Monolithic Analog Phase Shifters Based on Barium Strontium Titanate Coated Sapphire Substrates for WLAN Applications

A Thesis
Presented to
The Academic Faculty

by

Dongsu Kim

In Partial Fulfillment
of the Requirements for the Degree
Doctor of Philosophy in the
School of Electrical and Computer Engineering

Georgia Institute of Technology
March 2004

Monolithic Analog Phase Shifters Based on Barium Strontium Titanate Coated Sapphire Substrates for WLAN Applications

Approved by:

Dr. J. Stevenson Kenney, Advisor

Dr. Mark G. Allen

Dr. John Papapolymerou

Dr. Madhavan Swaminathan

Dr. Andrew T. Hunt

March 26 2004

Table of Contents

Acknowledgements ..... **vi**

List of Tables ..... **viii**

List of Figures ..... **ix**

List of Abbreviations ..... **xv**

Summary ..... **xvii**

CHAPTER I : Introduction **1**

CHAPTER II : Background Information: Barium Strontium Titanate (BST) Technology **6**

2.1 Fundamental Behavior and Motivation to Use BST Thin Films 6

2.2 Historical Summary of BST Devices 12

2.3 Conventional BST Phase-Shifter Topologies 14

2.4 Comparison of Other Phase-Shifter Technologies 25

CHAPTER III : BST Device Fabrication **28**

3.1 BST Thin Film Deposition and Substrate Preparation 28

3.2 Metallization Processes 31

3.2.1 Top Electrodes 31

3.2.2 Air Bridges 35

3.3 Conclusions 37

CHAPTER IV : BST Device Implementation and Characterization **38**

4.1 *S*-Parameter Measurement and Calibration 38

4.2 Coplanar Waveguides (CPWs) on BST Coated Substrates.....40

4.3 Interdigital Capacitors (IDCs) on BST Coated Substrates 44

4.3.1 Influence of Geometry 46

4.3.2 Effect of BST Composition and Thickness..... 49

4.3.3 Characterization over Temperature 53

4.3.4 IDC Modeling 57

4.4 Meandered-Line and Spiral Inductors 60

4.5 Intermodulation Distortion Measurement and Dynamic Range Extension 64

4.6 Conclusions.....70

CHAPTER V : *S*-Band Reflection-Type Phase Shifters 71

5.1 3-dB Couplers on BST Coated Substrates 72

5.1.1 CPW Branch-Line Coupler..... 73

5.1.2 CPW Lange Couplers 75

5.2 Reflective Terminations 79

5.3 Reflection-Type Phase Shifters.....85

5.3.1 Small-Signal Characteristics..... 85

5.3.2 Nonlinear Characteristics..... 95

5.4 Conclusions.....97

CHAPTER VI : 2.4 GHz All-Pass Network Phase Shifters.....98

6.1 Simple All-Pass Network Phase Shifters 98

6.1.1 Theoretical Aspect 98

6.1.2 Experimental Validation: Single Section and Double Section..... 102

6.1.3 Temperature Characteristics.....112

6.2 Phase Shifters Using Two Quarter-Wave-Length Transmission Lines.....114

6.2.1 Theoretical Aspect 115

6.2.2 Experimental Validation..... 120

6.2.3 Temperature Characteristics..... 124

6.3 Conclusions.....125

CHAPTER VII : BST Beamforming Networks (BFNs) for WLAN Systems Using Client-Based Smart Antennas.....127

7.1 Description and Simulation of the System.....128

7.2 Hardware Description and Measurement of Two-Element BFNs 131

7.3 Experimental Validation of Throughput Improvement.....136

7.4 Conclusions.....139

CHAPTER VIII : Conclusions & Future Work 141

Appendix.....144

References.....149

Vita 156

Acknowledgements

First, I want to gratefully acknowledge the enthusiastic supervision of my research advisor, Professor J. Stevenson Kenney. His breadth of knowledge and depth of commitment to this area of research impressed me greatly and were critical to the completion of this project.

I am also deeply grateful to Professor Mark G. Allen for his valuable support and helpful comments during my research. I also thank the rest of my thesis committee, Professor John Papapolymerou, Professor Madhavan Swaminathan, and Dr. Andrew T. Hunt for reviewing my thesis and giving insightful comments.

Support for this research was provided by in part by U.S. Air Force SBIR contract number F33615-01-M-1950 under a subcontract from MicroCoating Technologies, Inc. This work was also supported by the Yamacraw Design Center, an economic development project funded by the State of Georgia. My special thanks go to Dr. Andrew T. Hunt and Mr. Patrick J. Marry at MicroCoating Technologies, Inc. for their vital role in providing me with BST samples.

I owe special thanks to Yoonsu Choi, Sang-Soo Je, and Yongkyu Yoon for their numerous technical discussions and assistance. I also thank Minsik Ahn, Edouard G. Desautel, and Gregory Quillard for their help with antenna simulation and measurement.

I am indebted to my many colleagues in the Communication Systems Technology (CST) Laboratory for providing a stimulating and fun environment in which to learn and grow. I am specifically grateful to Hyunchul Ku, Youngcheol Park, Wangmyoung Woo, Mike McKinley, Kungpop U-yen, Roland Sperlich, Jau Chen, Min Chen, and Marvin

Miller.

Finally, I must acknowledge my parents and my sisters for their constant love and support throughout my life. During my graduate studies, my beloved wife, Minchoung Kim, has been the source of endless encouragement. Without her support, love and presence, this study could not have been completed.

List of Tables

Table 2.1 Summary of BST phase-shifter performance. 25

Table 2.2 Comparison of a variety of aspects of three monolithic phase-shifter technologies. 27

Table 3.1 Comparison of CCVD with PLD and MOCVD for thin film depositions [56]. 29

Table 4.1 Capacitance variation of 15-finger IDCs at 2.4 GHz. 55

Table 4.2 Summary of measured inductors. 64

List of Figures

Figure 1.1 Overview of dissertation content. 3

Figure 2.1 Temperature dependence of a ferroelectric material [1]. 7

Figure 2.2 The structure of $Ba_xSr_{1-x}TiO_3$. (so-called Perovskite structure) 8

Figure 2.3 Overview of application areas for ferroelectric films [4]. 9

Figure 2.4 RF front-end applications for BST thin films. 11

Figure 2.5 Linear phased-array using phase shifters. 11

Figure 2.6 CPW-based BST phase shifter. 16

Figure 2.7 Microstrip-based BST phase shifter. 16

Figure 2.8 Schematic of a loaded-line phase shifter with periodically loaded capacitors. 18

Figure 2.9 Parallel plate capacitor. 19

Figure 2.10 Interdigital capacitor. 20

Figure 2.11 Schematic of a reflection-type phase shifter. 21

Figure 2.12 Reflective terminations. (a) Single-series resonated termination. (b) Double-series resonated termination in parallel connection with a transformation network. 23

Figure 2.13 Loss FOM of phase shifters for three monolithic technologies. 27

Figure 3.1 Schematic representation of CCVD process [56]. 29

Figure 3.2 BST thin film cross section. 30

Figure 3.3 Metallization process using NR3000P photoresist. 32

Figure 3.4 SU-8 photoresist pattern process. 33

Figure 3.5 Metallization process using SU-8 photoresist. 34

Figure 3.6 SEM image of the 2 μm IDC using SU-8 photoresist. 34

Figure 3.7 Simplified air bridge fabrication step. 36

Figure 3.8 Photomicrograph of air bridges. (a) Spiral inductor. (b) Lange coupler. .. 36

Figure 4.1 *S*-parameter on-chip test setup. 39

Figure 4.2 Photomicrograph of the fabricated CPWs. 41

Figure 4.3 Loss and loss variation of various CPWs. 42

Figure 4.4 Effective dielectric constant and characteristic impedance for two different CPWs..... 42

Figure 4.5 BST permittivity as a function of bias voltage for a 5/10 structure. 43

Figure 4.6 SEM image of the fabricated interdigital capacitor. 44

Figure 4.7 Equivalent circuits by lumped element expression. (a) Capacitor under test. (b) Open circuit. (c) Short circuit proposed by K. Ikuta, *et al.* [61].. 45

Figure 4.8 Capacitance as a function of frequency for the capacitor with 13 fingers.46

Figure 4.9 Capacitance and Q-factor as a function of bias voltage for capacitors with 9, 11, 13, 17 fingers. 47

Figure 4.10 Tunability as a function of bias voltage at 2.4 GHz..... 48

Figure 4.11 Measured results for the capacitors with two different thicknesses at 2.4 GHz as a function of bias voltage. (a) Capacitance and tunability. (b) Q-factor. 50

Figure 4.12 Capacitance and Q-factor for capacitors with different (Ba+Sr)/Ti ratios.51

Figure 4.13 BST permittivity for capacitors with different (Ba+Sr)/Ti ratios. 52

Figure 4.14 Measured capacitance and Q-factor with two different compositions of BST thin films. 53

Figure 4.15 Capacitance and Q-factor as a function of bias voltage. (Ba/Sr=1.0, (Ba+Sr)/Ti=1.0) 55

Figure 4.16 Capacitance and Q-factor as a function of bias voltage. (Ba/Sr=1.2, (Ba+Sr)/Ti=0.8) 56

Figure 4.17 Measured and extracted Q-factors from 3 MHz to 6 GHz at 0 V..... 59

Figure 4.18 Effective loss tangent as a function of bias voltage. 60

Figure 4.19 Photomicrograph of (a) meandered-line inductors; (b) & (c) spiral inductors..... 61

Figure 4.20 Comparison of measured and simulated performances for spiral inductors..... 62

Figure 4.21 Intermodulation in a nonlinear device. 65

Figure 4.22 Relation between fundamental and third-order products. 65

Figure 4.23 Reduced IMD capacitor 66

Figure 4.24 Two-tone cancellation setup. 68

Figure 4.25 Fundamental output powers and third-order IM (IM3) products as a function of input power. 68

Figure 4.26 Input IP3 as a function of input power. 69

Figure 5.1 Schematic of a reflection-type phase shifter 72

Figure 5.2 Schematic of a CPW branch-line coupler. 73

Figure 5.3 Photomicrograph of the fabricated CPW branch-line coupler. 74

Figure 5.4 Experimental result of the CPW branch-line phase shifter. 74

Figure 5.5 Schematic of a CPW Lange coupler. 75

Figure 5.6 Photomicrograph of the fabricated Lange coupler. 76

Figure 5.7 Simulated result of the Lange coupler. (line width = 40 μm, spacing = 60 μm, and length = 9400 μm) 77

Figure 5.8 Measured result of the Lange coupler. (line width = 40 μm, spacing = 60 μm, and length = 9400 μm) 77

Figure 5.9 Measured result of the Lange coupler. (line width = 40 μm, spacing = 50 μm, and length = 9700 μm) 78

Figure 5.10 Measured result of the folded-type Lange coupler. 79

Figure 5.11 Reflective terminations with a bias network. (a) Single-series resonated termination. (b) Double-series resonated termination in parallel connection with a transformation network. 80

Figure 5.12 Simulated and measured differential phase-shift ranges of two different single-series resonated terminations. 82

Figure 5.13 Measured return losses of two different single-series resonated terminations 82

Figure 5.14 Measured differential phase shift of double-series resonated termination in parallel connection. 84

Figure 5.15 Measured return loss of double-series resonated termination in parallel connection. 84

Figure 5.16 Photomicrograph of the reflection-type phase shifter using the CPW branch-line coupler. 86

Figure 5.17 Insertion loss of the phase shifter under five different bias conditions. ... 86

Figure 5.18 Return loss of the phase shifter under five different bias conditions. 87

Figure 5.19 Differential phase shift with respect to the phase at 0 V for three different frequencies. 87

Figure 5.20 Photomicrograph of the reflection-type phase shifters. (a) Straight design. (b) Folded-type design. 88

Figure 5.21 Insertion loss and return loss of the phase shifter using the straight-design Lange coupler for 0, 40, 80, 120, and 160 V in the range of 1 GHz - 4 GHz. 89

Figure 5.22 Differential phase shift of the phase shifter using the straight-design Lange coupler with respect to the phase at 0 V for a 20-V step. 90

Figure 5.23 Insertion loss and return loss of the phase shifter using the folded-type design Lange coupler for 0, 40, 80, 120, and 160 V in the range of 1 GHz - 4 GHz. 91

Figure 5.24 Differential phase shift of the phase shifter using the folded-type design Lange coupler with respect to the phase at 0 V for a 20-V step. 91

Figure 5.25 Loss FOM of two different types of phase shifters. 92

Figure 5.26 Photomicrograph of the modified reflection-type phase shifter. 93

Figure 5.27 Measured result of the modified reflection-type phase shifter. (a) Insertion loss and return loss. (b) Differential phase shift with respect to the phase at 0 V. 94

Figure 5.28 Two-tone test setup. 95

Figure 5.29 Nonlinear response of the reflection-type phase shifter with four different bias states. (a) Fundamental output powers and third-order IM products (IM3) as a function of input power. (b) Input IP3 as a function of input power. 96

Figure 6.1 Schematic of a simple all-pass network phase shifter. 99

Figure 6.2 Decomposition of the simple all-pass network phase shifter into even- and odd-mode excitations. (a) Even mode. (b) Odd mode. 99

Figure 6.3 Simulated insertion and return losses of the all-pass network phase shifter. 101

Figure 6.4 Photomicrograph of the single-section all-pass network phase shifter. .. 103

Figure 6.5 Measured capacitance and Q-factor for a capacitor at 2.4 GHz. 103

Figure 6.6 Insertion and return losses. (a) MoM simulation. (b) Measurement. 104

Figure 6.7 Differential phase shift with respect to the phase at 0 V. (a) MoM simulation. (b) Measurement. 105

Figure 6.8 Loss FOM of the single-section all-pass network phase shifter. 106

Figure 6.9 Measured result of the single-section all-pass network phase shifter with 2 μm-spaced IDCs. (a) Insertion loss and return loss. (b) Differential

phase shift with respect to the phase at 0 V. 107

Figure 6.10 Fundamental output powers and third-order IM (IM3) products as a function of input power for two different phase shifters. 109

Figure 6.11 Photomicrograph of the double-section all-pass network phase shifter.. 109

Figure 6.12 Measured result of the double-section all-pass network phase shifter. (a) Insertion loss and return loss. (b) Differential phase shift with respect to the phase at 0 V. 110

Figure 6.13 Loss FOM of the double-section all-pass network phase shifter. 111

Figure 6.14 Temperature dependence of the all-pass network phase shifter (Ba/Sr = 0.9 and (Ba+Sr)/Ti = 0.8). 113

Figure 6.15 Temperature dependence of the all-pass network phase shifter (Ba/Sr = 1.2 and (Ba+Sr)/Ti = 0.8). 113

Figure 6.16 Loss FOM of a phase shifter for four different temperature states (Ba/Sr = 1.2 and (Ba+Sr)/Ti = 0.8) 114

Figure 6.17 Schematic of the all-pass network phase shifter using quarter-wave-length transmission lines. 115

Figure 6.18 The equivalent circuit for a quarter-wave-length transmission line. 115

Figure 6.19 Decomposition of the phase shifter into even- and odd-mode excitations. (a) Even mode. (b) Odd mode.....116

Figure 6.20 Differential phase shift as a function of inductance for different values of capacitor C_1. (a) Tunability, $r = 2.5$. (b) Tunability, $r = 3$. 119

Figure 6.21 Photomicrograph of the all-pass network phase shifter using quarter-wave-length transmission lines. 120

Figure 6.22 Measured result of the phase shifter for bias voltages from 0 V to 180 V. (a) Insertion and return loss. (b) Differential phase shift with respect to the phase at 0 V. 122

Figure 6.23 Measured result of the phase shifter for bias voltages from 0 V to 160 V. (a) Insertion and return loss. (b) Differential phase shift with respect to the phase at 0 V. 123

Figure 6.24 Temperature dependence of an all-pass network phase shifter using quarter-wave-length transmission lines. 124

Figure 6.25 Loss FOM of the phase shifter at three different temperature states. 125

Figure 7.1 Scheme of the system used for the simulation. 129

Figure 7.2 Simplified block diagram of the WLAN system connected to a two-element BFN. 130

Figure 7.3. Photograph of the BFN, packaged phase shifter, and bond wire. 131

Figure 7.4 Measured beam pattern with phase difference of 0° (diamond), -90° (circle), 90° (square), and 60° (triangle). 132

Figure 7.5 Photomicrograph of the integrated two-element BFN. 133

Figure 7.6 Wilkinson power divider based on a BST coated sapphire substrate. (a) Photomicrograph. (b) Measured result. 134

Figure 7.7 BFN performance from measured data of the power divider and phase shifters. 135

Figure 7.8 Rejection of interference signal versus angle of beam. 136

Figure 7.9 Measured throughput and detected noise level in an indoor environment. (Carrier: LoS, Interference: LoS, and 54 dB SNR at the AP). 138

Figure 7.10 Measured throughput and detected noise level in an open outdoor environment. (Carrier: LoS, Interference: LoS, and 38 dB SNR at the AP). 138

Figure 7.11 Measured throughput and detected noise level in an open outdoor environment. (Carrier: NLoS, Interference: LoS, and 22 dB SNR at the AP). 139

List of Abbreviations

AP	Access point
Au	Gold
Ba	Barium
BFN	Beamforming network
BST	Barium strontium titanate
CCVD	Chemical combustion vapor deposition
CPW	Coplanar waveguide
Cr	Chrome
Cu	Copper
CW	Continuous wave
dB	Decibel
DI water	De-ionized water
DRAM	Dynamic random access memory
DSSS	Direct sequence spread spectrum
E-beam	Electron beam
EM	Electromagnetic radiation
FOM	Figure of merit
GaAs	Gallium arsenide
HF	Hydrofluoric
H_2SO_4	Sulphuric acid
HTS	High temperature superconductor
IDC	Interdigital capacitor
IMD	Intermodulation distortion
IP3	Third order intercept point
LoS	Line of sight
MEMS	Micro electro mechanical system
MESFET	Metal semiconductor field effect transistor
MMIC	Monolithic microwave integrated circuit
MOCVD	Metal organic combustion vapor deposition
MoM	Method of moment
NLoS	Nonline of sight
NVFRAM	Non-volatile ferroelectric random access memory
PLD	Pulsed laser deposition
PR	Photoresist
Q-factor	Quality factor
QPSK	Quadrature phase shift keying
RF	Radio frequency
SEM	Scanning electron microscope
Si	Silicon
SNR	Signal to noise ratio
S-parameter	Scattering parameter
Sr	Strontium

STO	Strontium titanate
Ti	Titanium
UHF	Ultra high frequency
UV	Ultraviolet
VSWR	Voltage standing wave ratio
VHF	Very high frequency
WLAN	Wireless local area network

Summary

The objective of this research is to implement monolithic analog phase shifters based on barium strontium titanate (BST) coated sapphire substrates for IEEE 802.11b wireless local area network (WLAN) applications. It has been known that several BST thin film properties such as high relative permittivity, electric field dependence, fast polarization response, relatively low loss, and high breakdown field, allow for miniaturization and high performance of analog phase shifters. Before attempting to implement BST phase shifters, coplanar waveguides (CPWs) and interdigital capacitors (IDCs) based on various BST compositions and thicknesses have been developed and characterized to capitalize on the electrical properties of BST thin films.

Based on the characteristics of BST thin films, two design topologies have been studied to implement phase shifters. The first topology is a reflection-type structure. The reflection-type phase shifter composed of a 3-dB coupler and two identical reflective terminations has provided a large phase shift with a relatively low insertion loss. The second topology is an all-pass network structure. The all-pass network phase shifter consists of only lumped elements so that one can shrink in size of devices. The total chip area of the all-pass network phase shifter is only 2.6 mm × 2.2 mm with a loss figure-of-merit (FOM) of more than 69°/dB at 2.4 GHz. This is the smallest size and the best performance obtained to date for BST phase shifters in the 2.4 GHz band and comparable or even better than the state of the GaAs MMIC phase shifters. The nonlinear response of the all-pass network phase shifter also was investigated with two-tone intermodulation distortion (IMD) measurement. Furthermore, the all-pass network phase shifter was

studied to ascertain a design to ensure minimum performance variation over a range of temperature and to determine which BST composition performed best in the face of temperature variations.

Compact beamforming networks (BFNs) for WLAN systems using client-based smart antennas have been demonstrated to validate the feasibility of BST technology for WLAN applications. The two-element BFNs have been shown to increase throughput and network capacity by rejecting interference.

CHAPTER I

INTRODUCTION

With recent increase in market demand for wireless communications, there has been the added pressure to minimize the size of RF circuits and implement tunable devices. The high permittivity and electric field dependence of ferroelectric materials that could allow for miniature and tunable RF devices have been well-known. In particular, barium strontium titanate (BST) thin films have been found to be one of the most suitable ferroelectric materials at high-frequency applications because of their high tunability, high permittivity, and relatively low loss. Therefore, these materials have resulted in a new class of tunable RF devices including varactors, tunable matching networks, frequency-agile filters, voltage-controlled oscillators, and phase shifters.

Among these devices, considerable effort has been devoted to develop phase shifters. These are an essential component in phased-array antennas for telecommunication and radar applications. In most phased-array antennas, electronically variable phase shifters and/or time-delay devices are required in order to electronically steer beams. Compact and low-cost phase shifters are required for commercial applications such as 802.11a, b, and g wireless local area networks (WLANs) in which beamforming networks (BFNs) that use client-based smart antennas, can improve capacity by applying spatial filtering to separate carrier signals from interference by the angle of arrival.

With the advent of monolithic microwave integrated circuit (MMIC) technology, there has been intensive research on MMIC phase shifters. These phase shifters provide small

size, low control voltage, and fast tuning speed, and thus have been extensively used in modern phased-array antennas. They can also be integrated with low-noise or medium-power amplifiers on the same chip, resulting in reduction of the assembly cost of phased-array antennas. However, they involve a relatively large loss and have low power-handling capability. Micro-electro-mechanical systems (MEMS) technology has recently emerged and shown significant promise for implementation of low loss phase shifters as an alternative to MMIC technology. MEMS phase shifters, which are mostly digital designs using MEMS switches, have a large phase-shift range with a low insertion loss beyond *X*-band. However, MEMS phase shifters have their own drawbacks in switching speed, limited resolution, and packaging issue.

Another promising technology relies on BST thin films to implement a phase shifter. This technology has the potential for tunable elements that capitalize on high tunability, fast tuning speed, relatively low loss, and high power-handling capability. Also, the high permittivity of BST thin films can shrink the size of circuits, which satisfies the increasing demand for miniaturization.

This dissertation focuses on implementing low-cost compact analog phase shifters based on BST coated sapphire substrates and applying them to the BFNs for WLAN systems using client-based smart antennas. Several phase-shifter topologies and their corresponding tradeoffs are studied, along with an investigation of BST properties at high-frequency range. Figure 1.1 illustrates the overview of the dissertation content that will be covered here.

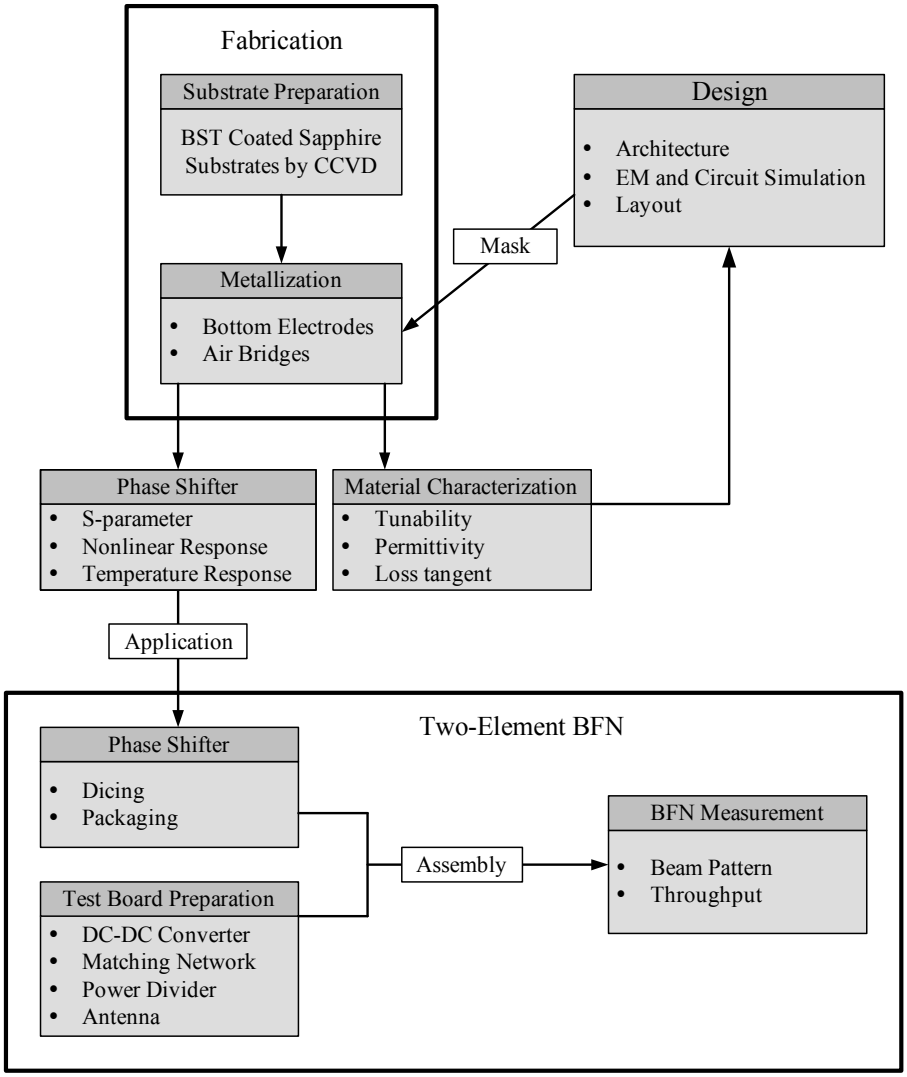

Figure 1.1 Overview of dissertation content.

Original contributions of this dissertation include

1. First development of monolithic BST reflection-type phase shifters using coplanar waveguide (CPW) Lange couplers and branch-line couplers.
2. First development of BST all-pass network phase shifters, resulting in best performance and smallest size obtained to date for BST phase shifters in the 2.4 GHz band.
3. First demonstration of BFNs for WLAN applications using BST phase shifters.

This dissertation is organized as follows:

In Chapter 1, a brief outline of the contents and organization of each chapter is described. Chapter 2 introduces fundamental behavior and motivation to use BST thin films for high-frequency applications. Chapter 2 also summarizes the historical perspective of numerous BST devices for high-frequency applications and conventional BST phase-shifter topologies. It also compares BST phase shifters with other technologies, including MEMS and MMIC phase shifters. Chapter 3 covers details of the fabrication process. A brief description of the combustion chemical vapor deposition (CCVD) process and comparison with conventional BST thin film deposition methods are discussed. Details of metallization process are covered as well. Dielectric properties of BST thin films using CPWs and interdigital capacitors (IDCs) are investigated in Chapter 4. Material parameters such as relative permittivity, tunability, and loss tangent are extracted from experimental data. The characterization and modeling of BST IDCs with respect to various BST compositions and thicknesses are described along with characterization over a range of temperature. Also, a gap capacitor to improve linearity, a so-called reduced intermodulation distortion (IMD) capacitor, is introduced. Chapter 5 and Chapter 6 converge more on phase-shifter implementation, starting with reflection-type phase shifters. CPW couplers, reflective terminations and phase-shifter responses are discussed in Chapter 5. Chapter 6 focuses on implementation of lumped-element structures to further reduce the size of phase shifters. Various design topologies and experimental results are discussed, resulting in the smallest size and the best performance obtained to date for BST phase shifters in the 2.4 GHz band. It also details the use of two-tone IMD measurement to derive the large signal characteristics of phase shifters.

Furthermore, the design of phase shifters to minimize variation over a range of temperature is discussed. Chapter 7 investigates the development of BFNs with BST phase shifters for WLAN systems using client-based smart antennas. To validate the feasibility of BST phase shifters for practical communication systems, 2.4 GHz miniature BFNs are implemented. The hardware used in this implementation are described along with a presentation of the measured data of the BFNs that revealed better throughput improvement than with commercial diversity systems. Finally, in Chapter 8, conclusions and future work are discussed.

CHAPTER II

BACKGROUND INFORMATION: BARIUM STRONTIUM TITANATE (BST) TECHNOLOGY

This chapter contains a discussion of the fundamental behavior of barium strontium titanate (BST) thin films in high-frequency applications, and the motivation for such use. Historical perspective on BST devices and a brief description of several BST phase-shifter topologies are also presented. In addition, other phase-shifter technologies are compared with this BST technology.

2.1 Fundamental Behavior and Motivation to Use BST Thin Films

Ferroelectric materials have been extensively studied as an important class of electronic materials. The main characteristic of these materials is that their permittivity is a function of an applied electric field and temperature. Ferroelectric materials show spontaneous polarization and hysteresis effects in the relation between a dielectric displacement and electric field, just as ferromagnetic materials do, and thus the name is ferroelectric even though they contain no iron (ferrum) [1].

The typical temperature dependence of the spontaneous polarization and permittivity in ferroelectric materials is shown in Figure 2.1. Below the transition temperature, which is called the Curie temperature, ferroelectric materials are in the ferroelectric state, which shows spontaneous polarization and the hysteresis effect. However, most RF devices and DRAM capacitors can take advantage of their high permittivity and/or field dependence

in the so-called paraelectric state, which is above the Curie temperature. In this state, the materials provide normal dielectric behavior and are no longer in the ferroelectric state. Most ferroelectric materials in the ferroelectric state incur large losses at high-frequencies, and exhibit the hysteresis effect, which is undesirable in high-frequency applications. It should be kept in mind that the sharp peak around the Curie temperature and permittivity are suppressed in a thin film compared with a bulk ferroelectric ceramic. The result in a thin film is that the phase transition between the ferroelectric and paraelectric states is considerably broadened because of fine grains, interfacial capacitance, and residual stress [2][3].

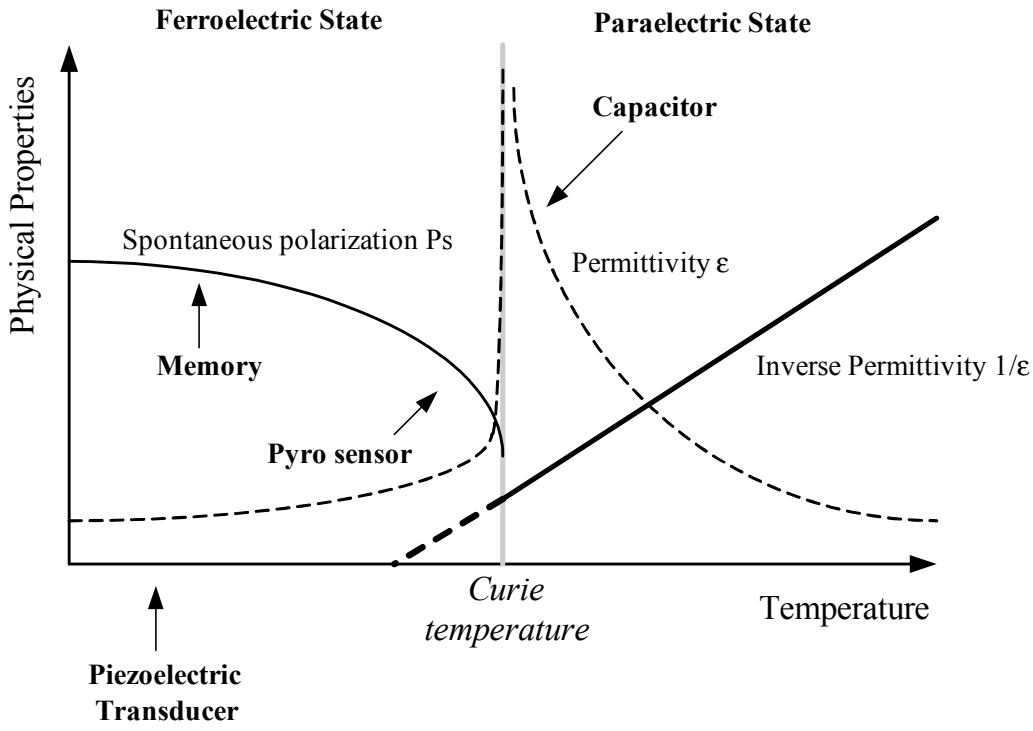

Figure 2.1 Temperature dependence of a ferroelectric material [1].

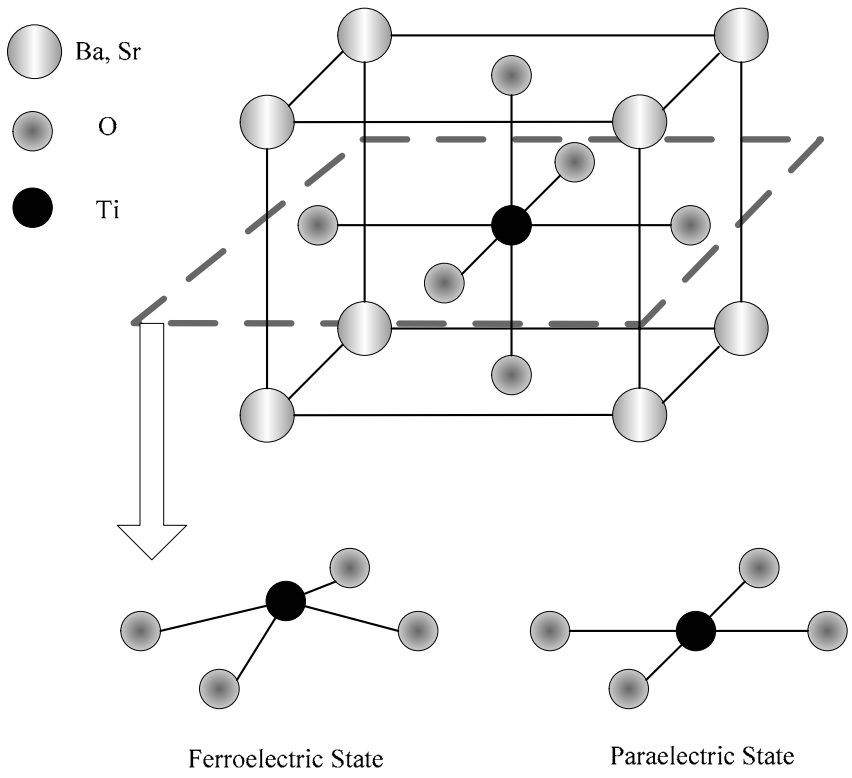

Figure 2.2 The structure of $Ba_xSr_{1-x}TiO_3$. (so-called Perovskite structure)

A perovskite crystal structure, which is a typical BST structure, is shown in Figure 2.2. In the paraelectric state, there is no spontaneous polarization, which means there is the symmetry among the Ti-ion, O-ion and Ba_xSr_{1-x}. The orientational polarization of the Ti-ion in the Perovskite structure results in high permittivity and tunability by applying bias voltage. In other words, a high dipole moment is induced because of the high electrical charge of the Ti-ion, and thus high permittivity and tunability of the dielectric constant can be obtained. In the ferroelectric state, spontaneous polarization occurs, and the structure becomes slightly elongated, as shown in Figure 2.2. In the paraelectric state, reciprocal relative permittivity $1/\varepsilon$ is known to be linear over a broad range of temperatures.[1],

$$\varepsilon = \frac{C}{(T - T_0)}, \tag{2.1}$$

where C is the Curie-Weiss constant and T_0 is the Curie-Weiss temperature. T_0 is slightly lower than the exact Curie temperature.

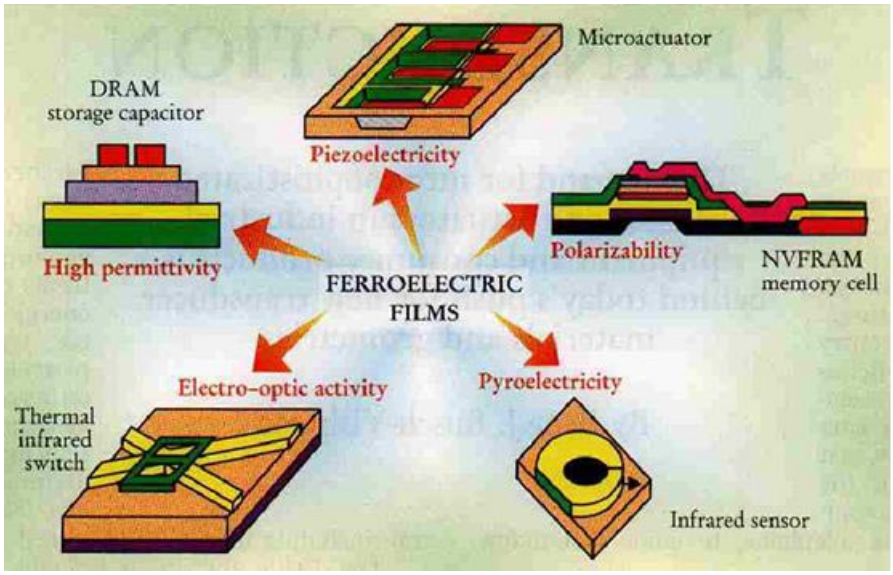

Figure 2.3 Overview of application areas for ferroelectric films [4].

An enormous range of ferroelectric film application areas are presented in Figure 2.3. One of the commercially viable options of ferroelectric films is non-volatile ferroelectric random access memory (NVFRAM) by using the ability of the ferroelectric materials to switch their polarization direction between two stable polarized states [4]. In addition, dynamic random access memory (DRAM), which is comprised of a transistor connected to an integrated capacitor, can use ferroelectric thin films. The transistor and a resistor in a conventional DRAM occupy a small portion of the space and most of the space is occupied by the capacitor; and thus the size of the cell can be reduced by taking advantage of the high permittivity of the materials. In addition to memory applications, a variety of other devices can use the special properties of ferroelectric thin films. For

instance, because of their piezoelectric and pyroelectric properties, they are suitable to use as mechanical transducers and infrared sensors, respectively, as shown in Figure 2.3.

Another important application of ferroelectric thin films, especially BST thin films is high-density varactors and frequency-agile devices for telecommunications. With the rapid expansion of wireless communication markets, low-cost, highly efficient miniature devices that operate at high-frequency ranges are in high demand.

Two major perspectives of high-frequency applications are shown in Figure 2.4 and Figure 2.5. The first one is a RF front-end application. The trend toward smaller and cheaper passive devices with higher-density varactors can be satisfied by incorporating BST thin films for use as duplexers, voltage-controlled oscillators, tunable matching networks, baluns, and so on. Although semiconductor varactors have been widely used recently, they are less than ideal at high-frequency ranges because of large losses and poor power-handling capability. Therefore, BST thin films are an alternative route to varactors and passive devices using because of their unique properties such as high permittivity, tunability, and relatively low loss.

A second major application for BST thin film technology lies in its use as a phase shifter for phased-array antennas. A phase shifter would increase interest in phase-array antennas for military and commercial systems like smart antenna systems for the wireless industry. BST phase shifters have the potential to replace MMIC phase shifters by reducing the cost of high-performance phased-array antennas. The comparison of BST phase shifters with MMIC and MEMS phase shifters will be discussed in the last section.

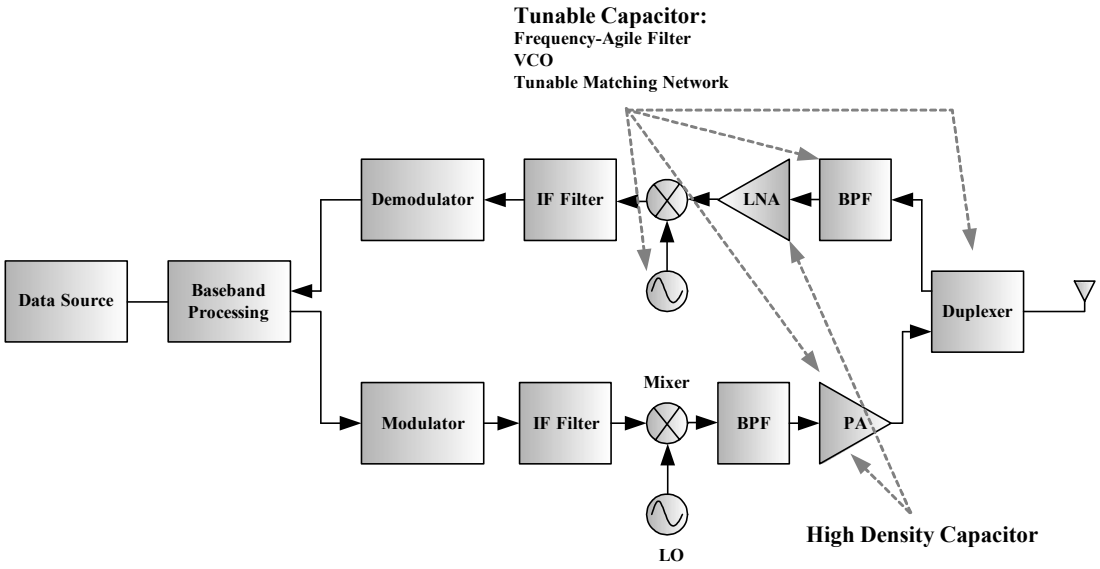

Figure 2.4 RF front-end applications for BST thin films.

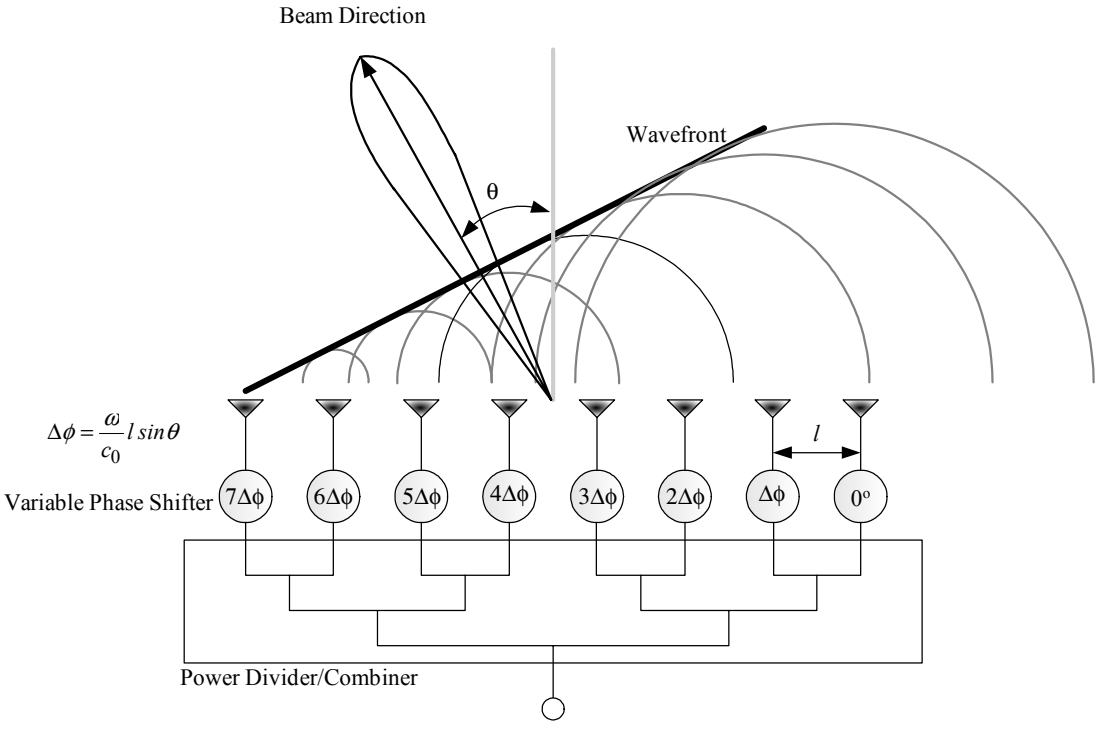

Figure 2.5 Linear phased-array using phase shifters.

2.2 HISTORICAL SUMMARY OF BST DEVICES

A survey of the literature reveals that numerous ferroelectric devices such as phase shifters, frequency multipliers, switches, harmonic generators, limiters, etc. have been developed since the late 1950s. An overview of these developments can be found in Fiedziuszko *et al.*, [5] but more details and some of latest work on BST devices are summarized in this section. In 1958, Morgenthaler showed ferroelectric ceramic to be suitable for velocity modulation by applying bias voltage [6]. Coleman and Becker discussed a ferroelectric frequency multiplier using barium titanate in 1959 [7]. An *X*-band ferroelectric phase shifter proposed by DiDomenico and Pantell and a ferroelectric phase shifter for VHF and UHF proposed by Cohn and Eikenberg were reported in 1962 [8][9]. The performance of the *X*-band phase shifter showed a phase-shift range of 40° - 50° with an average insertion loss of 5 dB, and the phase shifter for VHF provided a phase-shift range of 348° and an insertion loss from 3.7 to 2.2 dB at 207 MHz with 4000 V. Cohn and Eikenberg developed a high-power ferroelectric limiter in 1965, achieving a handling peak input power level of 25 kW and a small signal insertion loss of 0.5 dB [10]. In 1965, Amoss *et al.* proposed a ferroelectric microwave switch employing lead strontium titanate ($Pb_{0.315}Sr_{0.685}TiO_3$) as a ferroelectric material [11]. This switch had an isolation of 40 dB, an insertion loss of less than 1 dB, and a bandwidth of 10 %, with a switching voltage of 1000 V. A one-GHz ferroelectric limiter was proposed by Horton and Donaldson in 1967 [12]. In the same year, a microstrip phase shifter using a ferroelectric material was developed by Das [13].

In 1993, a microstrip resonator employing $YBa_2Cu_3O_{7-x}$ superconductors and $SrTiO_3$ ferroelectric films was developed by Beall *et al.*[14]. In 1995, Jackson *et al.* proposed a

CPW phase shifter using a high-temperature superconductor (HTS) and $Ba_xSr_{1-x}TiO_3$, resulting in 140° at 10 GHz with 30 V [15]. Instead of a CPW structure, De Flaviis *et al.* employed a microstrip structure so that the phase shifter could obtain 40°/dB at 2.4 GHz with 250 V [16]. Also, they described characteristics of various ferroelectric materials. In 1998, a ferroelectric microstrip band-pass filter was reported by Subramanyam *et al.* [17], and a frequency-shift range of 0.85 GHz was achieved at 19 GHz with 400 V. Kozyrev *et al.* [18] developed and discussed in 1998 a reflection-type phase shifter using BST varactors, a tunable filter, and IMD performance and proposed a distributed phase shifter using a CPW structure that in 2000 achieved 45°/dB at 30 GHz [19]. In the same year, periodically loaded-line phase shifters were reported using BST parallel plate capacitors as proposed by Erker *et al.* [20], and using BST interdigital capacitors as proposed by Liu *et al.* [21]. The phase shifters using parallel plate and interdigital capacitors achieved 27°/dB at 30 GHz with 20 V, and 32°/dB at 20 GHz with 100 V, respectively. Acikel *et al.* improved the performance of the above loaded-line phase shifter, achieving 45°/dB at both 20 and 30 GHz in 2001 [22]. A reflection-type one-bit phase shifter using BST was developed by Sherman *et al.*, resulting in 60°/dB at 5.4 GHz with 350 V [23]. In 2002, Tombak *et al.* have reported the characteristics of BST capacitors such as tunability, quality factor, and large signal characterization [24].

Thus, ferroelectric materials have shown great promise for various RF/microwave components, especially for tunable devices using field dependence permittivity. In the next sections, we will focus on various topologies to implement ferroelectric phase shifters and on comparison of ferroelectric technology with other technologies, such as semiconductors and MEMS.

2.3 CONVENTIONAL BST PHASE-SHIFTER TOPOLOGIES

A phase shifter, which is a two-port device whose function is to alter the phase of an RF signal, is an essential component in phased-array antennas for telecommunications, radar applications, and future generations of reconfigurable mobile communications. In most phased-array antennas, electronically variable phase shifters and/or time-delay devices are required to steer the beam electronically. The principle of electron scanning in a phased-array antenna is illustrated in Figure 2.5. The radiated beam can be steered by introducing a phase shift between successive elements. The required phase shift $\Delta\phi$ that must be introduced between the elements in order to create scan angle θ in the broad direction can be expressed as

$$\Delta\phi = \frac{\omega}{c_0} l \sin\theta , \tag{2.2}$$

where l is the inter-element spacing and c_0 is the free-space velocity. Another functional feature in phased-array antennas is null steering. Null steering can be used to reduce the interference signals by steering a deep null point. More details will be discussed in Chapter 7.

Among electronic phase shifters, monolithic phase shifters are more attractive than hybrid phase shifters because of their small size, reliability, and reproducibility. Monolithic phase shifters can be classified as either digital or analog. Their classification depends on whether the control element is used as an electronic switch or a continuously variable element. GaAs MESFETs, planar *p-i-n* diodes, and MEMS switches can be treated as electronic switches. A digital phase shifter provides several benefits over an analog phase shifter such as lower loss, easier interface with a digital computer to a

control signal, and so on. However, an analog phase shifter can be controlled with any desired resolution so that highly accurate beam control is possible, but the resolution of a digital phase shifter depends on the number of bits. Moreover, an analog phase shifter requires only a single control line; in a switched line phase shifter the number of control lines must equal the number of bits. The schottky-barrier gate capacitance of GaAs MESFETs has been most commonly used for monolithic analog operation.

BST thin films have several interesting properties at high frequencies: high permittivity, field dependent permittivity, fast tuning response, and high power-handling capability. The high permittivity allows for miniaturization, and the permittivity can be varied depending on an applied bias voltage so that the phase velocity of a transmission line and its capacitance can be altered. Furthermore, the fast polarization response and high breakdown field of BST thin films allow the fast tuning response and high power-handling properties of the phase shifter. Therefore, BST phase shifters can be an alternative technology to semiconductor and/or MEMS phase shifters for phased-array antennas that require rapid and continuous phase shifters.

Several groups have investigated phase shifters using BST thin films that are based on various substrates such as MgO, Al_2O_3, and Si. Two commonly used topologies of BST phase shifters are a distributed and a reflection-type structure. Figure 2.6 and Figure 2.7 show the schematics of microstrip and CPW-based phase shifters, which are typical structures of distributed phase shifters on BST thin films. In this case, BST forms the entire substrate on which conductors are deposited. By applying a bias voltage between a signal line and ground planes, the variation of the propagation constant of the transmission lines can occur because of the variation of the dielectric constant.

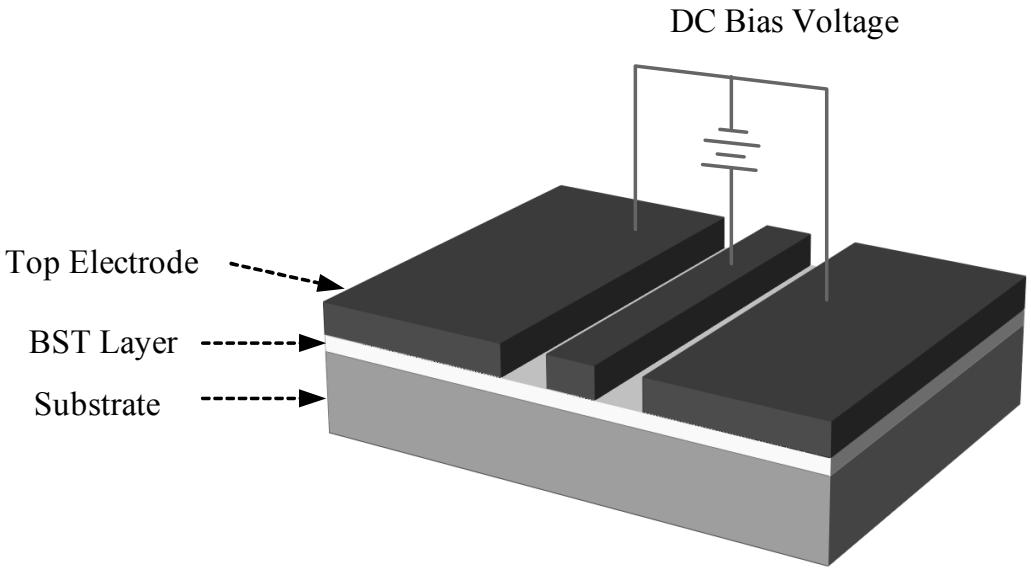

Figure 2.6 CPW-based BST phase shifter.

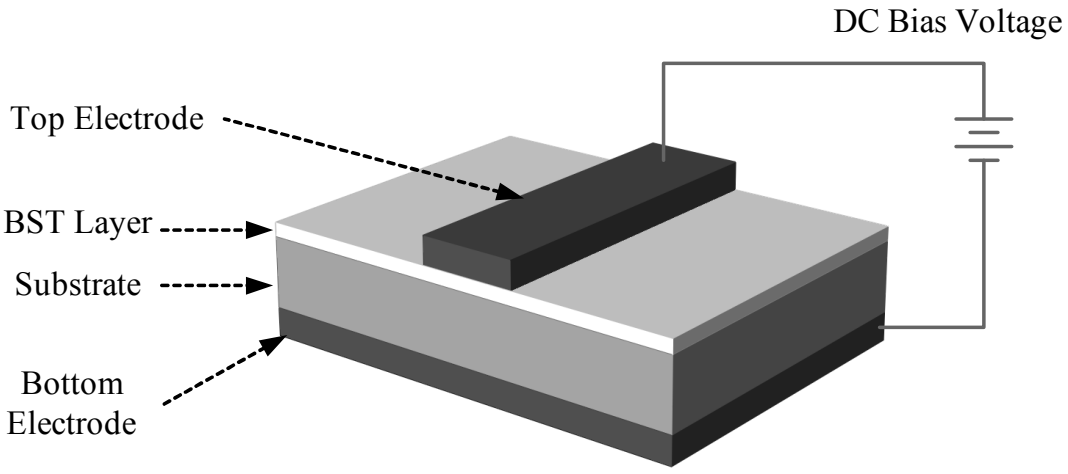

Figure 2.7 Microstrip-based BST phase shifter.

The phase velocity and phase constant can be expressed as

$$v_p(V) = \frac{c_0}{\sqrt{\varepsilon_{eff}(V)}}, \tag{2.3}$$

$$\beta(V) = \frac{\omega}{v_p(V)} = \frac{2\pi\sqrt{\varepsilon_{eff}(V)}}{\lambda_0}, \tag{2.4}$$

where c_0 is the velocity of light in free-space, λ_0 is the wavelength of free-space, $\varepsilon_{eff}(V)$ is the effective dielectric constant depending on an applied bias voltage, and l is the length of the transmission line. Therefore, the differential phase shift is found from the change in the phase constant given by

$$\Delta\phi = l\,\Delta\beta = l\left(\beta_{max}(V) - \beta_{min}(V)\right) = 2\pi l \frac{\left(\sqrt{\varepsilon_{eff}^{max}} - \sqrt{\varepsilon_{eff}^{min}}\right)}{\lambda_0}. \tag{2.5}$$

In 1995, Jackson *et al.* proposed the CPW phase shifter using a high-temperature superconductor (HTS) and BST, which resulted in 140° at 10 GHz with 30 V [15]. De Flaviis *et al.* designed a planar microstrip phase shifter using BST, achieving more than 160° with an insertion loss below 4 dB at 2.43 GHz with a bias voltage of 250 V in 1997 [16]. Also, Kozyrev *et al.* reported on a 30 GHz BST phase shifter based on a CPW structure [19]. In 2000, continuous 360° phase shift was obtained with a maximum insertion loss of 8 dB using 350 V. However, this approach has some limitations in spite of the simple structure. The tunability of the ferroelectric material is not efficient, and high control voltages are required.

Another approach to realize a distributed-type phase shifter is to rely on BST parallel plate capacitors or interdigital capacitors (IDCs) periodically loading a transmission line, as shown in Figure 2.8. This structure behaves like a synthetic transmission line and can

be approximated in terms of the inductance and capacitance per unit length below the Bragg frequency.

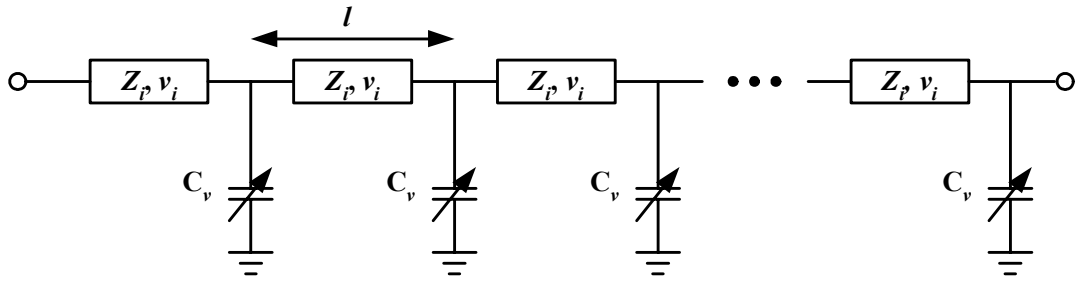

Figure 2.8 Schematic of a loaded-line phase shifter with periodically loaded capacitors.

These phase shifters consist of a high impedance transmission line that is periodically loaded with capacitors that enable the phase velocity to be altered. After capacitive loading, the characteristic impedance of the loaded-line reduces to 50 Ω. The Bragg frequency is given by [25] as

$$f_{bragg} = \frac{1}{\pi\sqrt{L_t\left(C_t + C_v(V)\right)}}, \tag{2.6}$$

where L_t and C_t are the unloaded-line inductance and capacitance per unit length, respectively. The characteristic impedance and phase velocity for the loaded line can be expressed as

$$Z_0(V) = \sqrt{\frac{L_l}{\left(C_l + \frac{C_v(V)}{l}\right)}}, \tag{2.7}$$

$$v_p(V) = \sqrt{\frac{1}{\left(L_l\left(C_l + \frac{C_v(V)}{l}\right)\right)}}, \tag{2.8}$$

where L_l and C_l are the loaded-line inductance and capacitance per unit length, and l is

the length of each section of transmission line. The phase constant and differential phase shift in (2.4) and (2.5) can be rewritten as

$$\beta(V) = \frac{\omega}{v_p(V)} = \omega\sqrt{L_l\left(C_l + \frac{C_v(V)}{l}\right)}, \tag{2.9}$$

$$\Delta\phi = l\,\Delta\beta n = l\left(\beta_{max}(V) - \beta_{min}(V)\right)n = l\omega n\sqrt{L_l}\left(\sqrt{C_l + \frac{C_v^{max}}{l}} - \sqrt{C_l + \frac{C_v^{min}}{l}}\right), \tag{2.10}$$

where n is the number of sections.

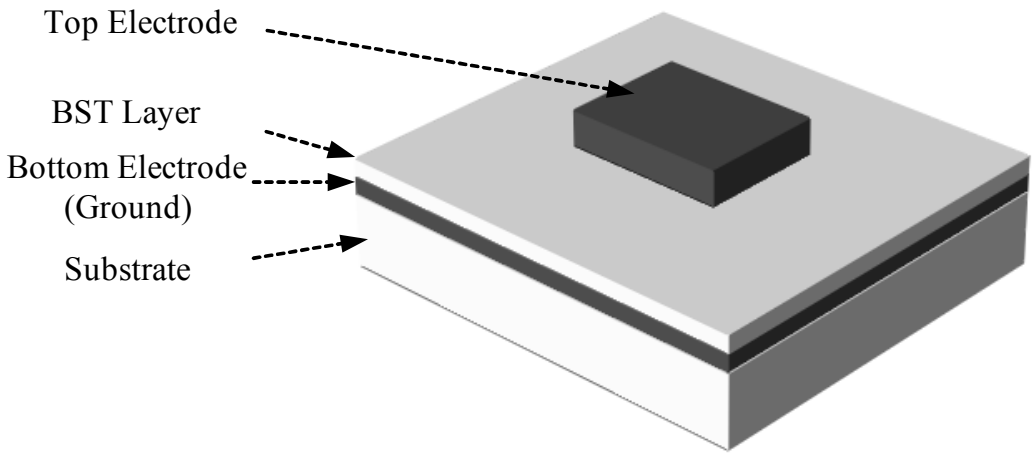

Figure 2.9 Parallel plate capacitor.

Erker *et al.* proposed a loaded-line phase shifter employing BST parallel plate capacitors as tuning elements [20]. The schematic representation of the parallel plate capacitor is shown in Figure 2.9. A CPW transmission line of characteristic impedance 100 Ω was fabricated on a high-resistivity silicon substrate (40 KΩ-cm). The performance showed a phase-shift range of 157° at 30 GHz with a 5.8-dB insertion loss using 20 V. To obtain 160° phase shift at 20 GHz, nine identical cells were connected in series; resulting in a total length of 3.06 mm. Acikel *et al*. improved the performance of a

distributed phase shifter using advanced BST parallel plate capacitors [26]. This phase shifter provided a phase-shift range of 240° with an insertion loss of 3 dB at 10 GHz at room temperature using 17.5 V.

BST IDCs on a sapphire substrate have also been used with the same topology proposed by Liu *et al.* [21]. The schematic representation of an IDC is shown in Figure 2.10. The 1 μm spaced capacitor can tune the capacitance from 7 pF at 0 V to 3.8 pF at 90 V, while the 2 μm-spaced capacitor has much lower tunability because the DC bias is not large enough to tune the capacitor effectively. The phase shifter using the 1 μm-spaced capacitors demonstrated a phase-shift range of 110° at 20 GHz with an insertion loss of below 3.4 dB using 100 V. The main advantages of BST IDCs over BST parallel plate capacitors are that the quality factor of the IDCs is higher than that of the parallel plate structures, and IDCs are easier to fabricate. The periodically loaded-line phase shifters using either parallel plate or interdigital capacitors are more efficient in terms of the tunability of BST with a lower bias voltage compared with the simple transmission-line phase shifters.

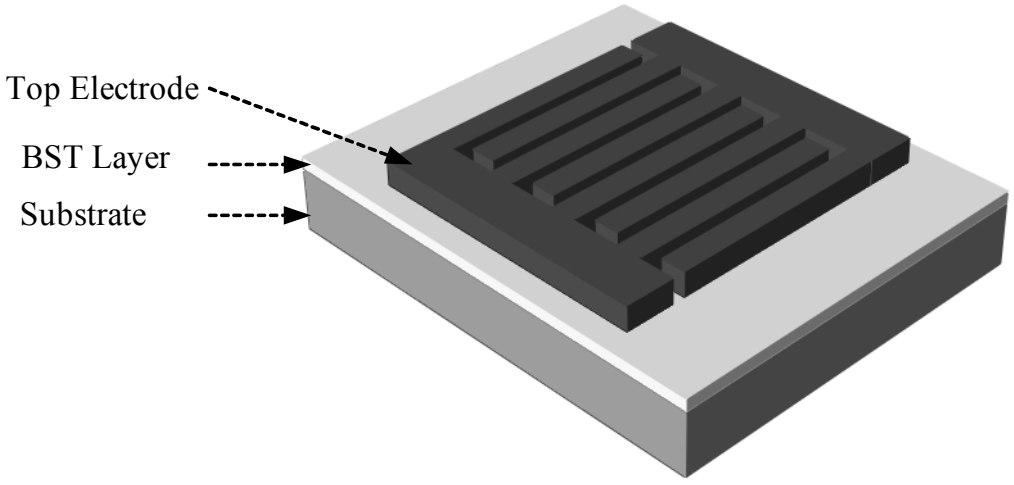

Figure 2.10 Interdigital capacitor.

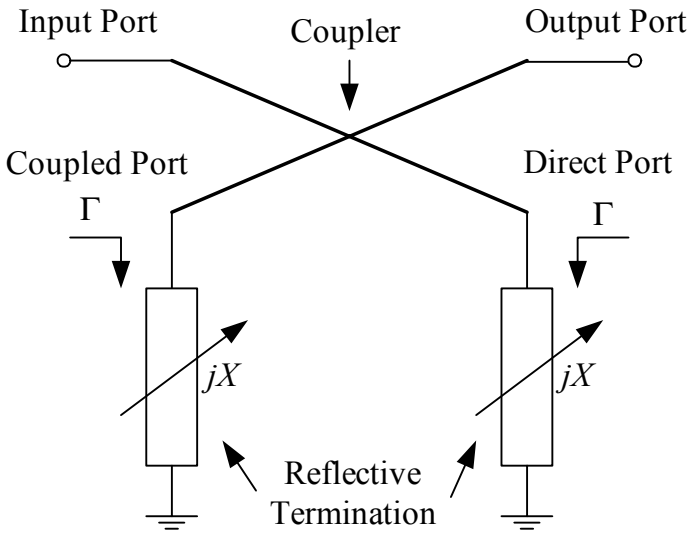

Figure 2.11 Schematic of a reflection-type phase shifter.

Another configuration to create BST phase shifters involves a reflection-type structure. A reflection-type phase shifter was first introduced by Hardin *et al.* using varactor diodes, which have been the most common elements for this structure [27]. A reflection-type phase shifter makes use of the reflective terminations in conjunction with a 3-dB coupler. Figure 2.11 shows the schematic of a reflection-type phase shifter. With reference to Figure 2.11, the coupler divides the input signal equally between two output ports with a phase difference of 90°. Reflected signals from reflective terminations sum at the isolated port of the coupler. If lossless LC terminations are connected to an ideal 3-dB coupler, all the power at the input port will emerge from the isolated port. The reflection-type phase shifter has a good return loss over a large range of phase shift.

The main control part of the reflection-type phase shifter is the reflective termination, which can be controlled by variable capacitances. If we neglect parasitics, the reflection coefficient Γ of the reflective termination is given by

$$\Gamma = \left|\Gamma\right| e^{j\phi} = \frac{jX - Z_0}{jX + Z_0}, \tag{2.11}$$

where Z_0 is the characteristic impedance of the input and output of the coupler. Therefore, the phase of the reflective termination can be expressed as

$$\angle\phi = \tan^{-1}\left(\frac{2Z_0 X}{X^2 - {Z_0}^2}\right) = \pi - 2\tan^{-1}\left(\frac{X}{Z_0}\right). \tag{2.12}$$

The reflection-type phase shifters using single series-tuned reflective terminations were developed by several groups using various varactor technologies as shown in Figure 2.12. Hardin *et al.* proposed a series-tuned reflective termination adopting varactor diodes [27], and Ellinger *et al.* have developed the smallest reflection-type phase shifter using a GaAs MESFET process for a satellite radar system [28]. By using a lumped element branch-line coupler and single-series reflective terminations, a phase-shift range of 210° with an insertion loss of 5.8 dB was achieved. Furthermore, an ultra-broad-band reflection-type phase shifter was suggested by Miyaguchi *et al.* [29] by switching two states of series and parallel reflective terminations. The reflection-type phase shifter using BST thin films was implemented by Kozyrev *et al.*[18]. This hybrid phase shifter made use of the rat-race hybrid coupler and BST capacitors as a variable reactance, resulting in 78°/dB in the frequency range of 1.8 GHz - 1.9 GHz. A monolithic reflection-type phase shifter based on BST thin films was first implemented by the author in 2.4 GHz [30][31]. This phase shifter consists of the CPW Lange coupler and single-series resonated terminations, which are composed of a series combination of two IDCs and inductors in order to increase the phase control range by resonating the capacitive reactance with the inductive reactance. An *X*-band reflection-type phase shifter has been developed by Serraiocco *et al.* using only lumped element components, and thus the size is less than 0.5

mm^2 [32]. The performance of the phase shifter showed a phase-shift range of 148° with an insertion loss of 11 dB.

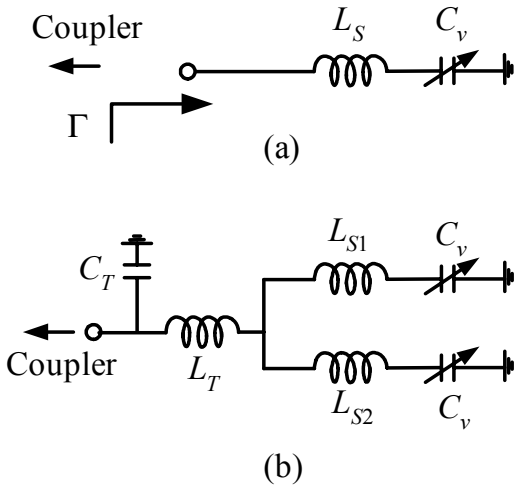

Figure 2.12 Reflective terminations. (a) Single-series resonated termination. (b) Double-series resonated termination in parallel connection with a transformation network.

However, in (2-12), a single-series resonated termination has the drawback of a limited phase-control range because of the limited tunability of the tuning element. Generally, a phase-shift range of 360° is required for a full azimuthally scanning range in adaptive phased-array antennas. One method to achieve a 360° phase shifter is to increase the phase variation of the reflective termination by using two different series resonated terminations in parallel, a concept first introduced by Henoch and Tamm in 1970 [33], as shown in Figure 2.12. One resonated termination is series resonant at the lowest bias voltage (maximum capacitance), whereas the other is at the highest voltage (minimum capacitance). Also, an LC transformation network can be added to decrease loss variation and the maximum loss. The author has developed double-series resonated terminations using BST thin films, achieving more than a phase-shift range of 360° with an average

loss of 4.7 dB at 2.5 GHz [34].

Table 2.1 presents a summary of the performance of BST phase shifters based on several designs at various frequencies. From Table 2.1 it can be seen that except for the phase shifter using parallel plate capacitors (PPCs), a bias voltage to operate phase shifters is relatively high because of low field concentration by IDCs and CPW/microstrip transmission lines. However, a reduction in dynamic range is also observed in low bias voltage phase shifters. Therefore, the device involves a tradeoff between bias voltage and linearity. Further discussion of nonlinear response and dynamic range extension of IDCs and phase shifters can be found in the later chapters. Several distributed phase shifters have been developed with microstrip, CPW, and CPW periodically loaded BST capacitors. However, the total lengths of phase shifters are relatively long (e.g., 3 mm at 30 GHz for 160° and 17.5 mm at 10 GHz for 240°). The reflection-type phase shifters, which have a large bandwidth, were also implemented, resulting in a low insertion loss at 1.85 and 2.4 GHz. To achieve smaller size and better performance, the phase shifter using an all-pass network structure was designed by the author. This phase shifter occupies only 5.7 mm^2 for 121° and 10.9 mm^2 for 255° with the loss figure-of-merit of the phase shifter (FOM) of 69°/dB. By using smaller spaced IDCs, a phase-shift range of more than 100° could be obtained with an applied bias voltage of only 40 V.

Table 2.1 Summary of BST phase-shifter performance.

Design	Control element	$\Delta\phi$ (°)	Max. S_{21} (dB)	Freq. (GHz)	Voltage (V)	Ref.
CPW loaded line	PPC	157	5.8	30	20	[20]
CPW loaded line	IDC	110	3.4	20	100	[21]
CPW loaded line	PPC	265	5.8	20	30	[22]
CPW loaded line	PPC	240	3	10	17.5	[26]
Microstrip	Microstrip	165	3	2.4	250	[16]
CPW	CPW	360	8	31	350	[19]
Reflection type	IDC	110	1.4	1.85	100	[18]
Reflection type (Digital)	IDC	195	3.2	5.4	350	[23]
Reflection type	PPC	148	11	9.4	10	[32]
***Reflection type**	IDC	137	2.4	2.4	160	[31]
***Reflection type**	IDC	370	8	2.4	160	[34]
***All-pass network**	IDC	255	3.7	2.4	140	[35]
***All-pass network**	IDC	100/140	2.37	2.4	40/80	[3]

* Implemented by the author at the Georgia Institute of Technology

2.4 Comparison of Other Phase-Shifter Technologies

The previous section contained a brief description and summary of BST phase shifters. It is also necessary to compare this technology with others such as GaAs-based MMIC and MEMS technologies with their various aspects. Table 2.2 contains comparison of three competing monolithic phase-shifter technologies. GaAs-based MMIC phase shifters have been used extensively in modern phased-array antennas. A fast tuning speed (an order of nsec) and ease of integration with other devices, such as power amplifiers, on the same chip are benefits of this technology in both analog and digital operations. However, they involve a relatively large loss and have poor power-handling capability.

Recently, MEMS technology has shown significant promise for implementation of phase shifters. The most distinguished feature of a MEMS phase shifter is very low loss in combination with good power-handling capability. However, most MEMS phase shifters have been developed based on using MEMS switches to replace solid-state

switches in established phase-shifter designs, and thus their resolution is somewhat limited. Packaging issues and the stiction problem also have been concerns with MEMS phase shifters.

BST phase shifters, however, can overcome those problems. Compared to GaAs-based MMIC phase shifters, they provide better power-handling capability and linearity at the expense of bias voltage. Also, their simple fabrication on inexpensive substrates can reduce the cost of the circuits. The ease of packaging and their fast tuning speed are advantages over MEMS phase shifters.

It should be noted that in general there are advantages and disadvantages with each technology, so that the choice of which to use depends heavily on the application. However, with reference to Table 2.2, phase shifters present one of the most appropriate applications for BST technology because they require fast and continuous tuning, small size and relatively low loss as well as low cost. This phase-shifter application cannot be addressed easily by MEMS phase shifters because of their slow tuning response nor by GaAs-based MMIC phase shifters because of their high loss and low power-handling capability.

Figure 2.13 shows a comparison of three monolithic phase-shifter technologies with respect to the loss FOM of the phase shifter, which is calculated as the ratio of the differential phase shift and the maximum insertion loss of the phase shifter. MEMS phase shifters, which are mostly digital designs using MEMS switches, have a large phase-shift range with a low insertion loss beyond *X*-band. A continuously distributed MEMS phase shifter was also implemented, which has the tunability of the MEMS varactor of below 1.5. BST phase shifters introduce a comparable or even better FOM from *L* to *X*-band

than GaAs-based MMIC phase shifter, as shown in Figure 2.13.

Table 2.2 Comparison of a variety of aspects of three monolithic phase-shifter technologies.

	GaAs-based MMIC	MEMS switched-line	BST
Type	Analog/Digital	Digital*	Analog
No. of control	Single/No. of bits	No. of bits	Single
Insertion loss	High	Low	Moderate
Control voltage	< 10 V	< 60 V	<20, >100 V**
Switching speed	High (1~5 nsec)	Low (1~20 msec)	High (few 10's nsec)
Power consumption	Few mW	Negligible (<few mW)	Negligible (<few mW)
Cost	High	???	Low
Nonlinearity* **	Poor	Good	Good
Power handling	Poor (few mW)	Good (few W)	Good (few W)

*Analog MEMS varactor: $C_{max}/C_{min} \approx 1.5$.
**By adopting parallel plate capacitors, control voltage can go down to 10 V.
***Nonlinearity depends on control voltage.

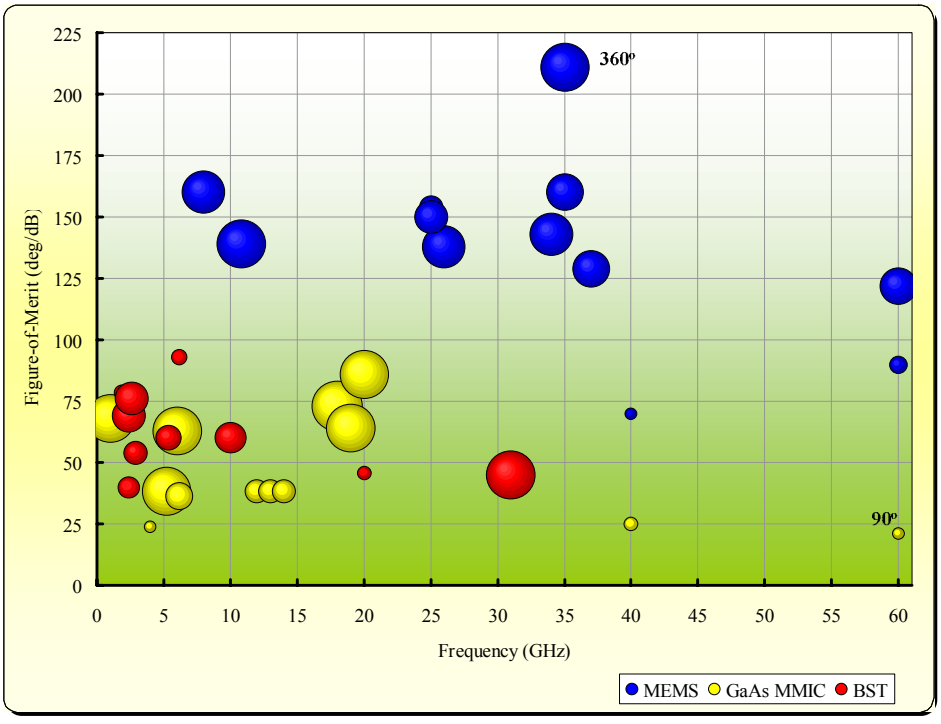

Figure 2.13 Loss FOM of phase shifters for three monolithic technologies.

CHAPTER III

BST DEVICE FABRICATION

In this chapter, details of the barium strontium titanate (BST) thin film deposition processes will be discussed along with the metallization process that was performed by the author at the Georgia Institute of Technology. Comparison of conventional thin film deposition methods with CCVD process will be included. Also, descriptions of photolithographic processes to produce very small patterns on the substrates will be introduced using different types of light-sensitive photoresists.

3.1 BST THIN FILM DEPOSITION AND SUBSTRATE PREPARATION

A significant amount of effort has been directed toward developing methods to grow high-quality BST thin films on single crystal substrates such as MgO, $LaAlO_3$, and Al_2O_3. A survey reveals that a variety of methods can be used to deposit BST thin films. In general, pulsed laser deposition (PLD), metalorganic chemical vapor deposition (MOCVD) and sputtering are widely used for depositing BST thin films. However, these vacuum-based methodologies are expensive, capital intensive, batch-process limited, and suffer from low throughput. Although inexpensive, sol-gel requires a multiple deposition process to obtain an acceptable thickness with concurrent difficulties in maintaining the purity of the thin films.

An alternative is the low-cost, open atmosphere combustion chemical vapor deposition (CCVD) process, which was recently patented by the Georgia Institute of Technology and

licensed exclusively to MicroCoating Technologies (MCT), Inc. [56]. The CCVD technology has the potential to overcome many of the shortcomings of traditional vapor deposition techniques such as MOCVD and PLD while yielding equal and/or better quality coatings at a lower cost, as shown in Table 3.1.

Table 3.1 Comparison of CCVD with PLD and MOCVD for thin film depositions [56].

Characteristic	CCVD	PLD	MOCVD
Thin film quality	+	+	+
Control of thin film	+	O	O
Ease of doping	+	-	-
Deposition rate	+	O	+
Potential for scaling	+	-	O
Capital cost	+	-	O
Starting chemical materials	++	-	O
+: Positive, O: Neutral, and -: Negative			

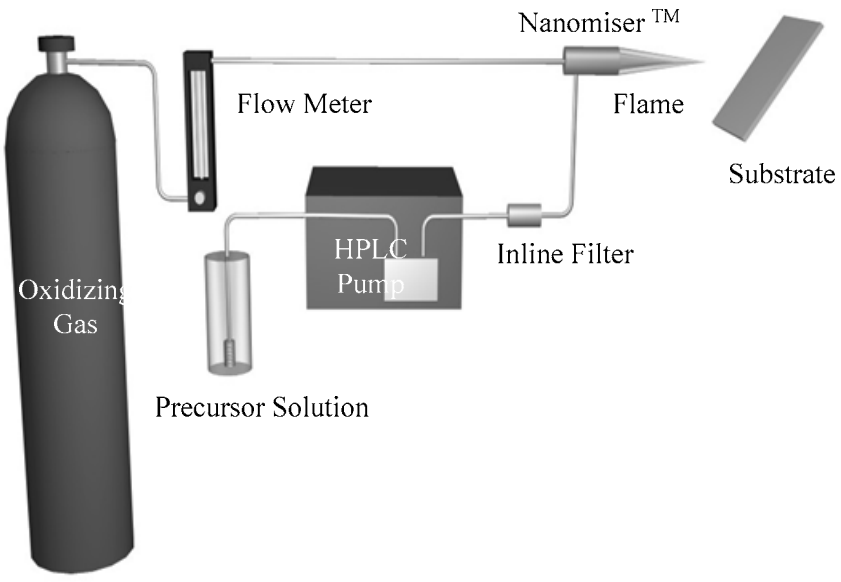

Figure 3.1 Schematic representation of CCVD process [56].

A schematic representation of the CCVD process is shown in Figure 3.1. In the process, precursors are dissolved in a solution, and this solution is atomized to form microscopic droplets by means of Nanomiser™, proprietary to MCT (patent pending). These droplets then are carried by an oxygen stream to the flame, and finally a substrate is coated by simply drawing it in the front of the flame. The heat from the flame provides the energy required to evaporate the droplets and for the precursors to react and to deposit on the substrates. Although flame temperatures can be in excess of 800°C, the substrate temperature can be actively controlled, so substrate temperature is an independent process parameter that can be varied to actively control the film's microstructure. The whole process generally takes no more than two hours from set-up to post-deposition cleaning. Among several possible microwave substrates, Al_2O_3 (sapphire) is chosen for the substrate in this research because of good insulating properties and low loss tangent with relatively low cost compared to MgO and $LaAlO_3$. Figure 3.2 shows the sapphire substrate with a 500 nm layer of BST thin film.

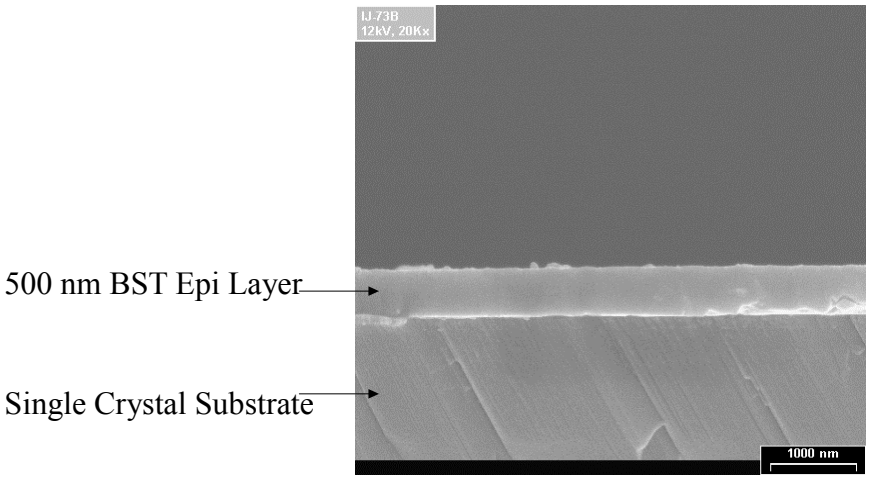

Figure 3.2 BST thin film cross section.

3.2 METALLIZATION PROCESSES

Based on the BST coated sapphire substrates prepared by the CCVD process described in the previous section, metallization was performed by the author at the Georgia Institute of Technology. Three mask steps are required to complete the fabrication of the phase shifter: The first establishes the top electrodes, and the others build air bridges. Details of these fabrication steps are as follows.

3.2.1 Top Electrodes

Two different types of photoresists are used to make the top electrodes. The first one is the NR3000P photoresist from Futurrex [57]. The simplified fabrication steps involved in the metallization on BST coated sapphire substrates using NR3000P photoresist are shown in Figure 3.3. The NR3000P photoresist is coated on a spinner and baked in an oven. The sample is then exposed through a chrome-glass mask to polymerize the pattern. After exposure, post-exposure baking is performed in an oven to selectively cross-link the exposed portions of the sample. After that, the photoresist is developed by Futurrex's developer. Finally, the sample is rinsed briefly with DI water and dried with a gentle stream of nitrogen. Metallization begins with deposition of 300 Å of chrome (Cr) or titanium (Ti) as an adhesion layer. On top of the chrome, 2 μm of copper (Cu), which is a good conductor (5.96×10^7 S/m) and has a high thermal conductivity, is deposited to form the main conductive layer. As an oxidation barrier for copper, 0.5 μm of gold (Au) is formed on the copper. A standard lift-off process using acetone is used then to create the bottom pattern on the substrate.

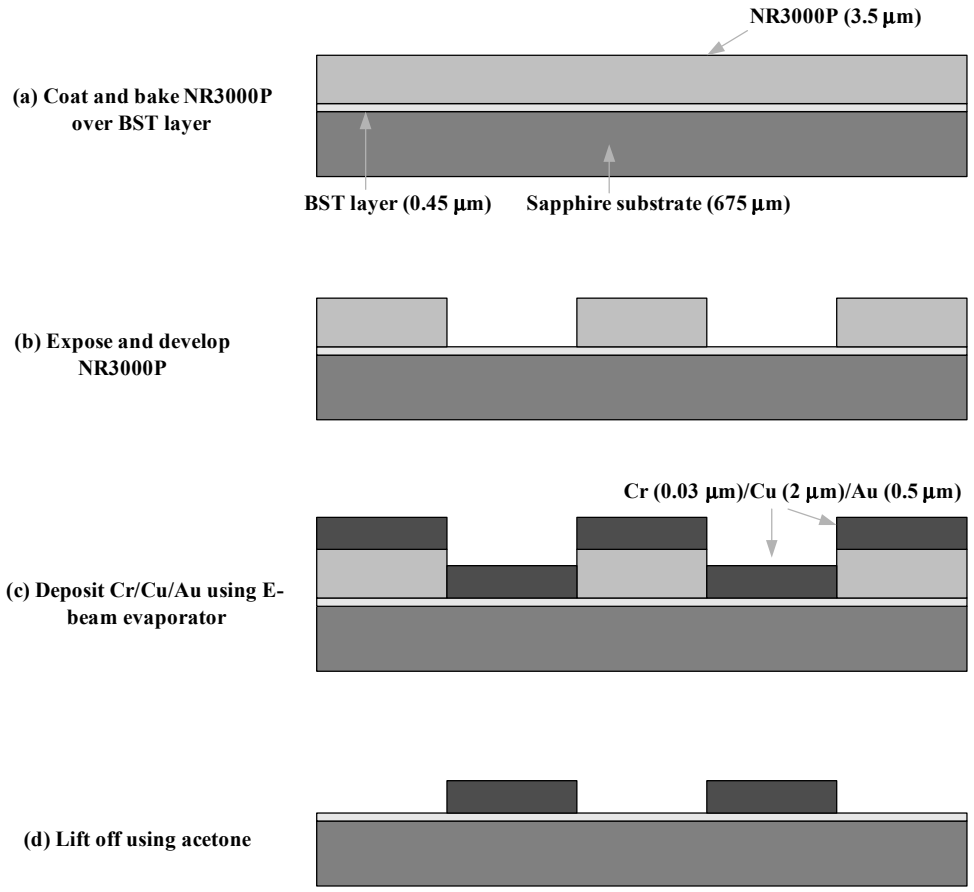

Figure 3.3 Metallization process using NR3000P photoresist.

The second way to make the top electrodes use the SU-8 photoresist from MicroChem [58] which yields a higher aspect ratio structure with near vertical side walls, MicroChem's SU-8 photoresist is used. Although the process using the NR3000P photoresist requires only a few steps for completion, it has limitations in its capability to create a structure with a high aspect ratio and small feature size. Standard spin, bake, and exposure recipes are created to build the structure of 1:2 aspect ratio (2 µm spacing and 4 µm photoresist thickness). The fabrication sequence requires a spinner, a hotplate, an exposure tool, and some wet chemicals, as shown in Figure 3.4 and Figure 3.5.

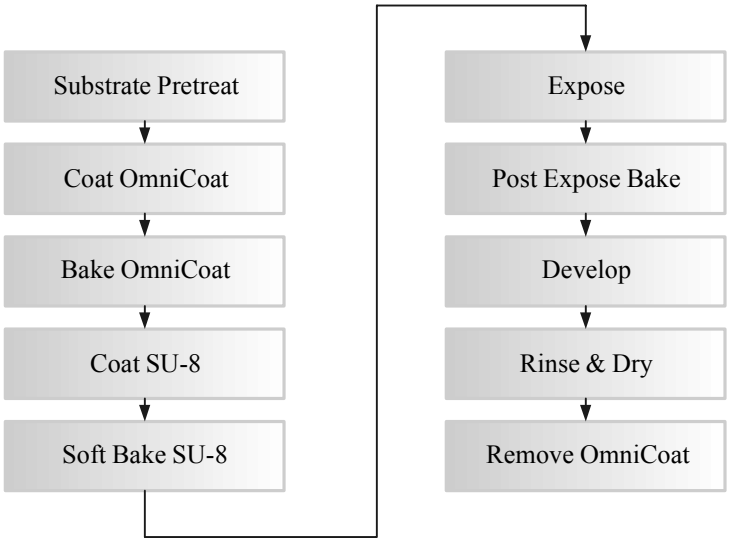

Figure 3.4 SU-8 photoresist pattern process.

To allow easy striping of the SU-8 photoresist, MicroChem's OmniCoat should be coated on the BST thin films before the SU-8 photoresist is spun. The OmniCoat is coated on a spinner and baked on a hotplate. For better coating fidelity and reduced edge bead, ramping and stepping the soft bake temperature is recommended [58]. After that, the SU-8 photoresist is spun onto the sample at 1500 rpm, and then the sample undergoes a hotplate bake to remove solvent. The sample is then exposed through a chrome-glass mask to polymerize the SU-8 photoresist pattern. After exposure, a post bake is performed on a hotplate to selectively cross-link the exposed portions of the sample. After that, SU-8 photoresist is developed by MicroChem's developer. The sample is then rinsed briefly with isopropanol, and dried with an N_2 gun. Finally, the OmniCoat is removed by wet removal using MCC 101 developer and Microposit MF 319. The metallization process is then carried out using a standard lift-off process, followed by E-beam evaporation of 2.5 μm thick Cr/Cu/Au metal stack as described in the previous section. After the lift-off process using MicroChem's remover PG, the OmniCoat is then

removed again by wet removal and/or O_2 plasma removal. One example of fabricated interdigital capacitors is shown in Figure 3.6.

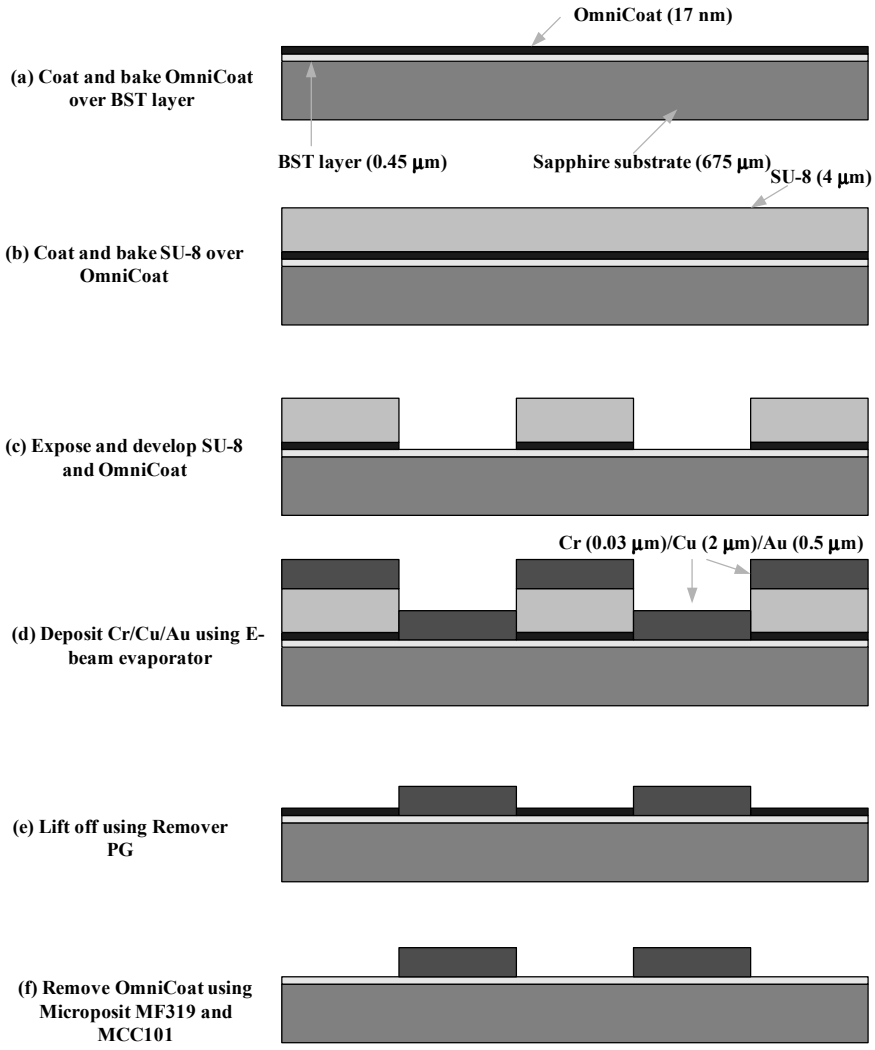

Figure 3.5 Metallization process using SU-8 photoresist.

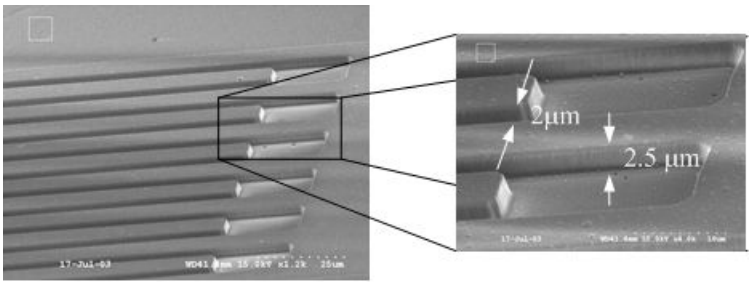

Figure 3.6 SEM image of the 2 µm IDC using SU-8 photoresist.

3.2.2 Air Bridges

So far, the top electrodes fabrication steps have been discussed using two different types of photoresists. The next step entails patterning air bridges incorporated into spiral inductors and the Lange coupler. A overview of the fabrication steps is shown in Figure 3.7. To obtain air bridge structures, a thick layer of photoresist (about 10 μm) is spun on the substrate and patterned to open posts of air bridges. This photoresist is also used as the sacrificial layer, which is the layer removed near the end of the fabrication process. Then, a thin Ti/Cu seed layer is formed to the entire substrate by DC sputtering, as indicated in Figure 3.7(a). Next, a second coating of photoresist is applied and patterned to allow the subsequent Cu electroplating, as shown in Figure 3.7(c). Finally, a lift-off process using acetone can remove the top level of photoresist, and the Ti/Cu seed layer is etched to release air bridge structures using hydrofluoric (HF) for Ti and sulphuric acid (H_2SO_4) for Cu in Figure 3.7(d). After the etching of the seed layer, the second level of photoresist is removed by applying acetone again. Then the air bridges are examined using a scanning electron microscope (SEM). Photographs taken with the SEM can be seen in Figure 3.8, clearly indicating air bridges. More details of the fabrication process are outlined in the Appendix.

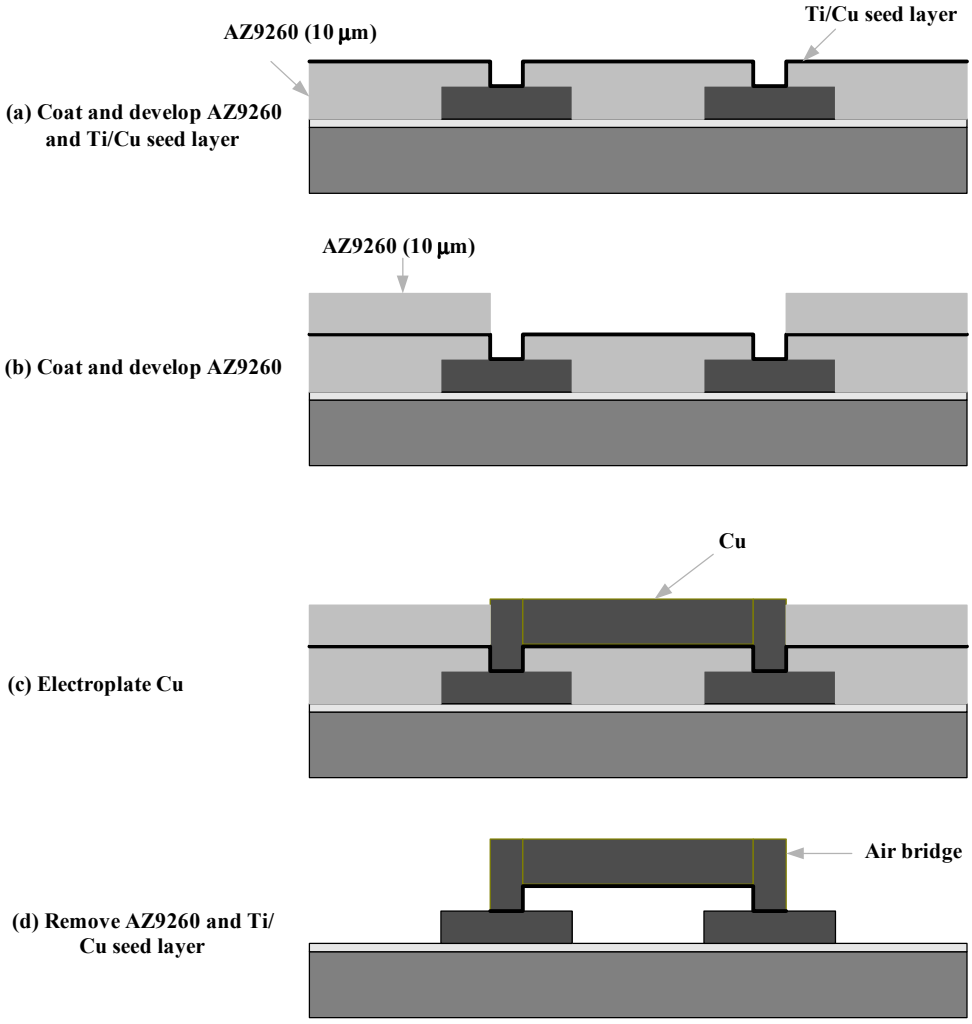

Figure 3.7 Simplified air bridge fabrication step.

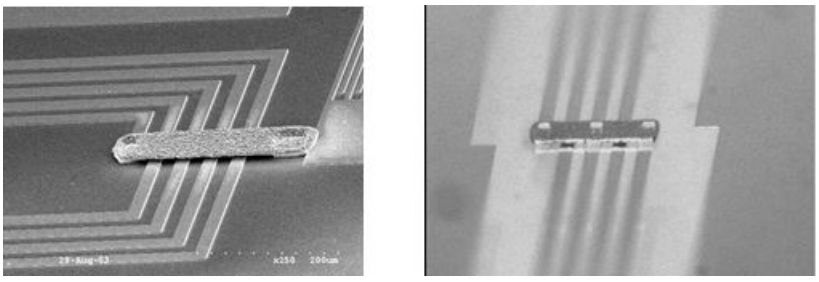

(a) (b)

Figure 3.8 Photomicrograph of air bridges. (a) Spiral inductor. (b) Lange coupler.

3.3 CONCLUSIONS

BST thin film deposition methods and metallization processes were discussed in this chapter. Compared with conventional deposition processes, the CCVD process provided relatively high-quality BST thin films with low cost in the absence of expensive vacuum systems. Details of metallization processes based on BST coated sapphire substrates were discussed as well. Two different types of photoresists were used to complete top electrodes, depending on the minimum feature size of the pattern. The process of creating air bridges, which are incorporated into the spiral inductors and the Lange couplers, was described as well. Photographs taken from the SEM clearly indicated the minimum feature size of 2 μm for IDCs and the presence of air bridges.

CHAPTER IV

BST DEVICE IMPLEMENTATION AND CHARACTERIZATION

An accurate characterization of materials and their high-frequency performance must precede our embarking upon the design of phase shifters. Although the main research topic is the design and implementation of phase shifters, it is reasonable to first characterize BST thin films. In this chapter, investigations of coplanar waveguides (CPWs) and interdigital capacitors (IDCs) will be discussed with respect to their small and large signal characteristics. The temperature sensitivities of various compositions and geometries of BST thin films also will be discussed. In addition, the characteristic of inductors on BST thin films and the use of gap capacitors to improve their dynamic range will be introduced as well.

4.1 *S*-PARAMETER MEASUREMENT AND CALIBRATION

In order to measure the *S*-parameters of one- or two-port devices under high bias conditions, careful test setup should be considered. The test setup shown in Figure 4.1 is representative of on-chip *S*-parameter measurement for a high bias. Measurements are accomplished using an HP-8753C vector network analyzer with Cascade Microtech's standard Air Coplanar G-S-G probe tips (150 μm pitch size). To apply a high bias voltage for one-port device under test (DUT), an external bias tee from KDI/TRIANGLE Corp., of which the minimum breakdown voltage is 300 V, is used. Also, a Cascade Microtech Summit 9101 probe station equipped with a thermal chuck connected to a thermal control

unit is used to sweep temperature from 0°C to 100°C as well as to measure *S*-parameters. The measurement of two-port devices is carried out using the same equipment with an additional DC block capacitor to protect a network analyzer from bias voltage leakage in the case of a bias voltage short. The measurement is calibrated with short-open-load-through (SOLT) using the impedance standard substrate of a Cascade Microtech. This calibration is done after applying a DC block capacitor and a bias tee so that the effects associated with these parts can be removed. It is worth noting that in the case of the phase-shifter measurement, bias voltage is applied through a DC bias pad and a bias network that are embedded in the phase shifter. The result is that two identical DC block capacitors are inserted between the phase shifter and network analyzer without an external bias tee.

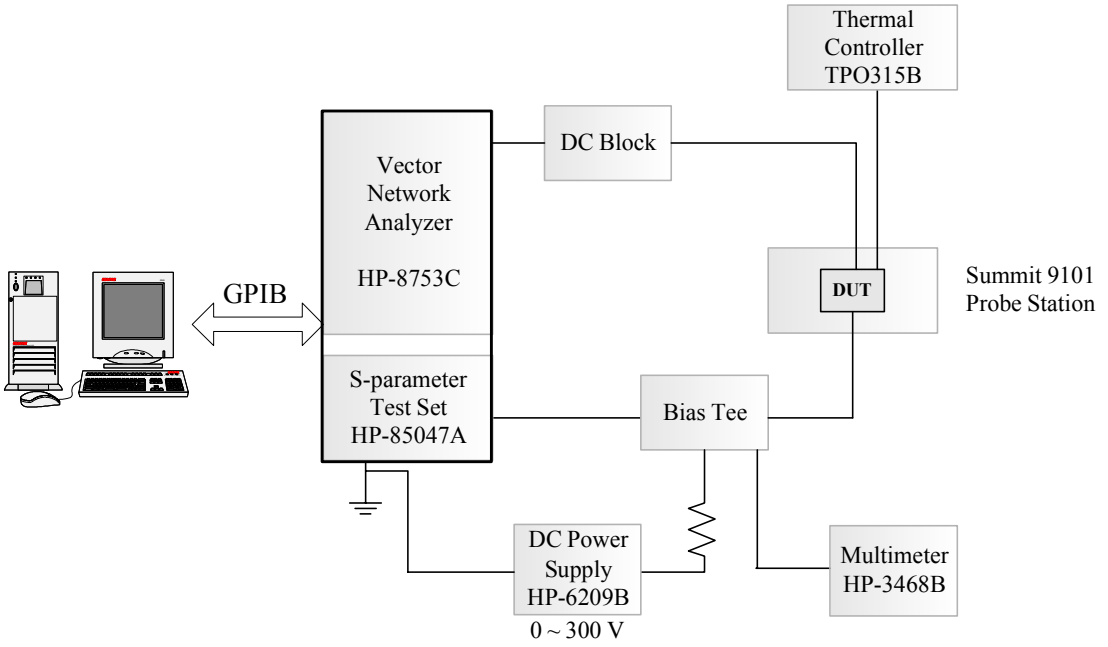

Figure 4.1 *S*-parameter on-chip test setup.

4.2 COPLANAR WAVEGUIDES (CPWS) ON BST COATED SUBSTRATES

The first challenge in characterizing high-permittivity BST thin films is the uniplanar concept of coplanar waveguide (CPW). The CPW proposed by C. P. Wen in 1969 was composed of a dielectric substrate with a center strip conductor and semi-infinite ground planes on the top surface [59]. The CPW structure can support a quasi-TEM mode like a microstrip line. Even though a microstrip line is one of the most popular types of planar transmission lines, CPW is chosen to analyze BST thin films because it provides several preferences such as higher concentration of the electric field and more efficient utilization of BST thin films. In order to obtain BST thin-film properties such as high permittivity, electric field dependent tunability, and dielectric loss, various CPWs were fabricated and tested. As indicated in Figure 2.6, the permittivity of the BST thin films can be changed by simply applying a bias voltage between a signal line and ground planes, perpendicular to the direction of propagation of RF signals. The characteristic impedance and tunability depend on the geometry of CPWs, and thus various line width and spacing are used here. For instance, in the case of small spacing between a signal line and ground planes, a very high electric field is achievable, resulting in high tunability. As a result, CPWs based on BST thin films are the simplest configuration to implement a phase shifter as well as to characterize their material properties.

Figure 4.2 shows a photomicrograph of fabricated 5 mm-long CPWs with various line width and spacing. These eight different CPWs were measured to extract the characteristic impedance, loss, and variation associated with specific bias voltages and geometries. Material parameters are as follows: a 500 nm-thick BST thin film, a Ba/Sr ratio of 1.33, a (Ba+Sr)/Ti ratio of 1.0, and a 430 μm-thick sapphire. The measured

performance is shown in Figure 4.3. Total loss and loss variation with respect to bias voltage decreases with increased line width while retaining a characteristic impedance of around 56 Ω. However, a bias-dependent tunability increases with smaller spacing because of higher electric field. Figure 4.4 illustrates the tunability of CPWs with a line width of 5 μm and spacing of 10 and 30 μm. A change of the effective dielectric constant is more than 52 % on a 5/10 structure, whereas it is 21 % on a 5/30 structure with 250 V. As expected, in the case of smaller spacing, higher electric field strengths are achievable that allow higher tunability.

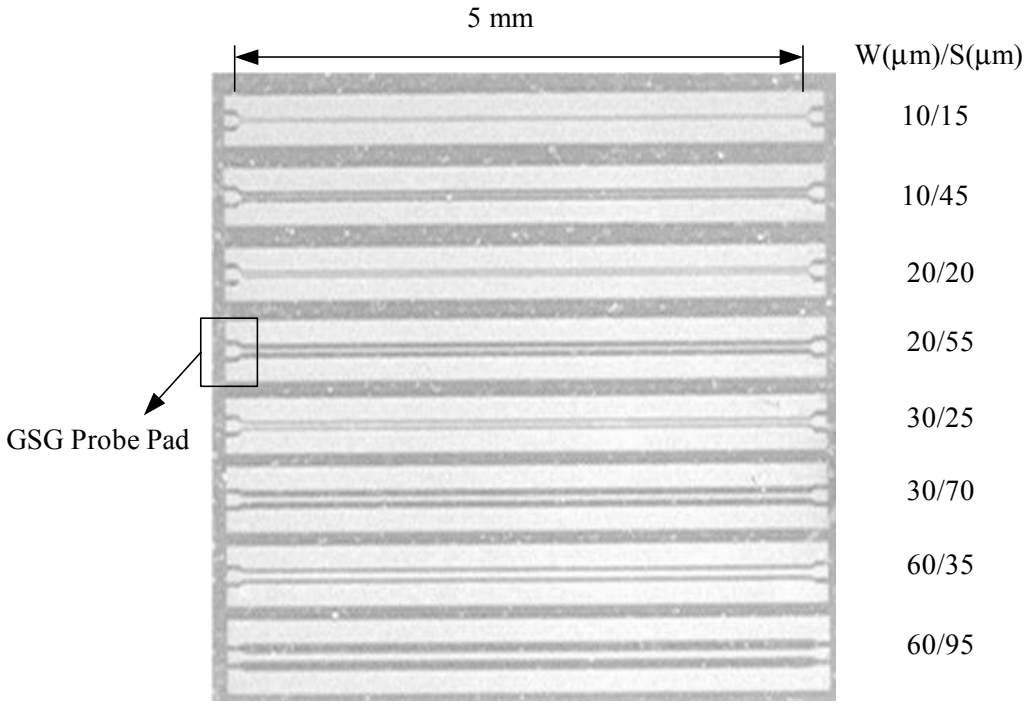

Figure 4.2 Photomicrograph of the fabricated CPWs.

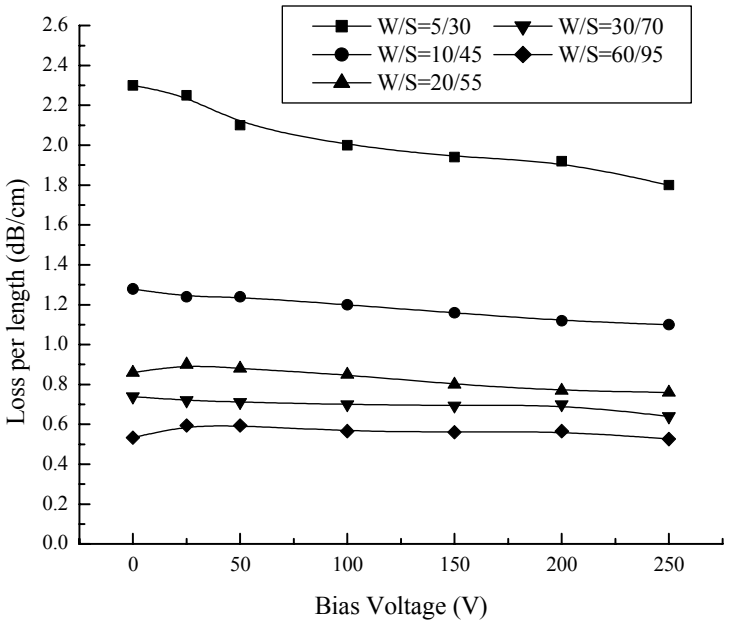

Figure 4.3 Loss and loss variation of various CPWs.

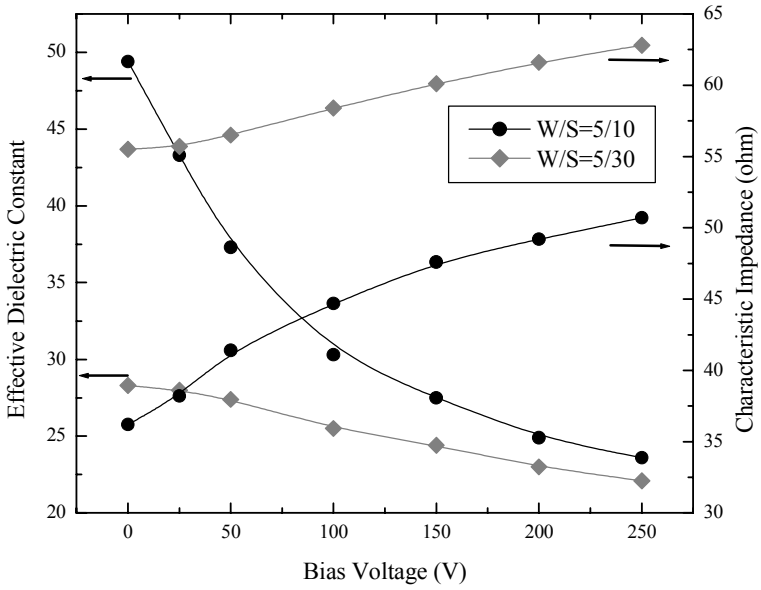

Figure 4.4 Effective dielectric constant and characteristic impedance for two different CPWs.

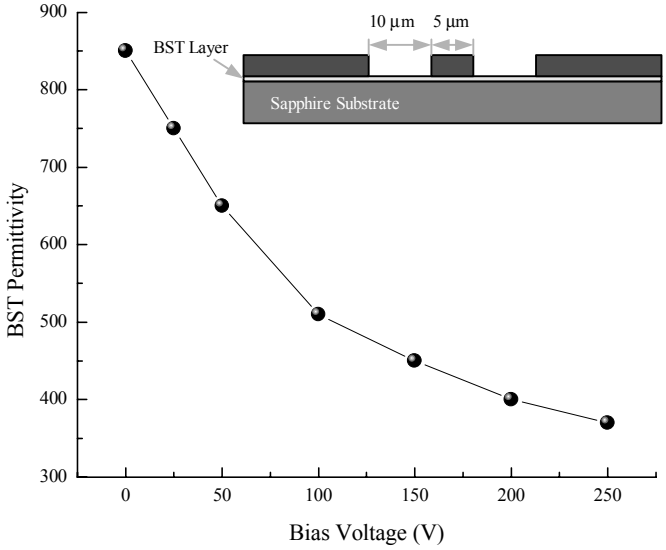

Figure 4.5 BST permittivity as a function of bias voltage for a 5/10 structure.

The permittivity of BST thin films can be extracted from the Method of Moment (MoM) simulation [60] by varying the dielectric constant of BST thin films to give the best fit to measured data. It was found that the permittivity of BST thin films is around 850 at 0 V and the variation of the permittivity exceeds 56 % with 250 V, as shown in Figure 4.5. It should be noted that the extracted variation of the permittivity is slightly higher than that of the effective dielectric constant in Figure 4.4 because the effective dielectric constant is constituted from the air as well as the substrate. Based on these material parameters, a CPW-based coupler including either a branch-line coupler or a Lange coupler would be designed as part of a reflection-type phase shifter.

4.3 INTERDIGITAL CAPACITORS (IDCS) ON BST COATED SUBSTRATES

The phase control element of analog phase shifters based on BST thin films is a varactor. In a distributed structure, capacitance can alter the phase velocity of the propagating wave by changing the permittivity on BST layers. In a reflection-type structure, the phase variation of reflected signals from reflective terminations can occur by BST varactors.

As we discussed in Chapter 2, two different types of varactors are widely available for BST technology. Interdigital capacitors (IDCs) were chosen for this research because they are simpler to fabricate and integrate into other devices by directly metallizing top electrodes onto BST thin films, as illustrated in the previous chapter. Although they suffer from high control voltages because of relatively large fringing electric fields in the air, they provide higher linearity of the devices that is proportional to bias voltage. By using small spacing between adjacent fingers in the IDCs, we can further reduce bias voltage down to the comparable voltage for parallel plate capacitors. Figure 4.6 shows the scanning electron microscopy (SEM) image of one of the fabricated 2 μm-spaced IDCs.

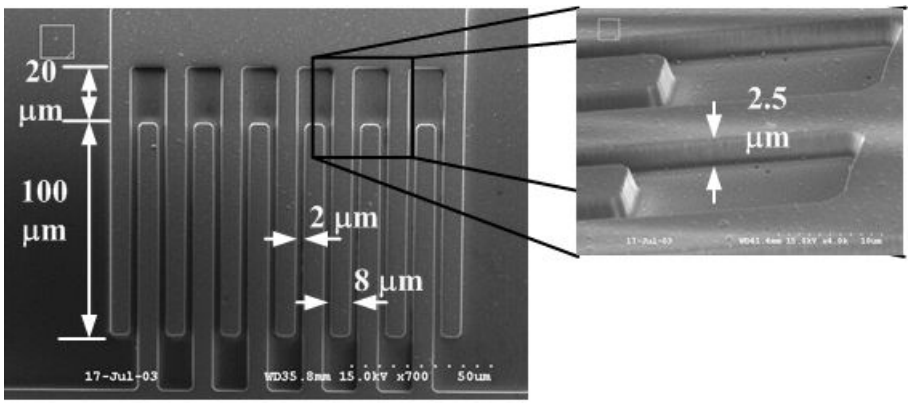

Figure 4.6 SEM image of the fabricated interdigital capacitor.

Capacitance and Q-factor in the high-frequency range were extracted using an equivalent circuit model with open and short circuit structures to account correctly for pads and parasitics [61]. Measured capacitor admittance Y_m is corrected using parallel stray admittance Y_{op} and series stray admittance Y_{sh} to obtain intrinsic capacitor admittance Y_c, as shown in Figure 4.7. Y_c can be expressed by

$$Y_c = \frac{(Y_m - Y_{op})(Y_{sh} - Y_{op})}{Y_{sh} - Y_m} = G + i\omega C, \tag{4.1}$$

where G and C are conductance and capacitance of the intrinsic capacitor. Also, Q-factor can be calculated as the ratio of G and ωC.

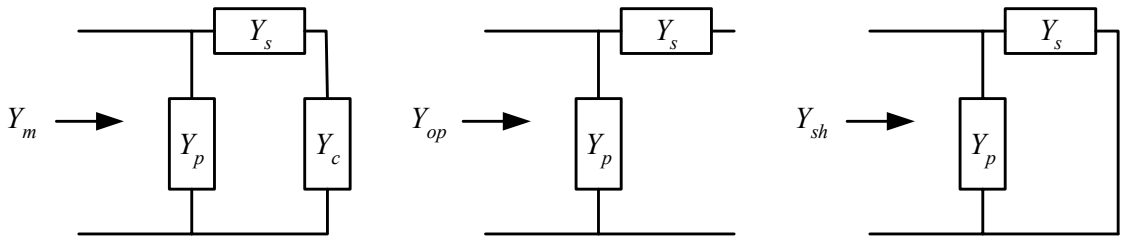

(a) (b) (c)

Figure 4.7 Equivalent circuits by lumped element expression. (a) Capacitor under test. (b) Open circuit. (c) Short circuit proposed by K. Ikuta, *et al.* [61].

Figure 4.8 shows the typical frequency characteristics of capacitance under six different bias conditions that involve open- and short-circuit structures. The capacitor has 13 fingers, all of which are 390 μm long. The spacing between adjacent fingers is 4 μm. Measurement using the open- and short-circuit structures reveals that the capacitance is constant throughout the entire frequency range measured.

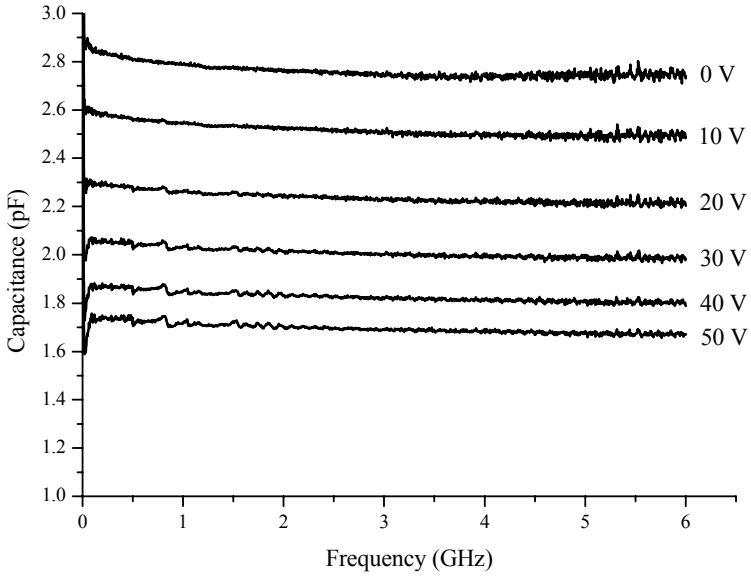

Figure 4.8 Capacitance as a function of frequency for the capacitor with 13 fingers.

4.3.1 Influence of Geometry

Given that the BST composition and thickness are determined, the only way to achieve the desired values of capacitors is by controlling the geometry of IDCs through line width, line length, number of fingers, and spacing between adjacent fingers. Among these alternatives, the most critical parameter is the spacing between adjacent fingers because this largely determines electric field strengths, which govern the capacitance and tunability of IDCs. Therefore, in this section, we investigate the properties of the capacitors associated with different spacings and numbers of fingers.

Figure 4.9 shows the capacitance, tunability, and Q-factor of the capacitors with different numbers of fingers as a function of bias voltage at 2.4 GHz. The dimensions of the capacitors are: line width = 8 μm, spacing = 4 μm, and line length = 390 μm. From the measured data, it is determined that the capacitors have almost same tunability of 3.1

and a maximum Q-factor of 55 ~ 60 with a bias voltage of 140 V regardless of the number of fingers. As expected, the capacitance increases as the number of fingers increases. In this case, the material parameters are as follows: a 450 nm-thick BST thin film, a Ba/Sr ratio of 1.33, a (Ba+Sr)/Ti ratio of 1.0, and a 430 μm-thick sapphire.

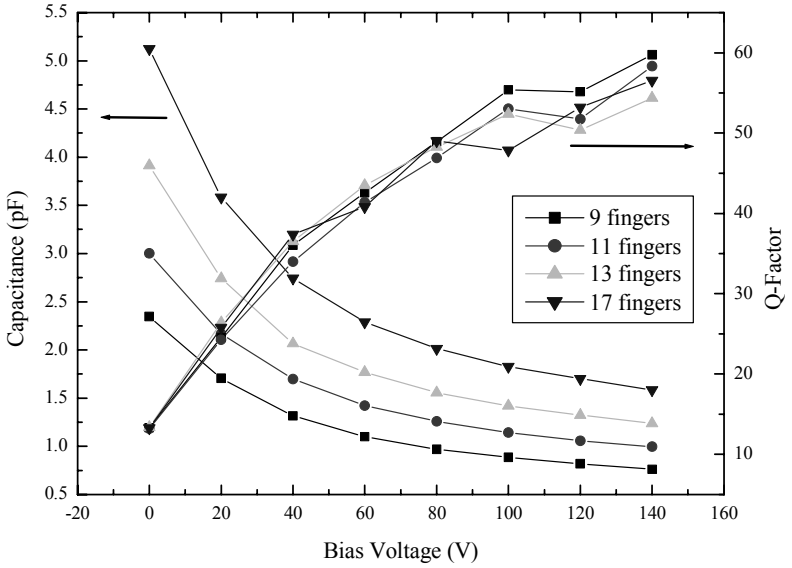

Figure 4.9 Capacitance and Q-factor as a function of bias voltage for capacitors with 9, 11, 13, 17 fingers.

In the case of 4 μm-spaced IDCs, more than 140 V is required to achieve a reasonable amount of tunability (~3), as shown in the previous figure. If, however, we shrink the spacing between adjacent fingers, we can further reduce bias voltage to a relatively low number because of the very high electric field strength [62]. The measured results of IDCs with three different spacings are shown in Figure 4.10. The dimensions of the capacitors are as follows: line width = 8 μm, spacing = 2, 3, or 4 μm, and line length = 100 μm. The 2 μm-spaced IDC has a tunability of 2.6, whereas the 4 μm-spaced IDC has

below 1.6 with 80 V. Because the electric field concentration in BST thin films increases with narrower spacing of the capacitors, the 2 μm-spaced IDC has much higher tunability than the 4 μm-spaced IDC. In this case, the BST composition is the same as the previous one, but the BST thickness is 350 nm, resulting in a tunability of less than 3. This result, however, can show a way to reduce bias voltage. It seems to be reasonable that if we shrink the spacing between fingers to 1 μm or to sub-micron dimension, we can achieve high tunability from an interdigital structure with a lower bias voltage that is comparable to BST parallel plate capacitors and varactor diodes. However, it should be kept in mind that reducing bias voltage creates increased nonlinear distortion; consequently the dynamic range of varactors is suppressed. One approach to improve linearity without increasing bias voltage is the so-called reduced IMD capacitor [63]. A separate bias structure is inserted between the spacing of a conventional gap capacitor, and thus the RF signal can be effectively isolated by the bias structure. This capacitor will be discussed in more detail in the last section of this chapter.

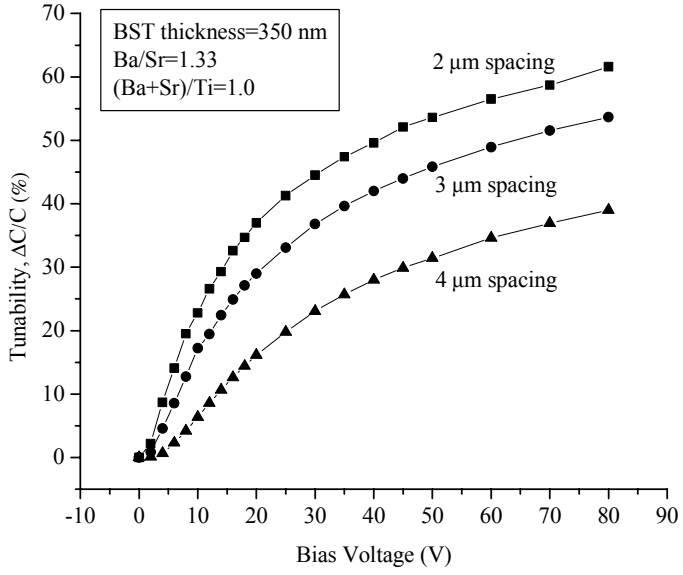

Figure 4.10 Tunability as a function of bias voltage at 2.4 GHz.

4.3.2 Effect of BST Composition and Thickness

The electrical properties of BST thin films are mainly determined by two factors: BST composition and thickness. Although the geometry of IDCs can control their electrical properties with particular BST coated substrates, the more critical factors are their inherent composition and thickness. Therefore, it is worth investigating the capacitance, tunability, and Q-factor associated with various BST compositions and thicknesses.

First, the thickness dependence of BST IDCs was investigated. The variation of the capacitance, tunability, and Q-factor as a function of bias voltage with two different BST thicknesses is seen in Figure 4.11. In this case, the spacing and length of the capacitors are 4 μm and 390 μm, respectively. By applying a bias voltage up to 140 V, a tunability of more than 2.6 is achieved by the capacitors with the 450 nm-thick BST thin film. Also, the capacitance and tunability of the capacitors with the 450 nm-thick BST thin film are much higher than those on the 350 nm-thick BST thin film because of higher permittivity and electric field concentration. The latter has, however, a higher Q-factor (from 25 to over 80) than the former. Therefore, it is apparent that capacitance and Q-factor involve a tradeoff, and thus intended application should be considered in choosing the appropriate BST thickness.

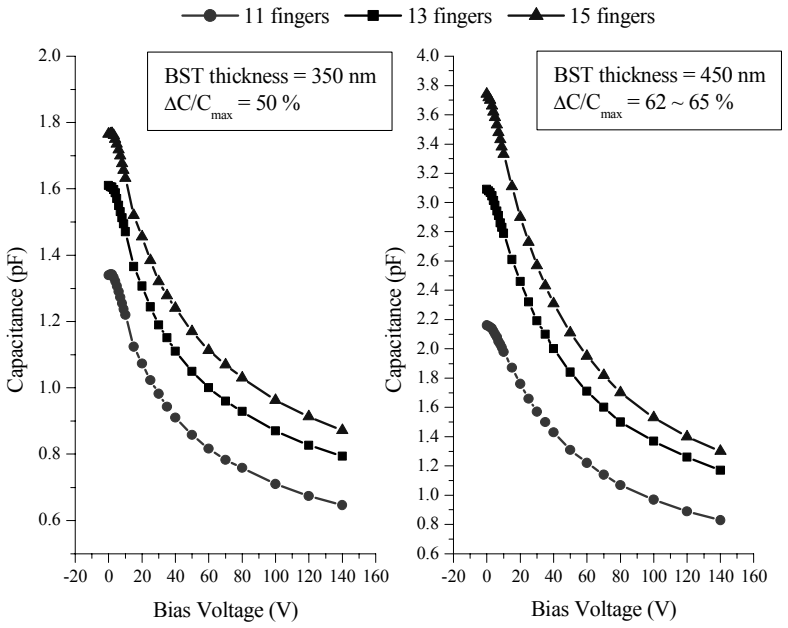

(a)

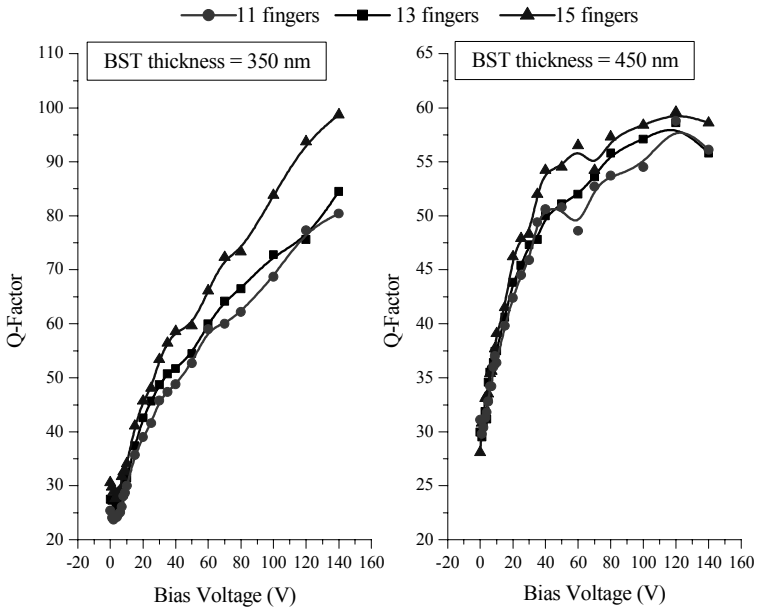

(b)

Figure 4.11 Measured results for the capacitors with two different thicknesses at 2.4 GHz as a function of bias voltage. (a) Capacitance and tunability. (b) Q-factor.

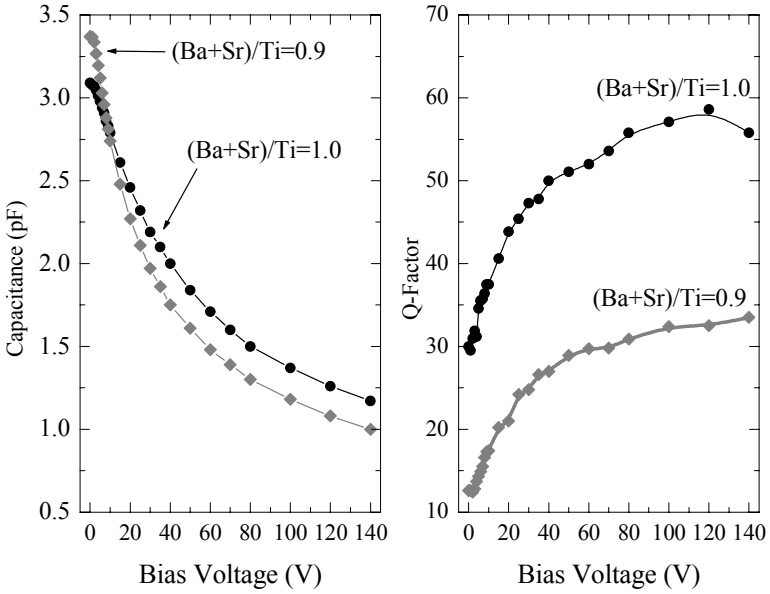

Figure 4.12 Capacitance and Q-factor for capacitors with different (Ba+Sr)/Ti ratios.

Second, the (Ba+Sr)/Ti ratio dependence of BST IDCs was studied. Depending on the (Ba+Sr)/Ti ratio, the capacitance, tunability, and Q-factor differ as well. The measured results of IDCs with two different (Ba+Sr)/Ti ratios are shown in Figure 4.12. The tunabilities of the capacitor with a (Ba+Sr)/Ti ratio of 1.0 and a (Ba+Sr)/Ti ratio of 0.9 are 2.6 and 3.4, respectively. Although the tunability of the former is lower than that of the latter, the Q-factor of the former is much higher than that of the latter.

The permittivity of the BST thin film can be calculated with the given thickness of BST thin film and sapphire, the dielectric constant of sapphire, and the geometry of the IDC employing a conformal mapping-based model for multilayered substrates [64]. Applying a constant bias voltage of 140 V, a relative change in BST permittivity of more than 4.2 is achieved on the capacitor with a (Ba+Sr)/Ti ratio of 0.9, whereas the change is more than 3.1 on the capacitor with a (Ba+Sr)/Ti ratio of 1.0, as shown in Figure 4.13.

The extracted variation of the BST permittivity is slightly higher than the actual capacitance tunability because the capacitance is constituted from the air as well as the substrate. The maximum permittivity of BST thin film detected at zero bias is more than 700 with a (Ba+Sr)/Ti ratio of 0.9 and more than 650 with a (Ba+Sr)/Ti ratio of 1.0. Compared with the extracted permittivity in Figure 4.5, the BST permittivity is relatively low because of the thinner BST layer.

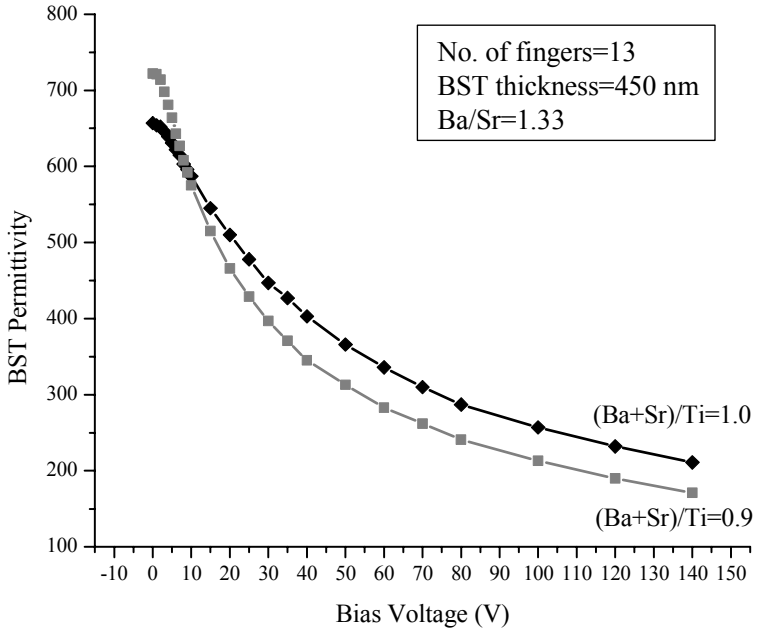

Figure 4.13 BST permittivity for capacitors with different (Ba+Sr)/Ti ratios.

Finally, the (Ba+Sr)/Ti ratio dependence of BST IDCs was investigated. Figure 4.14 shows the measured results of 15-finger IDCs with two different compositions of BST thin films. In this case, both BST coated substrates were N_2 atmosphere for 3 hours to increase the tunability and permittivity of BST thin films [65]. From the measured data, the maximum capacitance detected at zero bias decreases with the decreased Ba/Sr ratio,

while the Q-factor increases with the decreased Ba/Sr ratio. Therefore, depending on application, we should consider in choosing the appropriate composition. These BST composition and thickness have an effect on variation over temperature as well. Details of temperature response will be discussed in the following section.

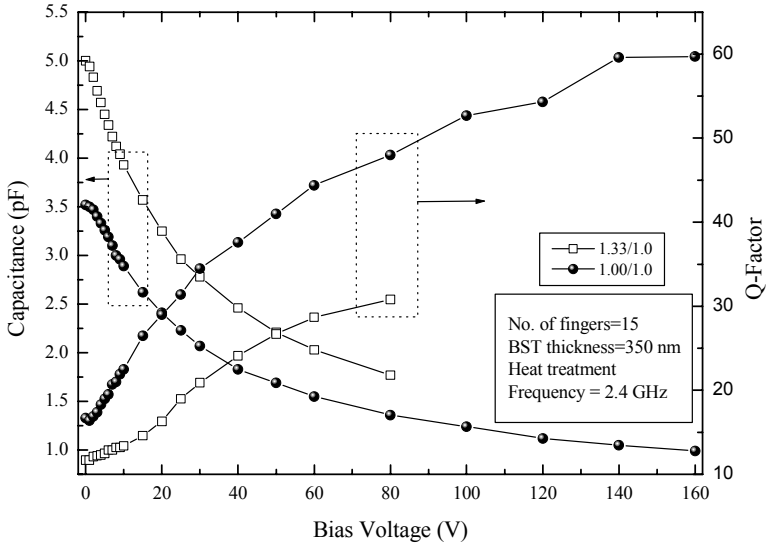

Figure 4.14 Measured capacitance and Q-factor with two different compositions of BST thin films.

4.3.3 Characterization over Temperature

So far, we have investigated the electrical properties of various BST thin films using CPWs and IDCs at room temperature. Reaction to temperature variation is another way to characterize these materials. Several groups have investigated the temperature dependence of BST devices. Jackson *et al*. [15] and Kozyrev *et al*. [18] have reported the temperature response of devices with STO thin films which have the Curie temperature of below 0 K (-273°C). Because tunability is highest when devices are operated near the

Curie temperature, and very low tunability is revealed at room temperature, these STO films are not applicable to RF devices for operation in the commercial temperature range. The temperature response of BST thin films has been reported as well. Parker *et al*. [66] have investigated temperature dependence of BST permittivity, and Gevorgian *et al*. [67] have reported a method to reduce variation over temperature using two different Ba/Sr ratios.

In this section, we investigate the temperature dependence of IDCs fabricated on several compositions and thicknesses of BST thin films. Once a suitable composition of BST thin film is chosen to minimize variation over temperature, we will then investigate circuit topologies to minimize phase-shift and loss variation over temperature. Based on these investigations, we will discuss details of the phase-shifter design that is optimized to be robust over commercial operating temperature ranges.

In order to find the best composition with respect to minimum variation over temperature, capacitors with five different compositions were considered. The BST thin films were treated by heat in a conventional furnace at 550°C for 3 hours in an N_2 atmosphere [65]. We fabricated five 4 μm-spaced IDCs with 15 fingers, and a bias-dependent tunability of more than 3 at room temperature was obtained with these five IDCs. Table 4.1 shows capacitance variation over temperature of five capacitors. With a (Ba+Sr)/Ti ratio of 0.8, the variations (C_{max}/C_{min}) of capacitors with Ba/Sr ratios of 0.8, 1.0, and 1.2 are 1.59, 1.33, and 1.17, respectively, in the temperature range of 0°C - 80°C. This implies that the variation over temperature continuously increases with the decreased Ba/Sr ratio because the temperature at which the maximum capacitance occurs shifts down as the Ba/Sr ratio decreases. Also, with a Ba/Sr ratio of 1.2, this temperature

is around room temperature and considerably broadened from 0°C to 80°C, and thus the variation is minimized.

Table 4.1 Capacitance variation of 15-finger IDCs at 2.4 GHz.

BST composition and thickness			C_{max}/C_{min} (0°C ~ 80°C)
Ba/Sr	(Ba+Sr)/Ti	Thickness	
0.8	0.8	250 nm	1.59
1.0	0.8	250 nm	1.33
1.2	0.8	250 nm	1.17
1.0	1.0	350 nm	1.55
1.33	1.0	350 nm	1.32

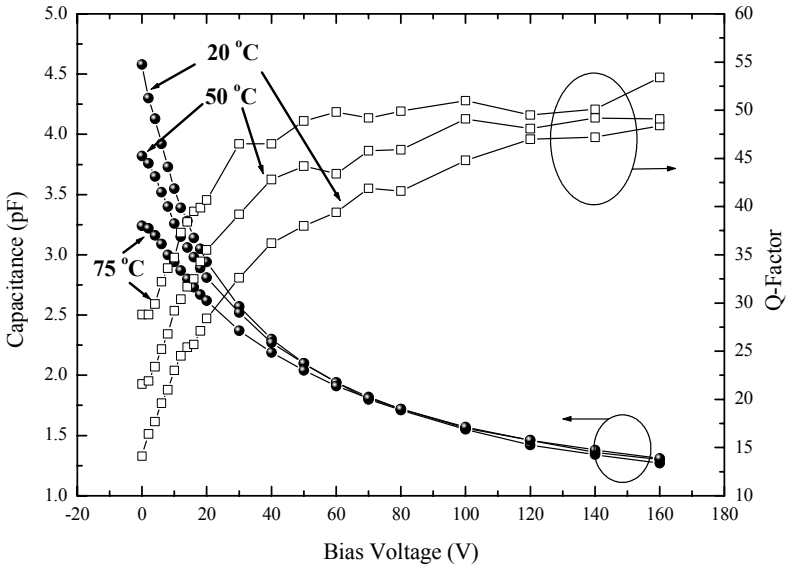

Figure 4.15 Capacitance and Q-factor as a function of bias voltage. (Ba/Sr=1.0, (Ba+Sr)/Ti=1.0)

The capacitance at three different temperature states keeping the temperature constant and changing bias voltage is shown in Figure 4.15. In this case, a capacitor with a Ba/Sr ratio of 1.0, (Ba+Sr)/Ti ratio of 1.0, and BST thickness of 350 nm was used. The

tunability of the capacitor at 20°C is more than 3.6 while the tunability at 75°C is less than 2.5. Also, a maximum capacitance at each temperature state is quite different. The variation over temperature is relatively high compared with the results of 250 nm-thick BST in Table 4.1 but is relatively low compared with the result of 450 nm thick BST in [34]. Therefore, we can conclude that as the BST thin films become thinner, and then the variation over temperature becomes lower and broader.

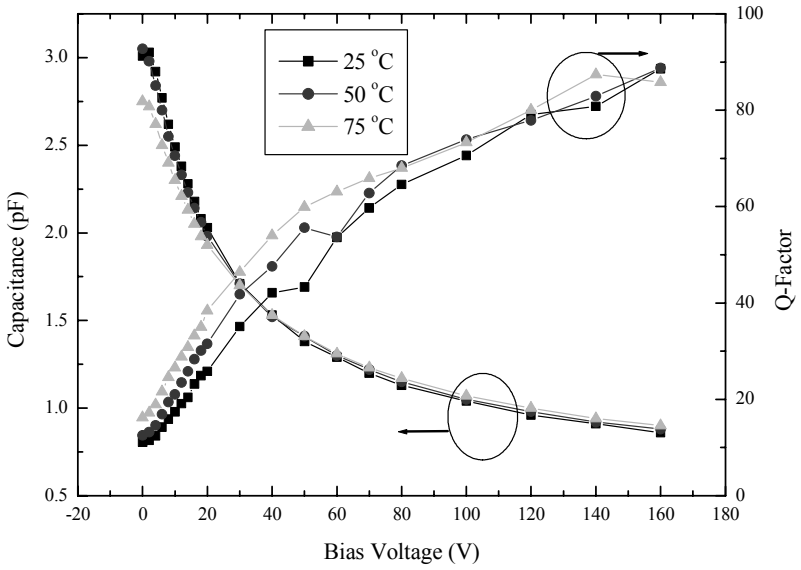

Figure 4.16 Capacitance and Q-factor as a function of bias voltage. (Ba/Sr=1.2, (Ba+Sr)/Ti=0.8)

A capacitor with a Ba/Sr ratio of 1.2, (Ba+Sr)/Ti ratio of 0.8, and BST thickness of 250 nm was measured as a function of bias voltage at three different temperature states as well. Tunabilities of 3.5, 3.46, and 3.05 were obtained at 25°C, 50°C, and 75°C, respectively, as shown in Figure 4.16. The measured Q-factors of the capacitor were also revealed to have small variation with this composition. From five different BST

compositions and thicknesses that we considered here, we found that the BST thin film with a Ba/Sr ratio of 1.2, (Ba+Sr)/Ti ratio of 0.8, and BST thickness of 250 nm provides the lowest variation over temperature along with a bias-dependent tunability of more than 3.

4.3.4 IDC Modeling

BST IDCs can be represented by a lumped-element equivalent model with four parameters, as shown in the inset in Figure 4.17: pure capacitance C_p, parasitic inductance L_s, parallel resistance $R_p(f)$, and series resistance $R_s(f)$. These four parameters are extracted by varying the values to fit the measured capacitance and Q-factor Q_m from 3 MHz to 6 GHz. First, C_p and L_s, which are dominant at the low- and high-frequency ranges, respectively, are obtained to fit the measured capacitance. Once both values are fixed, then the other two parameters $R_p(f)$ and $R_s(f)$ are extracted from Q_m. The series resistance, which accounts for the conductor loss, depends on a conductor thickness, conductivity, and geometry of the capacitor. This series resistance can be expressed as

$$R_S(f) = \alpha \frac{L}{\sigma \delta W N} \left(1 - e^{-\beta t/\delta}\right)^{-1}, \tag{4.2}$$

$$\delta = \sqrt{\frac{2}{\omega \mu \sigma}}, \tag{4.3}$$

where L, W, and N represent the line length, line width, and number of fingers, respectively. Also, σ is the conductivity of the metal, δ is the skin depth, t is the metal thickness, and μ is the magnetic permeability. The above equations clearly show that the series resistance is frequency dependent and becomes dominant as the frequency increases. As described in Chapter 3, however, in this research, three different metals Cr,

Cu, and Au were deposited on BST thin films and their conductivities are not ideal as well. Therefore, the fitting parameters α and β are used to give better fit to the measured data.

The parallel resistance is involved in leakage resistance and dielectric resistance. The leakage resistance caused by leakage current in the capacitor is usually negligible except at very low frequencies. Assuming a constant loss tangent over the measured frequency range, a dielectric resistance, however, is frequency dependent. This parallel resistance can be expressed as

$$R_p(f) = \frac{R_p}{\gamma + f(GHz)}, \tag{4.4}$$

where γ is the fitting parameter related to the leakage resistance, and its value is around 0.01. Based on the above three equations, Q-factors associated with the series and parallel resistances are extracted from the total Q-factor Q_t by changing fitting parameters α, β, and γ. With an increase of frequency, $R_s(f)$ increases enormously and becomes dominant. On the other hand, $R_p(f)$ is dominant at the low-frequency range, and thus we can extract both Q_c and Q_d from Q_t to fit Q_m. The relation between Q_t and Q-factors related to the series and parallel resistances is

$$Q_t = \left(\frac{1}{Q_c} + \frac{1}{Q_d} \right)^{-1}, \tag{4.5}$$

$$Q_c = \frac{1}{2\pi f C_p R_s(f)} - \frac{2\pi f L_s}{R_s(f)}, \tag{4.6}$$

$$Q_d = \frac{1}{\tan\delta} = 2\pi f C_p R_p(f). \tag{4.7}$$

Figure 4.17 shows the measured and extracted Q-factors as a function of frequency at 0

V. In this case, material parameters are as follows: a 450 nm-thick BST thin film, a Ba/Sr ratio of 1.33, a (Ba+Sr)/Ti ratio of 1.0, and a 675 μm-thick sapphire. The measured capacitance is 3.3 pF at 0V. From Figure 4.17, we can conclude that at the low-frequency range, Q_t is dominant by Q_d which are mainly due to the dielectric loss of BST thin films whereas at the high-frequency range, Q_c mainly contributes to Q_t. In the frequency range of 0.5 GHz – 3 GHz, both Q_d and Q_c contribute to Q_t of the device. Consequently, the improvement of BST thin-film quality and the thicker conductor with higher conductivity will significantly increase the device Q-factor for IEEE 802.11b WLAN applications.

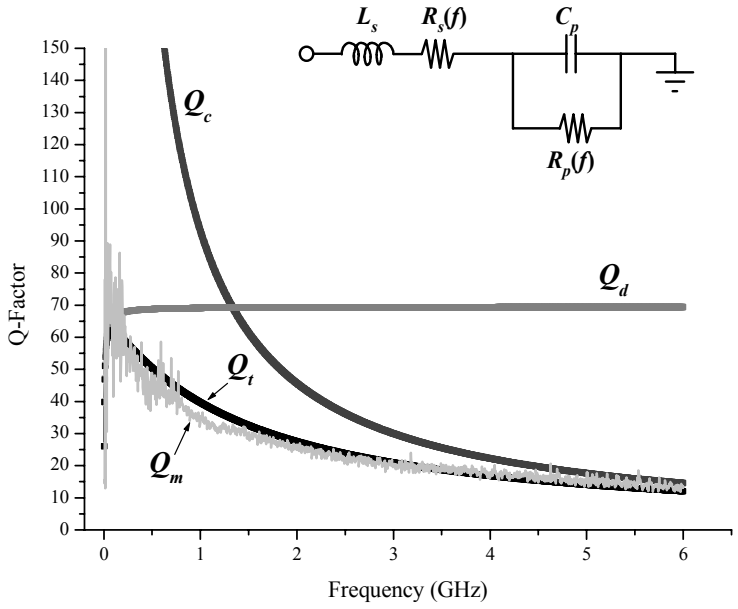

Figure 4.17 Measured and extracted Q-factors from 3 MHz to 6 GHz at 0 V

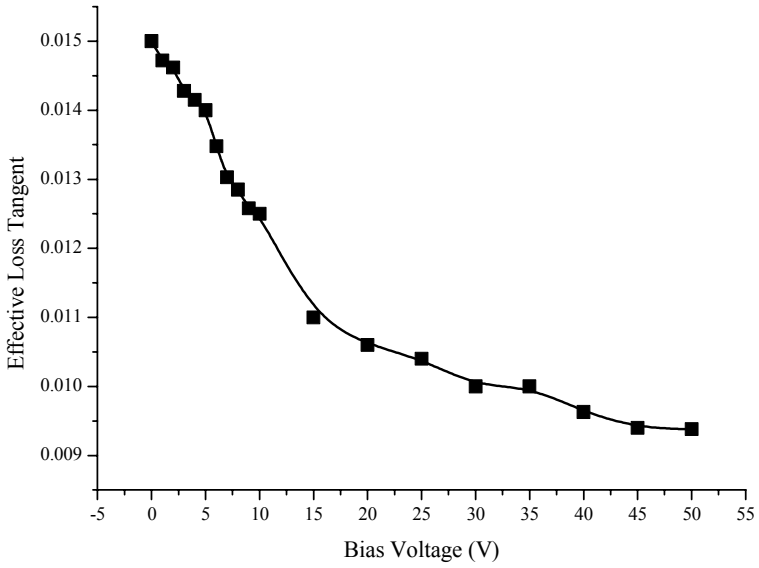

Figure 4.18 Effective loss tangent as a function of bias voltage.

The effective loss tangent for the BST thin film and sapphire substrate can be obtained by an inverse of Q_d. The effective loss tangent from eq.(4.7) as a function of bias voltage is shown in Figure 4.18. The effective loss tangent is in the range of 0.015 - 0.009 from 0 V to 50 V. Typically, the loss tangent of the sapphire substrate is an order of 10^{-4}, showing that the loss tangent of the BST thin film is the main contributor to the effective loss tangent.

4.4 MEANDERED-LINE AND SPIRAL INDUCTORS

As described in Chapter 2, distributed-type phase shifters such as CPWs, microstrips and loaded-line phase shifters can be implemented without inductors. However, these phase shifters may struggle with a large chip size at *S*-band. The best way to reduce overall chip size is by incorporating inductors. It should be kept in mind that one of the major goals of this research is to reduce the size of phase shifters, so that the value of using inductors is

apparent.

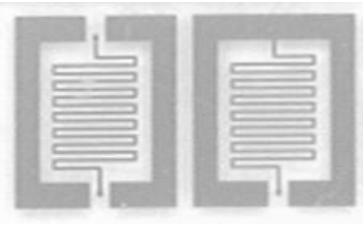

(a)

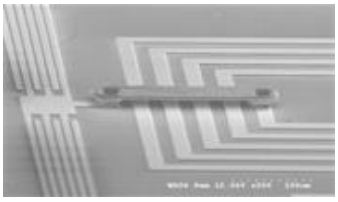

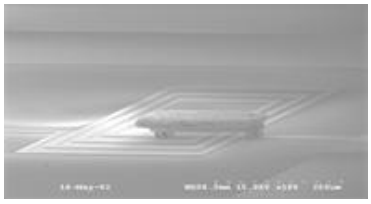

(b) (c)

Figure 4.19 Photomicrograph of (a) meandered-line inductors; (b) & (c) spiral inductors.

Two types of inductors are frequently available: meandered-line inductors and spiral inductors. Figure 4.19 shows photomicrographs of the fabricated meandered-line inductors and square-type spiral inductors. The current of the meandered-line inductor is flowing in opposite directions between adjacent lines, and thus overall inductance is significantly reduced compared with the spiral inductor. On the other hand, the current between adjacent lines in the spiral inductor is flowing in the same direction, resulting in high self-inductance by increasing mutual inductance. However, the major drawback of the spiral inductor is that it requires interconnection between the center of the spiral and the outside. Air bridge crossovers or dielectric spaced underpasses are usually used; in this research, air bridge crossovers were chosen to avoid via holes in the BST coated substrate.

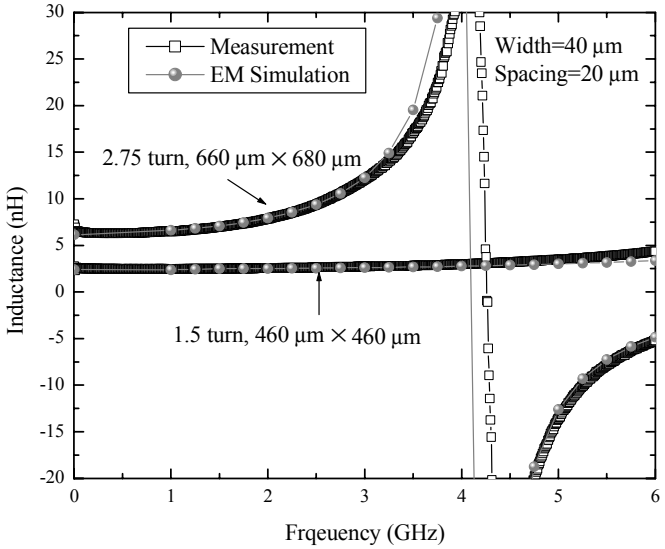

(a)

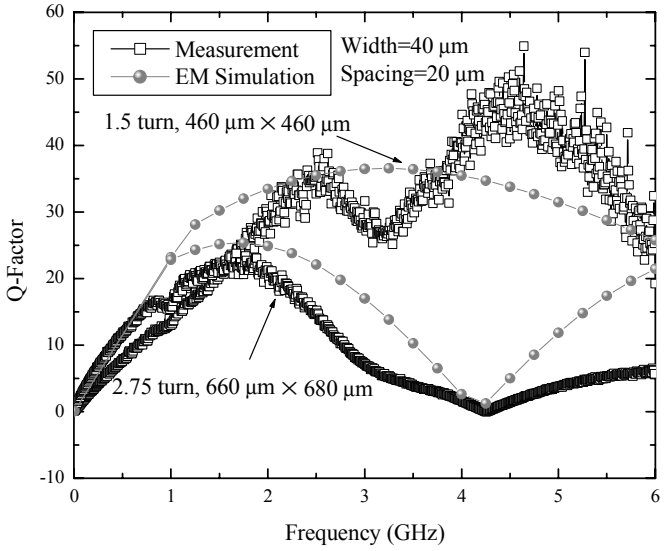

(b)

Figure 4.20 Comparison of measured and simulated performances for spiral inductors.

The initial versions of reflection-type phase shifters have employed meandered-line inductors because of the simplicity of fabrication. However, the rest of the phase-shifter designs have adopted the square-type spiral inductors to capitalize on size reduction and high-self inductance. It is worth noting that square-type spiral inductors are used because they impose fewer layout constraints than the round-type spiral inductor. Typically, the round one would have slightly superior performance at the expense of layout complexity and integration with other components. However, it is found by the EM simulation found no difference in performance at 2.4 GHz between the square one and approximate round one (45°).

The comparison between the measured and simulated results of two different spiral inductors is shown in Figure 4.20. Using the material parameters extracted from the CPWs and IDCs described in the previous sections, EM simulation was performed, resulting in good agreement with the measured values from 3 MHz to 6 GHz. In this case, the line width is 40 μm and the spacing between lines is 20 μm.

A small-signal spiral inductor model mainly comprise a series inductance, resistance, inter-wire coupling capacitance, and shunt parasitic capacitances between traces and ground planes. The ground plane is placed 140 μm apart from the edges of the spiral inductors for on-wafer measurement, and thus we can neglect shunt parasitic capacitances. With increase of frequency, the effective inductance increases because of the inter-wire coupling capacitance, resulting in no more inductance at a specific frequency, the so-called self-resonant frequency (SRF). Small-signal parameters, SRFs, and maximum Q-factors for several types of inductors are shown in Table 4.2. Clearly the meandered-line inductors occupy a large chip area with small inductances. The maximum Q-factor of

inductors that can be achieved on the BST coated sapphire substrates is around 45 at 4.5 GHz with inductance of 2.5 nH.

Table 4.2 Summary of measured inductors.

Type	No. of turns	Line width /spacing (μm)	Area (μm^2)	L (nH)	Q_{max}(f(GHz))	SRF(GHz)
Meandered	4	60/40	760×660	2.6	20(2)	> 6
Meandered	8	50/50	1100×1450	5.1	16(1.7)	~ 5
Spiral	1.5	40/20	460×460	2.5	45(4.5)	> 6
Spiral	2.75	40/20	660×680	6.3	20(1.9)	4.25
Spiral	4.5	20/20	560×580	12	14(1.8)	3.45

4.5 INTERMODULATION DISTORTION MEASUREMENT AND DYNAMIC RANGE EXTENSION

To this point we have considered BST IDCs, CPWs, and inductors in linear operation. If devices are operated at a high power level, problems of nonlinearity are introduced and must be controlled. Linearity is a critical parameter to prevent nonlinear signal distortion, which is an unwanted phenomenon for linear operation. In this section, we discuss how to measure nonlinear signal distortion and introduce a novel approach to improve the linearity of BST varactors.

Among the various ways to characterize distortion properties, two-tone intermodulation is one of the most common. When two signals are applied to a nonlinear device at frequencies of f_1 and f_2, the nonlinear characteristics of the device generates intermodulation (IM) products. Of particular interest are the third-order IM (IM3) products at $2f_1$-f_2 and $2f_2$-f_1 because these products are very close to the carrier frequency

and are difficult to filter out by a band-pass filter. The relation of various spectral components is shown in Figure 4.21.

A nonlinear output voltage can be expressed as a Taylor series so that [68]

$$V_{out}(t) = G_1 V_{in}(t) + G_2 V_{in}^2(t) + G_3 V_{in}^3(t) + \cdots + G_n V_{in}^n(t), \tag{4.8}$$

where $G_{1\ldots n}$ are the amplitude constants. If we assume that two tones have equal amplitude of a and frequency f_1 and f_2, respectively, that is,

$$V_{in}(t) = a\cos(2\pi f_1 t) + a\cos(2\pi f_2 t), \tag{4.9}$$

then, third-order components can be obtained by

$$\frac{3\times G_3 \times a^3}{4}\left(\cos(2\pi(2f_1 - f_2)t) + \cos(2\pi(2f_2 - f_1)t)\right). \tag{4.10}$$

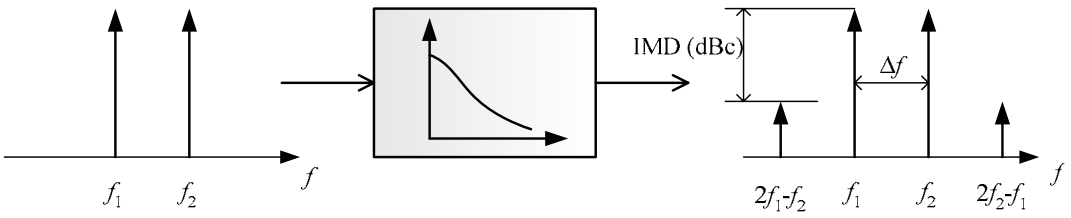

Figure 4.21 Intermodulation in a nonlinear device.

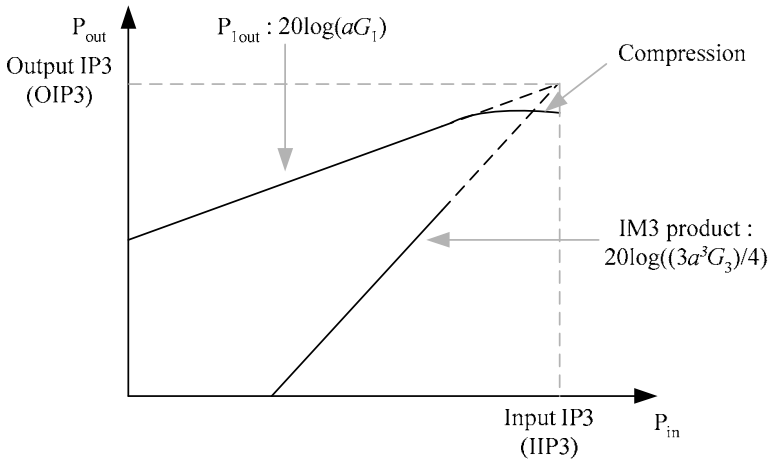

Figure 4.22 Relation between fundamental and third-order products.

The amplitude of third-order terms depends on the input signal level, and it increases by 3 dB if the input signal level is increased by 1 dB. Therefore, if one plots fundamental output power P_{1out} and IM3 products as a function of P_{in} (input power), then the slopes are 1:1 and 3:1, respectively, as illustrated in Figure 4.22. Here, the third-order intercept point (IP3) is defined as the point at which third-order products are equal to the fundamental signal. The input IP3 (IIP3), which is the vertical of this point, can be expressed by the output IP3 (OIP3), which is the horizontal of this point, and an insertion loss of the device. The relation between IIP3 and OIP3 is expressed by

$$\text{IIP3} = \text{OIP3} - \text{IL} = (P_{1\text{out}} + \frac{\text{IMD}_{\text{dBc}}}{2}) - \text{IL} \ . \tag{4.11}$$

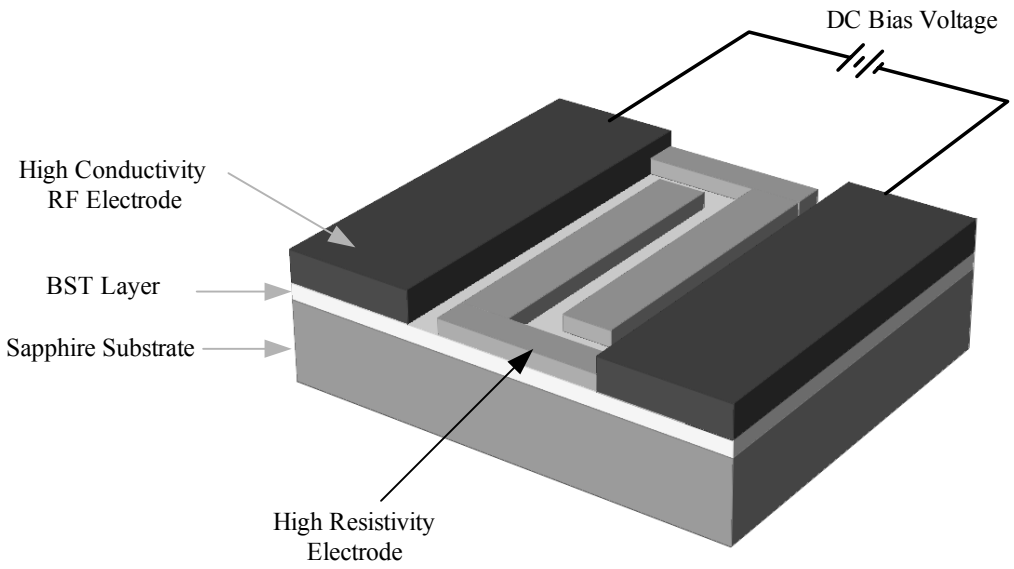

Figure 4.23 Reduced IMD capacitor

In order to improve the linearity of a BST varactor, Yoon *et al*. [63] proposed a reduced IMD capacitor. In conventional varactors, nonlinearity is directly proportional to the tunability of varactors, and thus a low control voltage and high tunability can degrade

linearity. However, a reduced IMD capacitor has a separate DC bias structure within the conventional RF gap capacitor so that the RF signal can be effectively isolated by the bias structure. The result is no degradation of IMD performance. The schematic of the reduced IMD capacitor is shown in Figure 4.23. This capacitor is composed of a conventional RF gap capacitor with a 12-14 μm gap and a separate bias structure, which has very narrowly spaced high resistance (2-3 $\times$ 10^4 Ω/sq.) oxide conductor electrodes 1-2 μm apart. This high resistivity of the bias structure decouples the DC bias from the RF signal, and the wide gap of the capacitor enables it to keep good IMD performance.

Figure 4.24 illustrates a two-tone cancellation setup. The equal-power input signals generated from two signal generators are separated by 50 kHz (f_1 = 1.9 GHz, f_2 = 1.90005 GHz), and these signals are amplified and merged by a high-power combiner. The combined signals are divided into two identical signals with a 3-dB loss to be applied to the device under test (DUT) and the delay line, respectively. The DUT output signal and the delayed signal from the delay line are combined and connected to a spectrum analyzer for the IM measurement. Ideally, two fundamental signals are cancelled because the DUT output signal and the signal from the delay line are out of phase. This cancellation setup can keep the noise floor of the RF signal at a low level, making it possible to measure IM3 products over a wide range.

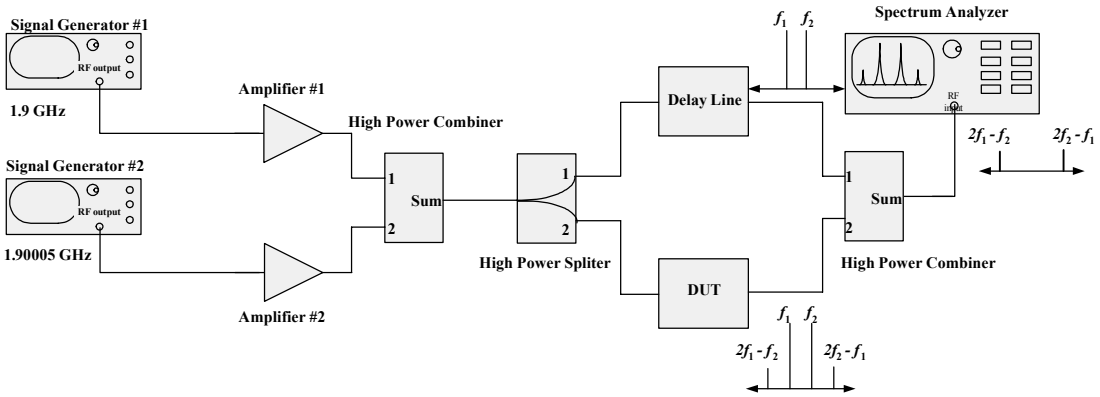

Figure 4.24 Two-tone cancellation setup.

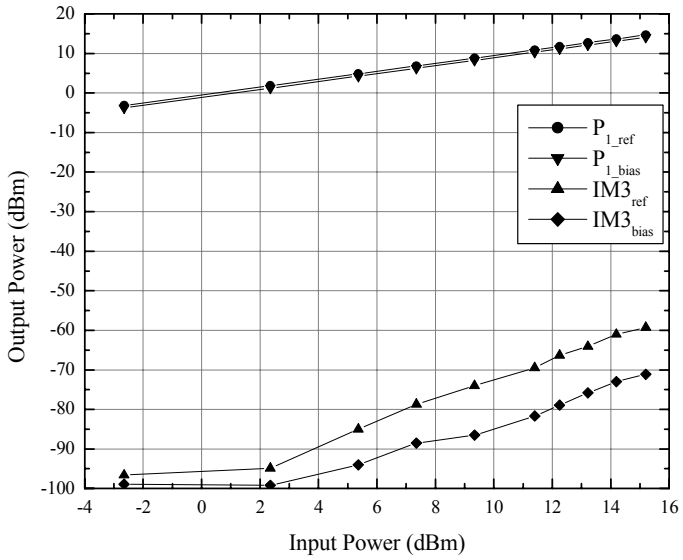

Figure 4.25 Fundamental output powers and third-order IM (IM3) products as a function of input power.

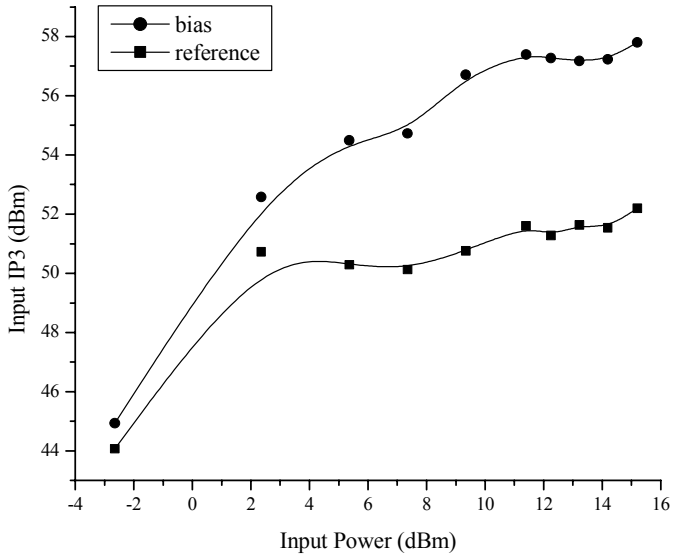

Figure 4.26 Input IP3 as a function of input power.

Figure 4.25 shows the fundamental output power and IM3 of the reference and the reduced IMD capacitor as a function of input power. Here, the tunability and capacitance of the reference capacitor are the same as those of the reduced IMD capacitor. At the low input power ranges (below 2 dBm), the IM3 of both capacitors are close to each other, and the difference of the IM3 of two capacitors is increasing with the increased input power. Beyond an IM3 of 10 dBm, the difference of IM3 is about 12 dB. The IIP3 against the input power is shown in Figure 4.26. Approximately 6 dB IIP3 improvement is obtained beyond an input power of 10 dBm. Compared to the reference structure, we can achieve the same tunability and 6 dB IIP3 improvement by using the reduced IMD capacitor.

4.6 CONCLUSIONS

In this chapter, the characterization of BST thin films using various CPWs and IDCs and the electrical properties of passive components based on BST coated sapphire substrates were explored. It was seen that high tunability (more than 3) could be obtained with a relatively high Q-factor using BST IDCs with an applied bias voltage of around 140 V. By shrinking the spacing between fingers, bias voltage could be reduced at the expense of linearity. In order to overcome this typical tradeoff between nonlinearity and bias voltage, a reduced IMD capacitor was introduced along with a brief description of IMD measurement. Additionally, the temperature characteristics of BST varactors were analyzed, and it was found that the optimum composition of BST thin films with respect to the minimum variation over temperature occurred with a Ba/Sr ratio of 1.2 and (Ba+Sr)/Ti ratio of 0.8. Finally, two different types of inductors were implemented on the substrates, resulting in relatively high Q-factors in association with the desired values of the inductors.

In the next chapter, the designs of phase shifters based on BST coated sapphire substrates will be shown. With 3 dB couplers as well as with the passive components described in this chapter, the theoretical and experimental results of several *S*-band reflection-type phase shifters will be presented.

CHAPTER V

S-BAND REFLECTION-TYPE PHASE SHIFTERS

The main topic of this research is to implement phase shifters on barium strontium titanate (BST) coated sapphire substrates operating at *S*-band. Although BST varactors, reduced IMD capacitors and CPWs, as described in the previous chapter along with an investigation of their material properties, could find utility in other applications, phase shifters are currently drawing the most interest for wireless applications such as phased-array antennas. As a consequence, in Chapter 5 and Chapter 6, several phase-shifter designs and the corresponding experimental validations will be discussed. Various CPWs , IDCs, and inductors have been characterized in the previous chapter with respect to a geometry, bias voltage, and temperature. These elements will be employed to implement BST phase shifters. In this chapter, reflection-type phase shifters, which represent early versions of BST phase shifters, are introduced. It should be emphasized here that these early versions show a potential to implement integrated BST phase shifters operating at *S*-band, but have not yet been optimized at 2.4 GHz.

A reflection-type phase shifter was first introduced by Hardin *et al*. [27] and has been one of the most common topologies for phase-shifter applications. A reflection-type phase shifter makes use of a 3-dB coupler with two ports that terminate in either phase-controllable reflective terminations for an analog operation or in switches for a digital operation. We will focus on an analog operation by utilizing BST properties, and the phase shifter described in this chapter is the first development of integrated reflection-

type phase shifters using BST thin films.

A schematic of an analog reflection-type phase shifter is shown in Figure 5.1. It consists of a 3-dB coupler, a bias network, and two identical phase-controllable LC reflective terminations that are connected to the coupled and direct ports of the coupler. The coupler divides the input signal equally between two output ports with a phase difference of 90°. Reflected signals from LC reflective terminations sum at the isolated port of the coupler. If lossless LC terminations are connected to an ideal 3-dB coupler, all the power at the input port will emerge from the isolated port. This type of phase shifter has a good return loss over a large range of phase shift.

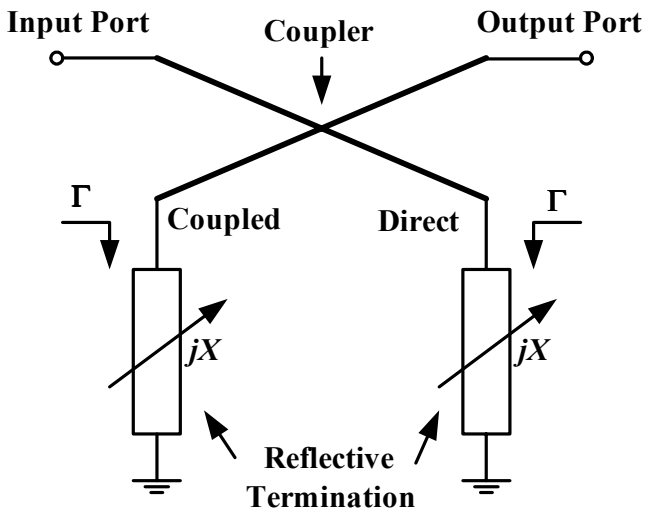

Figure 5.1 Schematic of a reflection-type phase shifter

5.1 3-dB Couplers on BST Coated Substrates

A variety of 3-dB couplers are available for many applications, and among the several design options, a branch-line coupler and a Lange coupler are discussed in this section because these are the most appropriate structure for a CPW configuration with easy fabrication and good performance. Compared with a microstrip coupler, a CPW coupler

has the advantage of easy connection to shunt devices, less radiation loss, and no need for via holes. Also, a CPW structure confines electric fields near the substrate surface, keeping a large percentage of the electric field in the BST. Therefore, it maintains a highly effective dielectric constant, resulting in shrinking the size of the distributed elements. In other words, the size reduction results from relatively short quarter-wave-length transmission lines of the couplers because of the high dielectric constant of BST thin films.

5.1.1 CPW Branch-Line Coupler

A CPW branch-line coupler shown in Figure 5.2 is one of the simplest structures for realizing a 3-dB coupler. Two main quarter-wave-length transmission lines spaced one quarter wavelength apart divide the input signal into two output signals, which are equal in magnitude but out of phase by 90°. For a 3-dB coupler, the characteristic impedances of the main (Z_A) and the shunt branches (Z_B) should be $Z_0/\sqrt{2}$ and Z_0, respectively. Z_0 is the characteristic impedance of the input and output ports.

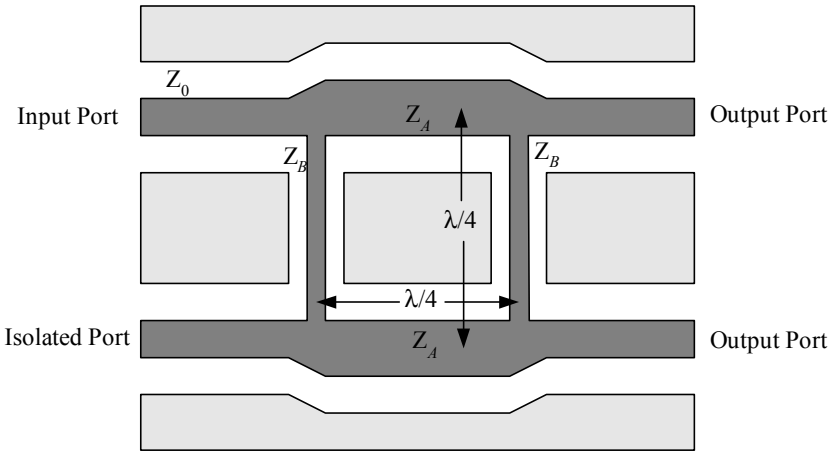

Figure 5.2 Schematic of a CPW branch-line coupler.

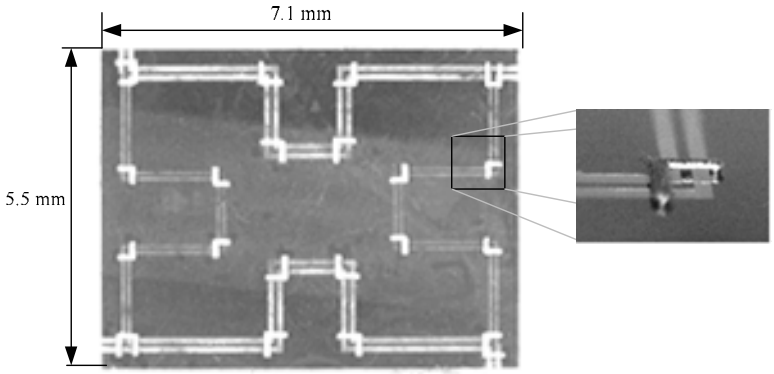

Figure 5.3 Photomicrograph of the fabricated CPW branch-line coupler.

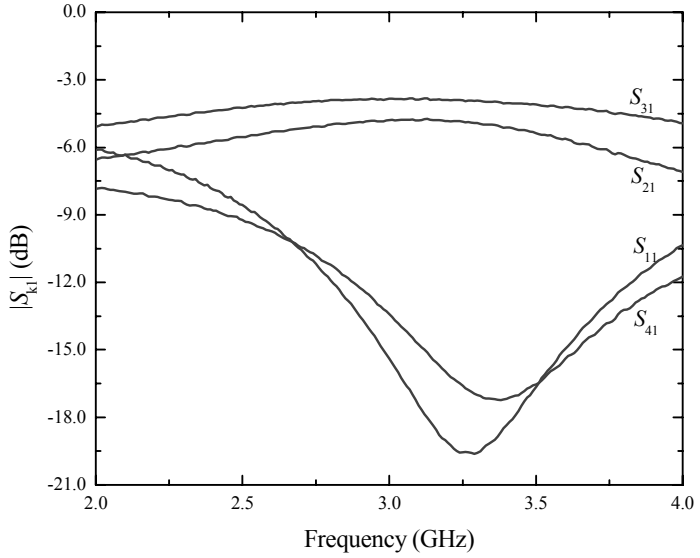

Figure 5.4 Experimental result of the CPW branch-line phase shifter.

Photomicrographs of the fabricated CPW branch-line coupler and air bridge for interconnections between ground planes are shown in Figure 5.3. To further reduce the overall size of the coupler, meandered lines are used instead of conventional straight lines, so that the size is less than 7.1 mm × 5.5 mm. Figure 5.4 shows the measured results of

the fabricated CPW branch-line coupler. The coupler provides a power split of 4.3 dB ± 0.5 dB at 3.1 GHz and the isolation and the return loss of the coupler are higher than 17 dB and 15 dB, respectively.

5.1.2 CPW Lange Couplers

Another configuration to realize a 3-dB coupler is the Lange coupler, which is one of the most practical for implementation [69]. With reference to Figure 5.5 the Lange coupler has generally four coupled lines that are interconnected to provide a tight coupling (3 dB) over a wide bandwidth. The Lange coupler has the advantages of small size and large line spacing compared to a coupled-line coupler and a large bandwidth compared to a branch-line coupler.

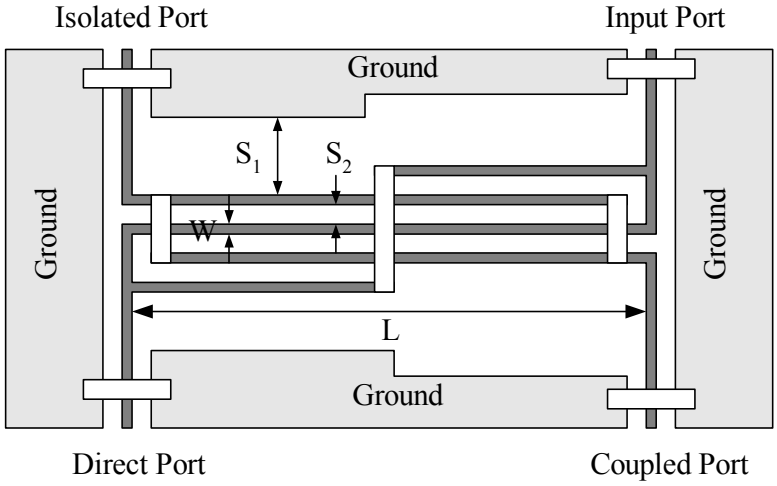

Figure 5.5 Schematic of a CPW Lange coupler.

The design of the Lange coupler starts from the even- and odd-mode characteristic impedances of two coupled lines. The desired characteristic impedance and coupling coefficient for the even- and odd-mode impedances are from [70],

$$Z_{0e} = \frac{4C - 3 + \sqrt{9 - 8C^2}}{2C\sqrt{(1-C)/(1+C)}} Z_0, \tag{5.1}$$

$$Z_{0o} = \frac{4C + 3 - \sqrt{9 - 8C^2}}{2C\sqrt{(1+C)/(1-C)}} Z_0, \tag{5.2}$$

where C is the voltage coupling coefficient, and Z_0 is the characteristic impedance. Therefore, the even- and odd-mode characteristic impedances must be 176.2 Ω and 52.6 Ω, respectively, for 50 Ω system.

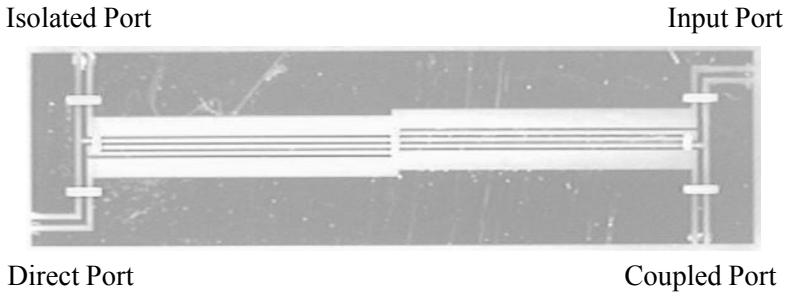

Figure 5.6 Photomicrograph of the fabricated Lange coupler.

A photomicrograph of the fabricated CPW Lange coupler based on a BST coated sapphire substrate is shown in Figure 5.6. The Lange coupler has a line width of 40 μm, spacing between lines and ground of 300 μm, spacing between all adjacent lines of 60 μm, and the length of lines of 9400 μm according to the MoM simulation using the Microwave Office™ [60]. Air bridge crossovers are also used in order to equalize the potentials of ground planes and to suppress spurious modes.

Figure 5.7 shows the simulated result of the Lange coupler. The magnitudes of signals at direct and coupled ports are 3.6 dB and 3.9 dB at 2.5 GHz, respectively. The isolation and return loss are higher than 15 dB over a wide frequency range.

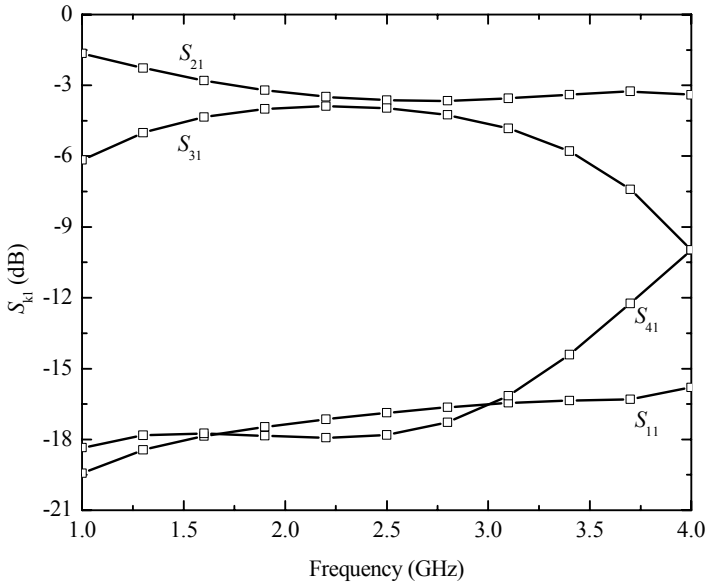

Figure 5.7 Simulated result of the Lange coupler. (line width = 40 μm, spacing = 60 μm, and length = 9400 μm)

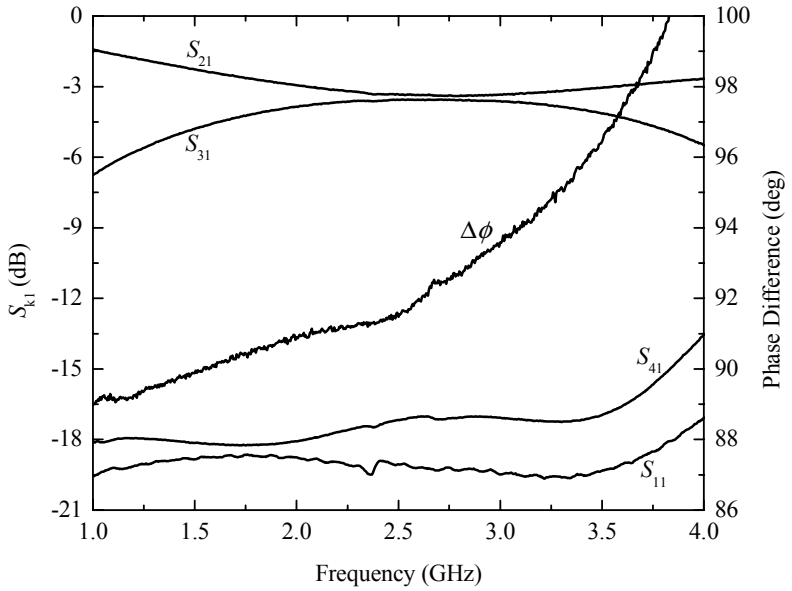

Figure 5.8 Measured result of the Lange coupler. (line width = 40 μm, spacing = 60 μm, and length = 9400 μm)

The measured result of the Lange coupler is shown in Figure 5.8. The coupler has a power split of 3.5 dB ± 0.5 dB in the range of 2 GHz - 3.4 GHz. The isolation is higher than 18 dB, and the return loss is higher than 17 dB in the same frequency range. This result shows pretty good agreement with the MoM simulated result in Figure 5.7.

Another measured result of the Lange coupler is shown in Figure 5.9. In this case, a spacing of 50 μm was used to increase an output power at the coupled port. Magnitudes of signals at direct and coupled ports are 3.9 and 3.3 dB at 2.5 GHz, respectively. The coupler has a power split of 3.5 dB ± 0.5 dB in the range of 1.6 GHz - 3.2 GHz. Also, the isolation is higher than 15 dB, and the return loss is higher than 16 dB in the same frequency range. The differential phase between the direct and coupled ports is 87° ± 1°.

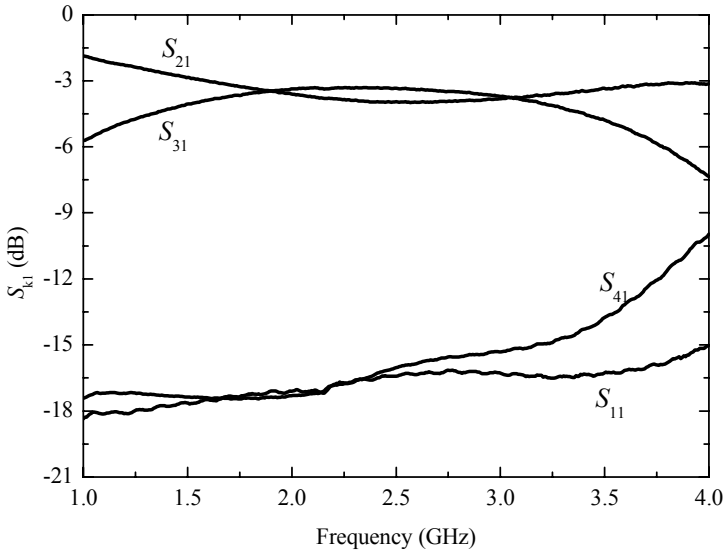

Figure 5.9 Measured result of the Lange coupler. (line width = 40 μm, spacing = 50 μm, and length = 9700 μm)

In addition to the straight Lange coupler design, a folded-type Lange coupler was designed to reduce the size of the phase shifter and maintain a smaller aspect ratio for easier packaging. The folded-type Lange coupler has a power split of 3.5 dB ± 0.5 dB, with an isolation and a return loss of higher than 16 dB in the range of 2.15 GHz - 3.4 GHz, as shown in Figure 5.10. Therefore, the CPW Lange couplers on BST thin films show a good power splitting performance with high isolation and return loss over a wide frequency range.

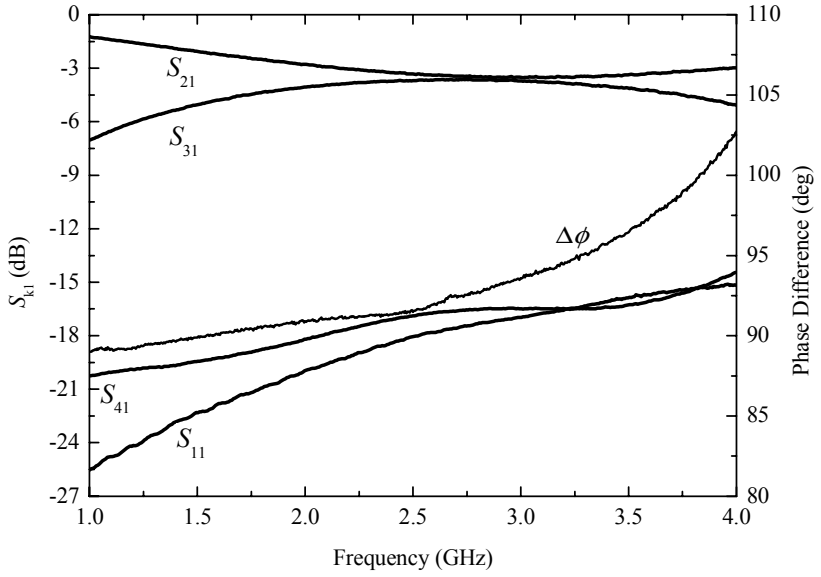

Figure 5.10 Measured result of the folded-type Lange coupler.

5.2 REFLECTIVE TERMINATIONS

A reflective termination is the main control part of a reflection-type phase shifter. There are two different types of terminations: single-series resonated termination and double-series resonated termination in parallel connection. A single-series resonated termination consists of a series combination of two capacitors and an inductor in order to increase the

phase-shift range by resonating the capacitive reactance with the inductive reactance, as shown in Figure 5.11. These two capacitors are placed in series with a bias voltage applied to the node between them through the bias network. The differential phase with respect to the phase at 0 V is controlled by the variation of capacitance using an external bias voltage.

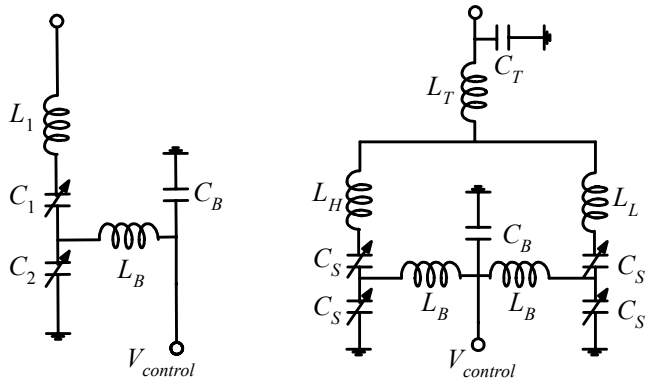

(a) (b)

Figure 5.11 Reflective terminations with a bias network. (a) Single-series resonated termination. (b) Double-series resonated termination in parallel connection with a transformation network.

If we assume that the values of L_B and C_B are high enough to be of consequence, and all parasitics are zero, the voltage reflection coefficient and the phase of a single-series resonated termination are expressed by

$$\Gamma = \frac{jX_T - Z_0}{jX_T + Z_0}, \tag{5.3}$$

$$\angle\phi_T = \tan^{-1}\left(\frac{2Z_0X_T}{{X_T}^2 - {Z_0}^2}\right) = \pi - 2\tan^{-1}\left(\frac{X_T}{Z_0}\right), \tag{5.4}$$

where Z_0 and X_T are the characteristic impedance and total reactance of the termination, respectively. The phase variation of the termination is given by

$$\Delta\phi_T = \left[\left(\pi - 2\tan^{-1}\left(\frac{X_{Tmin}}{Z_0}\right) - \left(\pi - 2\tan^{-1}\left(\frac{X_{Tmax}}{Z_0}\right)\right)\right)\right], \\ = 2\left[\tan^{-1}\left(\frac{X_{Tmax}}{Z_0}\right) - \tan^{-1}\left(\frac{X_{Tmin}}{Z_0}\right)\right] \tag{5.5}$$

$$X_{Tmax} = \left(\omega L_1 - \frac{(C_{1max} + C_{2max})}{\omega C_{1max} C_{2max}}\right) = \left(\omega L_1 - \frac{(C_{1min} + C_{2min})}{\omega r C_{1min} C_{2min}}\right), \tag{5.6}$$

$$X_{Tmin} = \left(\omega L_1 - \frac{(C_{1min} + C_{2min})}{\omega C_{1min} C_{2min}}\right), \tag{5.7}$$

where X_{Tmax} and X_{Tmin} are the maximum and minimum reactance, respectively. In order to obtain the maximum phase shift with a limited tunability of the capacitor, the maximum reactance should be set equal to the minimum reactance with opposite sign (X_{Tmax}= -X_{Tmin}). Therefore, the corresponding optimal inductance L_1 and the maximum phase shift for a lossless single-series resonated termination can be expressed as

$$L_1 = \frac{C_{1min} + C_{2min}}{2\omega^2 C_{1min} C_{2min}}\left(1 + \frac{1}{r}\right) = \frac{1}{2\omega^2 C_{min}}\left(1 + \frac{1}{r}\right), \tag{5.8}$$

$$\Delta\phi_{Tmax} = 4\tan^{-1}\left[\frac{C_{1min} + C_{2min}}{2\omega Z_0 C_{1min} C_{2min}}\left(1 - \frac{1}{r}\right)\right] = 4\tan^{-1}\left[\frac{1}{2\omega Z_0 C_{min}}\left(1 - \frac{1}{r}\right)\right], \tag{5.9}$$

where r is the ratio of the maximum and minimum capacitance, and C is the series capacitance of C_1 and C_2.

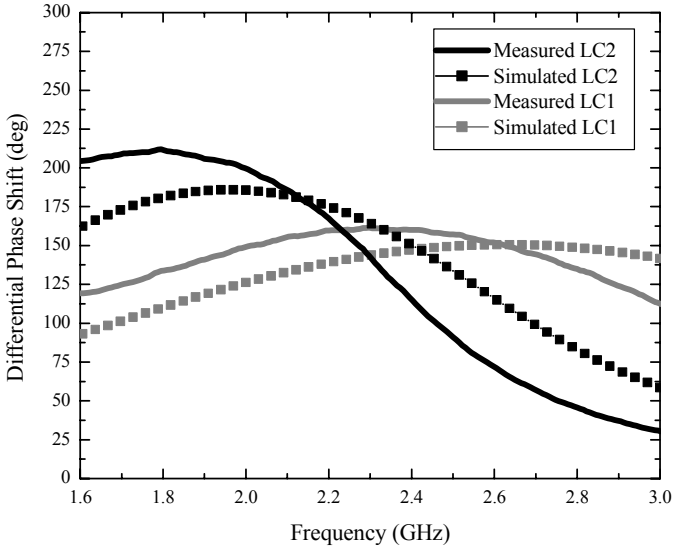

Figure 5.12 Simulated and measured differential phase-shift ranges of two different single-series resonated terminations.

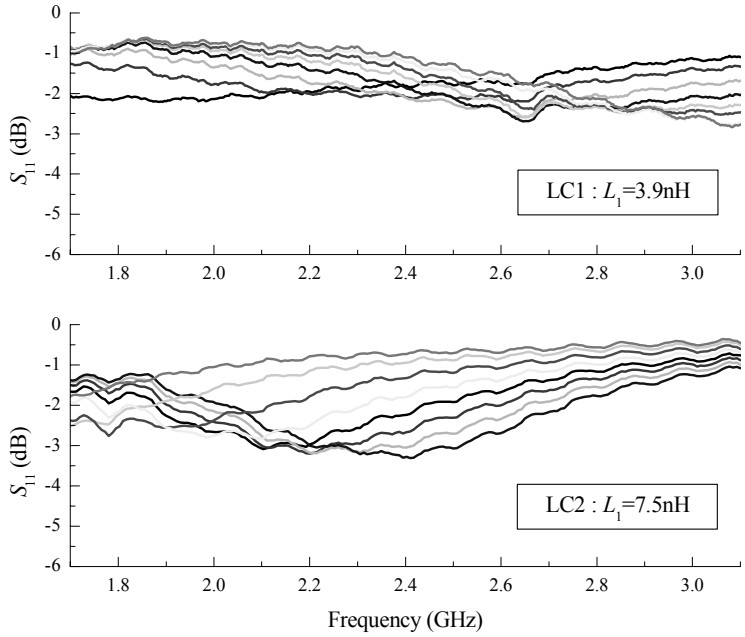

Figure 5.13 Measured return losses of two different single-series resonated terminations.

Figure 5.12 and Figure 5.13 show simulated and measured results of two different terminations. LC1 and LC2 have L_1 = 3.9 nH and 7.5 nH at 2.5 GHz, respectively, with C_{1max} = 2.4 pF, C_{2max} = 3.9 pF, and a tunability, r = 3.1. LC1 has a phase-shift range of more than 155° and loss of better than 2.2 dB in the frequency range of 2.1 GHz - 2.5 GHz, whereas LC2 has more than 200° and better than 2.8 dB between 1.6 and 2 GHz. To achieve a higher phase-shift range, a high inductance and a low capacitance are needed according to (5.8) and (5.9). However, this can cause a higher loss because of the resistive parasitics. Therefore, the single series termination is suitable for about a 180° phase-shift range with a limited tuning range ($r \leq 4$) in terms of loss per decibel.

Generally, a 360° phase-shift range is required for a full azimuthally scanning range in adaptive phased-array antennas. One way to reach a 360° phase-shift range is using two or more identical stages cascaded. However, the size of this topology for the BST phase shifter herein is too large to enjoy the benefit of the high dielectric material because of the 3-dB coupler. Another approach is that the phase variation of the reflective termination can be increased using two different series resonated terminations. One resonated termination is series resonant at the lowest bias voltage, whereas the other is at the highest voltage. Also, a transformation network is needed in order to reduce a return loss and loss variation. Figure 5.14 and Figure 5.15 illustrate the measured differential phase shift and loss of double-series resonated termination as a function of frequency. The termination has more than 360° phase shift at 2.5 GHz. The average loss of the terminations is 4.7 dB, and the maximum loss is 6.4 dB at 2.5 GHz with 160 V.

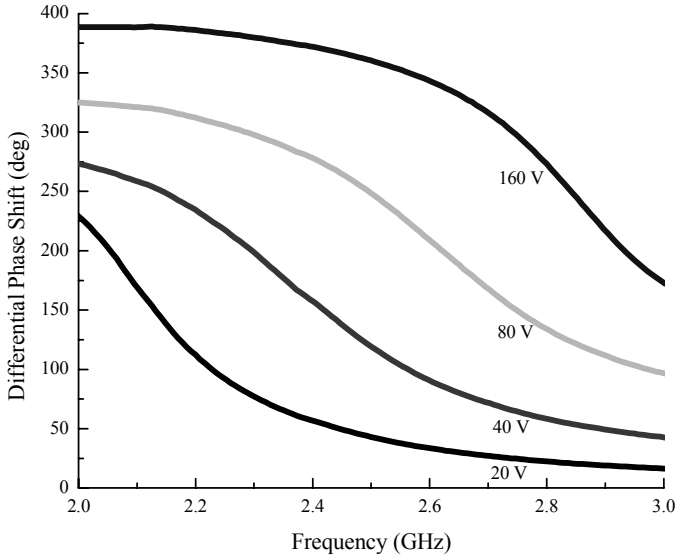

Figure 5.14 Measured differential phase shift of double-series resonated termination in parallel connection.

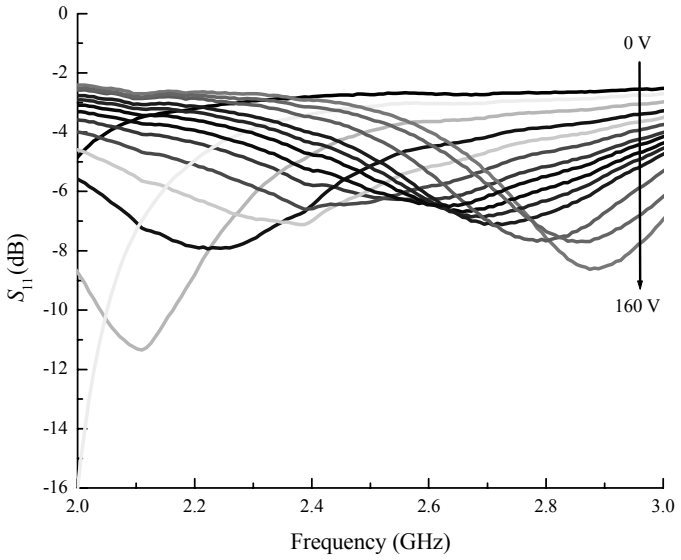

Figure 5.15 Measured return loss of double-series resonated termination in parallel connection.

5.3 REFLECTION-TYPE PHASE SHIFTERS

As described previously, a reflection-type phase shifter is composed of a 3 dB coupler and single- or double-series resonated terminations, depending on the desired phase-shift range. First, the phase shifter based on the CPW branch-line coupler and single-series resonated terminations is introduced to show the potential to achieve the BST phase shifter. Second, the CPW Lange coupler is employed to provide better performance and reduce overall size. Both the conventional straight design and folded-type design are used. Finally, it is desirable to keep the phase-shifter size as small as possible, and thus the modified folded-type phase shifter is designed in order to further reduce the size and maintain a smaller aspect ratio for easier packaging, resulting in overall size of the phase shifter of only 4 mm × 4 mm. We will first show the experimental results of the phase shifter using the branch-line coupler, and then show the results using the Lange couplers. The nonlinear characteristics of the phase shifters will be found in the last section.

5.3.1 Small-Signal Characteristics

The fabricated reflection-type phase shifter using the CPW branch-line coupler is shown in Figure 5.16. The phase shifter consists of the CPW branch-line coupler and two identical single-series resonated terminations along with a bias network. The total size of the phase shifter is less than 7.1 mm × 7.1 mm. Figure 5.17 shows the measured insertion loss under five different bias conditions in the range of 2 GHz - 4 GHz. The most equal insertion loss for all bias levels occurs at 2.95 GHz and is between 4.0 and 4.2 dB over the bias range. The insertion loss is better than 5 dB between 2.83 GHz and 3.03 GHz, with a variation of no more than 2 dB. The return loss is higher than 12.5 dB at 2.95 GHz, and higher than 10 dB over a range of 200 MHz, as shown in Figure 5.18. Figure 5.19

shows the relative phase shift at 2.85, 2.95 and 3.05 GHz with respect to the phase at 0V. A more than 110° phase shift is achieved at 2.85 GHz with a bias voltage of 175 V. A phase shift of more than 90° is achieved over ± 100 MHz at about 2.95 GHz.

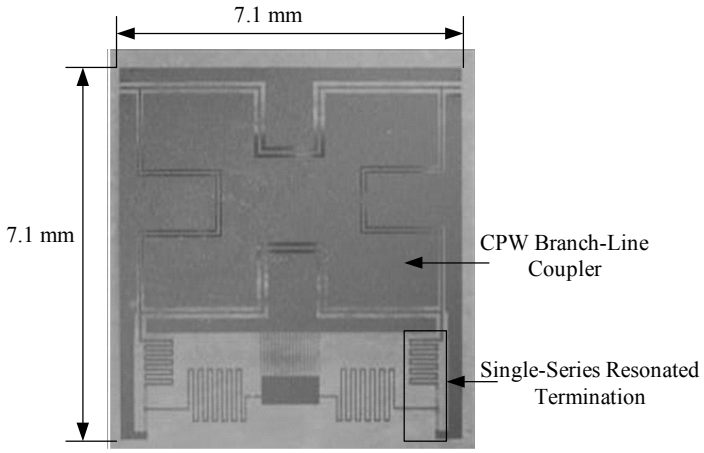

Figure 5.16 Photomicrograph of the reflection-type phase shifter using the CPW branch-line coupler.

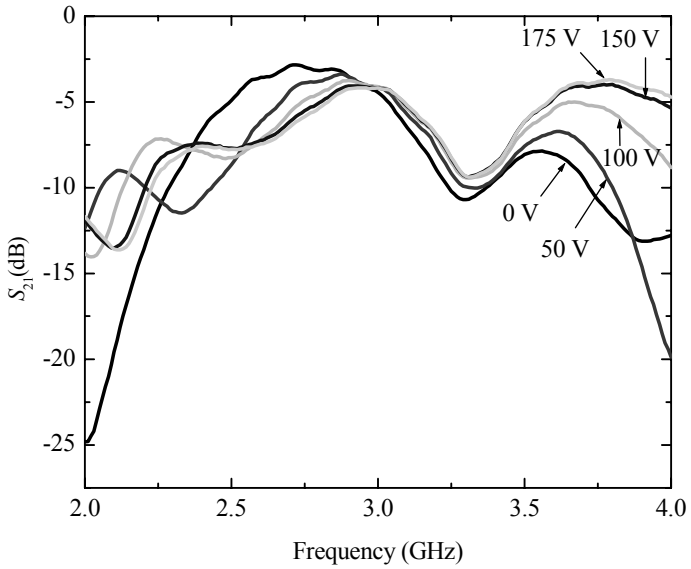

Figure 5.17 Insertion loss of the phase shifter under five different bias conditions.

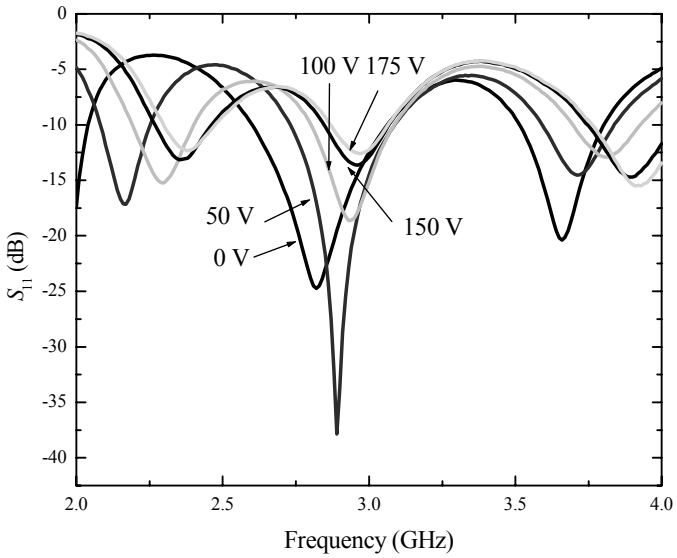

Figure 5.18 Return loss of the phase shifter under five different bias conditions.

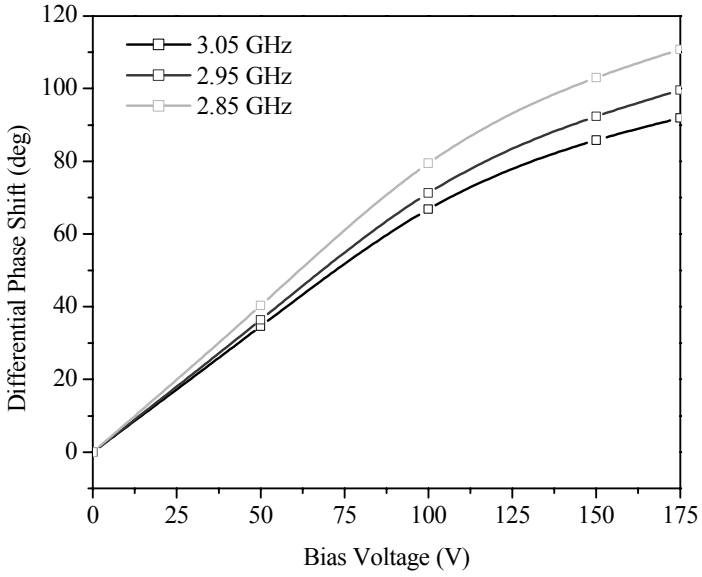

Figure 5.19 Differential phase shift with respect to the phase at 0 V for three different frequencies.

The fabricated reflection-type phase shifters using the CPW Lange couplers are shown in Figure 5.20. Two different phase-shifter versions are implemented. The first one uses the conventional straight Lange coupler. The second one uses the folded-type Lange coupler. Both phase shifters have two identical single-series resonated terminations connected to the two output ports of the coupler.

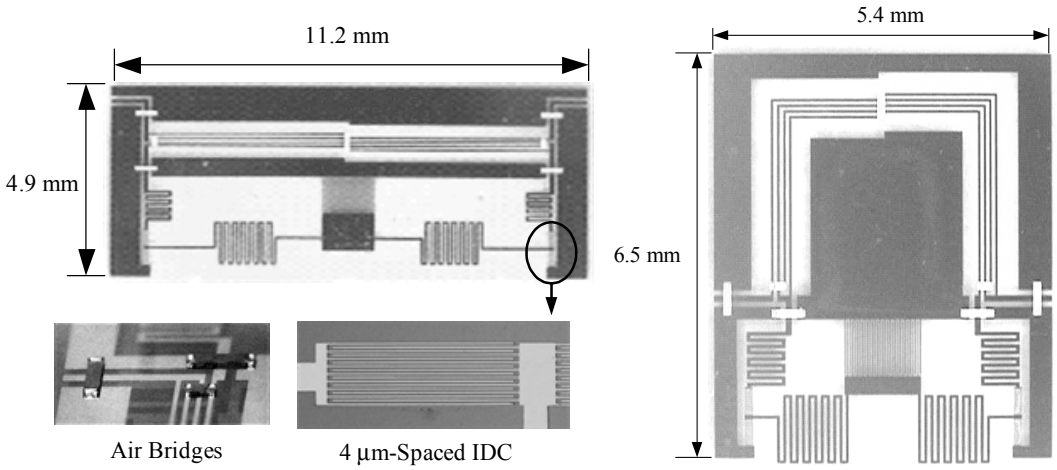

Figure 5.20 Photomicrograph of the reflection-type phase shifters. (a) Straight design. (b) Folded-type design.

The insertion loss and the return loss of the phase shifter using the straight Lange coupler are shown in Figure 5.21. Both phase-shifter versions are designed with a lower inductance (L_1 = 2.2 nH) than optimal values from (5.9) using a given capacitance (C_{1max} = C_{2max} = 4.2 pF) in order to reduce the insertion loss of the phase shifter and the loss variation. The insertion loss is less than 2 dB over most of the frequency range between 1.9 GHz and 3.7 GHz over all bias states. A narrowband resonance around 2.35 GHz increases the insertion loss to a maximum of 2.3 dB. The return loss is higher than 14 dB

in the same frequency range. Figure 5.22 shows the differential phase shift with respect to the phase at 0 V as a function of frequency for eight different bias levels. A more than 90° phase shift is achieved between 1.5 and 2.5 GHz with a bias voltage of 160 V. Therefore, a continuously variable phase-shift range of more than 90° with an insertion loss of better than 2 dB (not including losses from the resonance problem) and a return loss of 14 dB was obtained in the frequency range of 1.9 GHz - 2.5 GHz with all bias states.

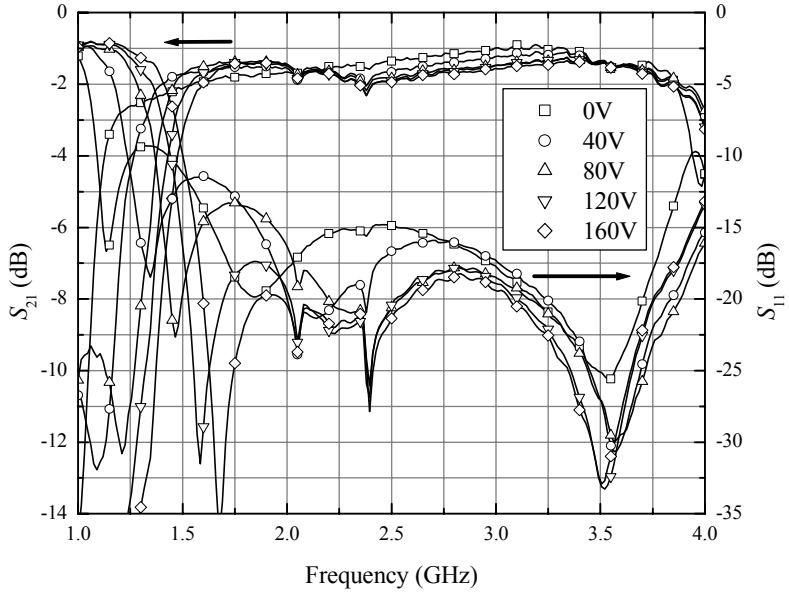

Figure 5.21 Insertion loss and return loss of the phase shifter using the straight-design Lange coupler for 0, 40, 80, 120, and 160 V in the range of 1 GHz - 4 GHz.

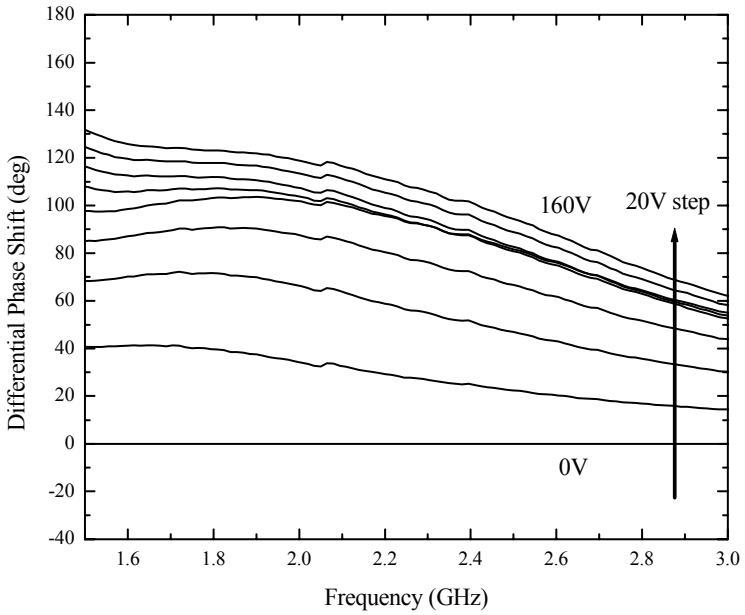

Figure 5.22 Differential phase shift of the phase shifter using the straight-design Lange coupler with respect to the phase at 0 V for a 20-V step.

Figure 5.23 and Figure 5.24 show the measured results of the phase shifter using the folded-type Lange coupler. The phase shifter has a phase-shift range of 133° with an insertion loss of 2.2 dB, loss variation of ± 0.1 dB, and return loss of higher than 19 dB at 2.5 GHz. Also, a phase-shift range of more than 130° was obtained with a bias voltage of 160 V in the frequency of 2.2-2.6 GHz. The overall performance and operating frequency range of this phase shifter are somewhat at variance with those of the phase shifter using the straight Lange coupler because of the slightly different thickness and/or composition of BST thin films.

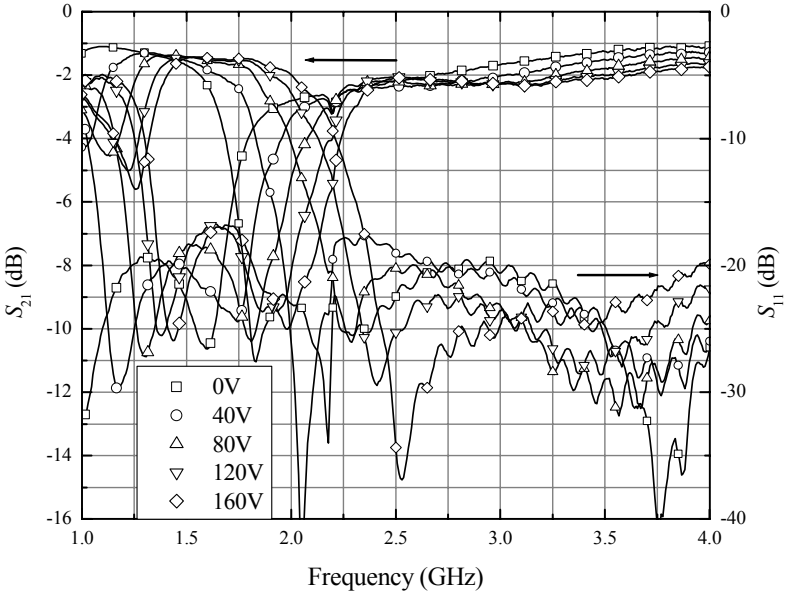

Figure 5.23 Insertion loss and return loss of the phase shifter using the folded-type design Lange coupler for 0, 40, 80, 120, and 160 V in the range of 1 GHz - 4 GHz.

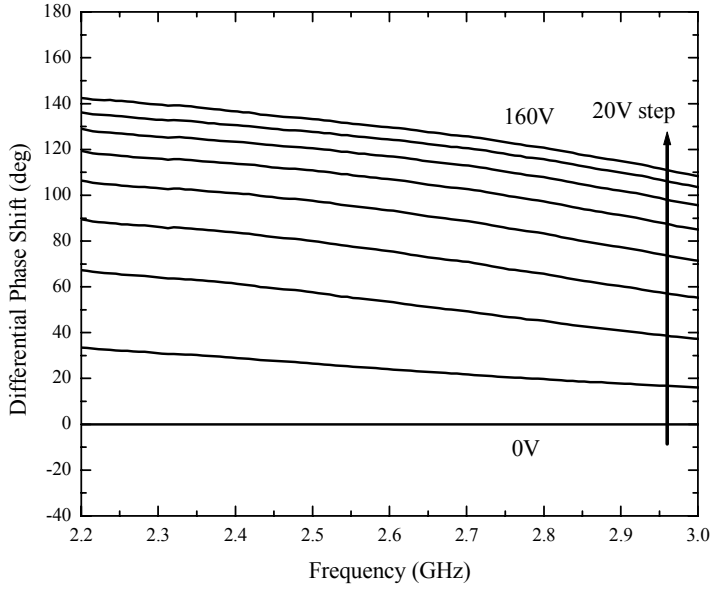

Figure 5.24 Differential phase shift of the phase shifter using the folded-type design Lange coupler with respect to the phase at 0 V for a 20-V step.

Although Figure 5.21 - Figure 5.24 sufficiently demonstrate the performance of the phase shifters, the loss figure-of-merit (FOM) of phase shifters can often be better illustration. The loss FOM can be expressed as

$$F = \frac{|\Delta\phi|(\text{deg})}{\alpha_{max}(dB)}, \tag{5.10}$$

where $\Delta\phi$ and α_{max} are the differential phase shift and maximum insertion loss, respectively. Maximum 72°/dB at 2 GHz and 40°/dB in the range of 1.5 GHz - 3 GHz were achieved with a bias voltage of 160 V using the straight Lange coupler, as shown in Figure 5.24. Also, the phase shifter using the folded-type Lange coupler has a maximum 57°/dB at 2.5 GHz. These results compare favorably, in terms of a loss and differential phase shift, to other reported BST phase shifters and to recently reported GaAs MMIC phase shifters

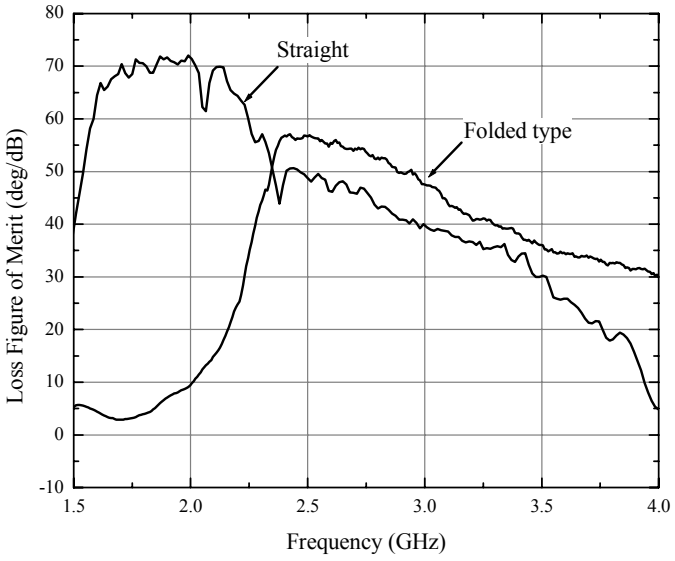

Figure 5.25 Loss FOM of two different types of phase shifters.

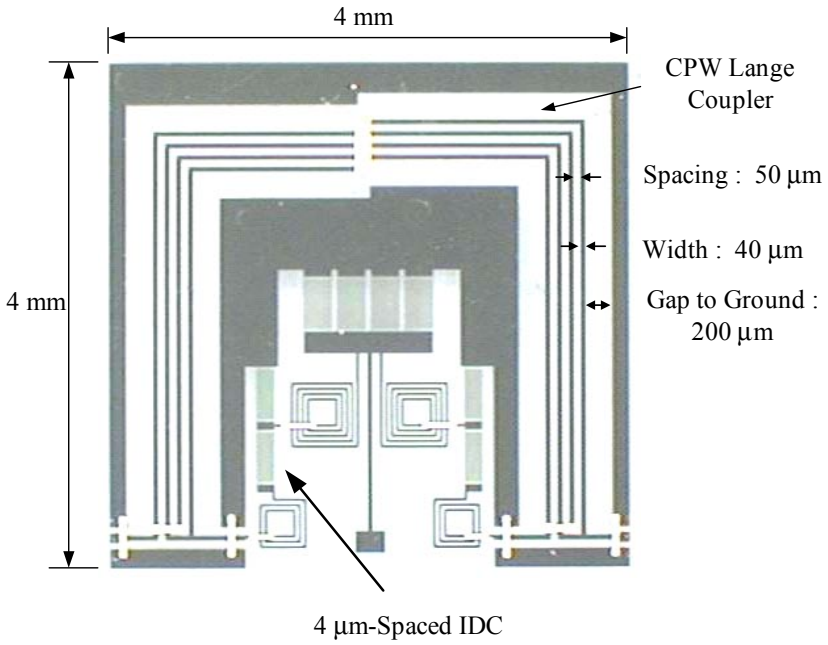

Figure 5.26 Photomicrograph of the modified reflection-type phase shifter.

The modified reflection-type phase shifter using the folded-type Lange coupler is fabricated to further reduce the size of the phase shifter. Two identical single-series resonated terminations and a bias network are located inside the Lange coupler so that the total size of the phase shifter is only 4 mm × 4 mm as shown in Figure 5.26. The measured results of the modified phase shifter are shown in Figure 5.27. The differential phase shift with respect to the phase at 0 V is up to 178°, with an average insertion loss of 2.9 dB and loss variation of ± 0.6 dB at 2.7 GHz. Also, the phase difference between 2.7 and 2.8 GHz is only 1° with a maximum insertion loss of 3.5 dB.

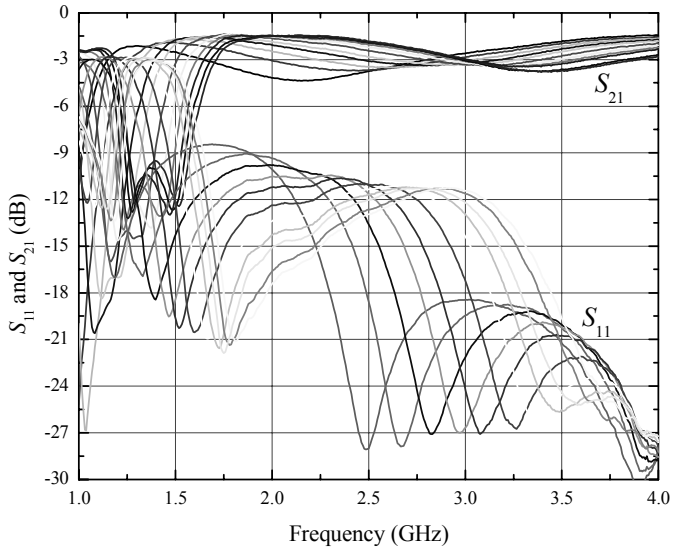

(a)

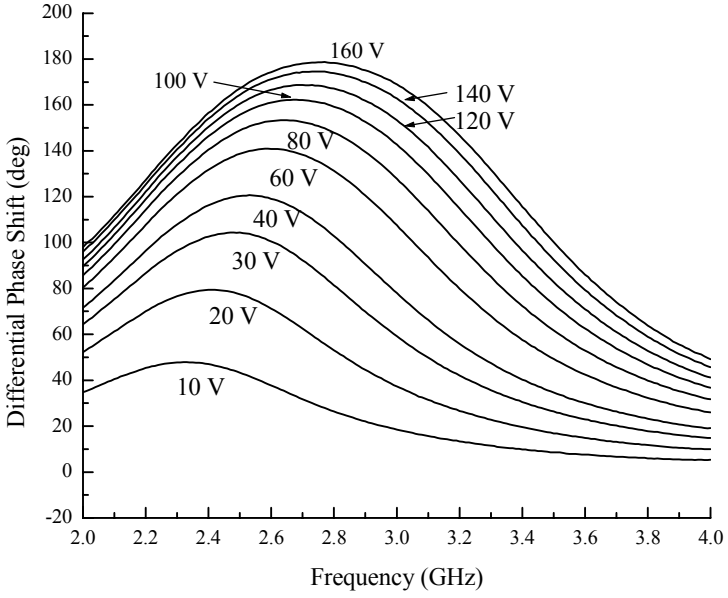

(b)

Figure 5.27 Measured result of the modified reflection-type phase shifter. (a) Insertion loss and return loss. (b) Differential phase shift with respect to the phase at 0 V.

5.3.2 Nonlinear Characteristics

Large signal characteristics of the phase shifter were investigated by two-tone measurement, as shown in Figure 5.28. The equal-power RF signals separated by 500 kHz (f_1 = 2 GHz and f_2 = 2.0005 GHz) are amplified and combined by amplifiers and an in-phase power combiner. A combined output is passed through a low pass filter in order to reduce the second, third and higher-order harmonics, and then a signal is applied to the phase shifter. This setup is the early version of the two-tone measurement setup and is relatively simple compared with the cancellation setup described in the previous chapter. This simplicity comes at the expense of dynamic range.

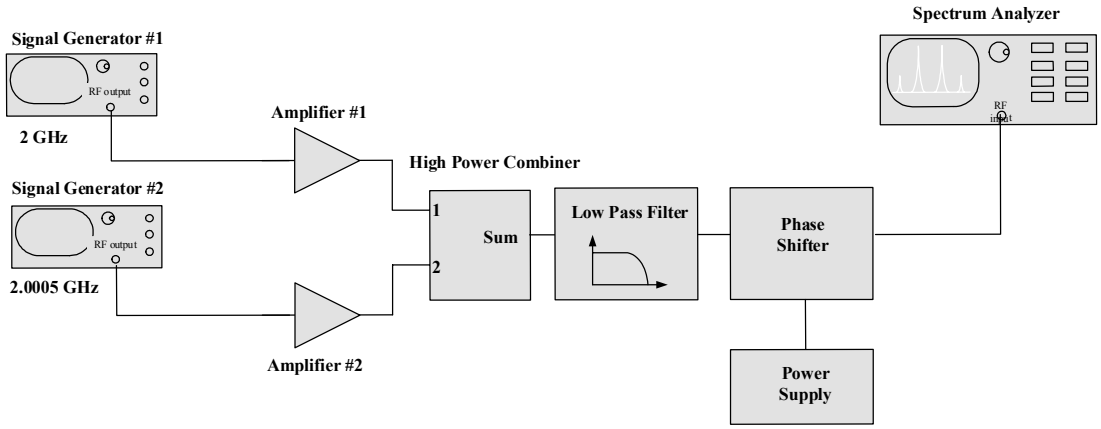

Figure 5.28 Two-tone test setup.

The fundamental and third-order output powers against the input power are measured for different bias voltages in Figure 5.29(a). As bias voltage increases, third-order output power decreases. Figure 5.29(b) shows the IIP3 of the phase shifter with different bias voltages. The phase shifter has a worst case IIP3 of 32 dBm with 0V and improves to 41.9 dBm at 60 V using input power range of 2.5 dBm - 15 dBm. The author believes this to be the best reported IIP3 to date for any BST phase shifter in this frequency range.

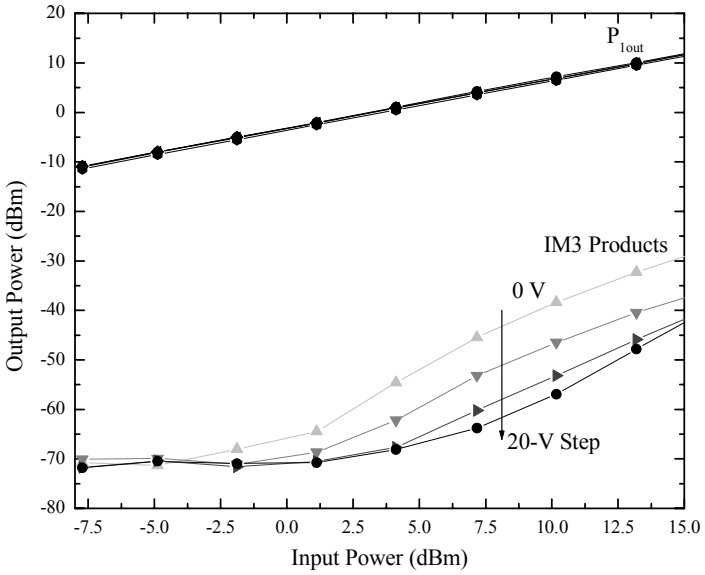

(a)

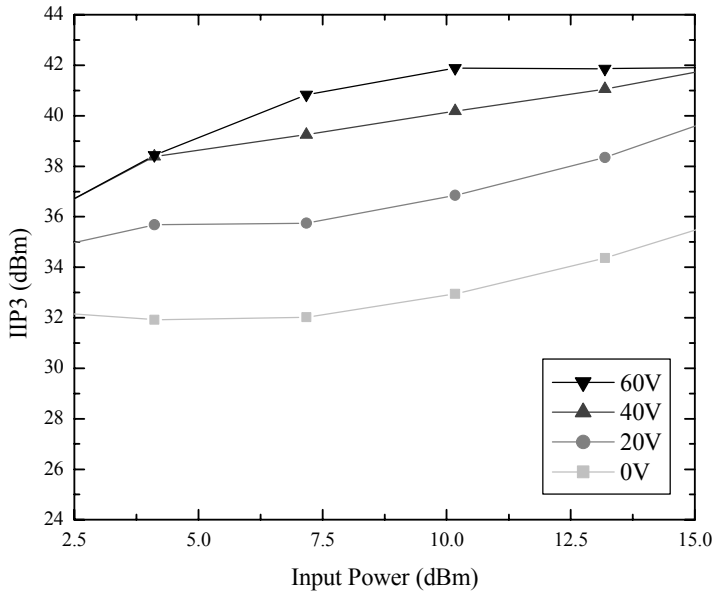

(b)

Figure 5.29 Nonlinear response of the reflection-type phase shifter with four different bias states. (a) Fundamental output powers and third-order IM products (IM3) as a function of input power. (b) Input IP3 as a function of input power.

5.4 CONCLUSIONS

In this chapter, the implementation of *S*-band reflection-type phase shifters based on BST coated sapphire substrates was reported using the material properties described in Chapter 4. The fundamental operating principles of the reflection-type phase shifter and the analytical expression of the reflective termination were discussed. The analysis included the maximum phase-shift range of the single-series resonated termination with the optimum inductance for a given capacitance and tunability. Experimental validation of the single-series resonated termination was performed along with the double-series resonated termination to obtain a phase shift of 360°. Using these terminations and 3-dB couplers, *S*-band phase shifters were successfully demonstrated, resulting in the loss FOM of 72°/dB at 2 GHz. To further reduce the overall size of the phase shifter, the modified reflection-type phase shifter was implemented as well by using a folded-type Lange coupler instead of a conventional straight Lange coupler, and thus the size of the smallest design was less than 4 mm × 4 mm. In addition to small-signal characteristics of the phase shifters, their nonlinear characteristics were investigated using two-tone IMD measurement. The worst case of the IIP3 of the phase shifters was 32 dBm and improved with an increased bias voltage.

CHAPTER VI

2.4 GHZ ALL-PASS NETWORK PHASE SHIFTERS

An alternative approach to further reduce circuit size and improve the performance of phase shifters is an all-pass network structure. Although distributed and reflection-type phase shifters have good performance, these topologies also have drawbacks. While wide bandwidths may be achieved with a reflection-type structure, a coupler contributes directly to the insertion loss of the phase shifter, and requires a large portion of the die area. The disadvantage of a distributed phase shifter at low frequencies is that it requires long lines to achieve the necessary phase shift. Therefore, in this chapter, two different types of all-pass network phase shifters are studied. Their analytical expression and experimental validation are reported along with the temperature characteristics and nonlinear responses of these phase shifters. In this investigation, several different BST samples were fabricated for temperature studies.

6.1 SIMPLE ALL-PASS NETWORK PHASE SHIFTERS

6.1.1 Theoretical Aspect

This phase shifter is derived from an all-pass network, which consists of two spiral inductors, four BST interdigital capacitors (IDCs) and a bias network as shown in Figure 6.1. The capacitors are the main control elements of the phase shifter, and they are series-connected on each branch in order to apply bias voltage only to capacitors. Again, IDCs

are chosen over parallel plate capacitors in order to maintain a planar process that requires no metal layers beneath a BST thin film. The spacing between fingers is 2 or 4 μm. Two inductors, of which the ratio is four, are inserted between the input and output ports and at the connection point of the capacitors.

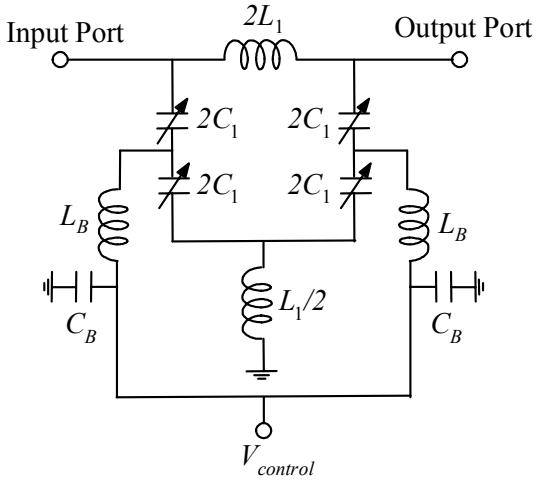

Figure 6.1 Schematic of a simple all-pass network phase shifter.

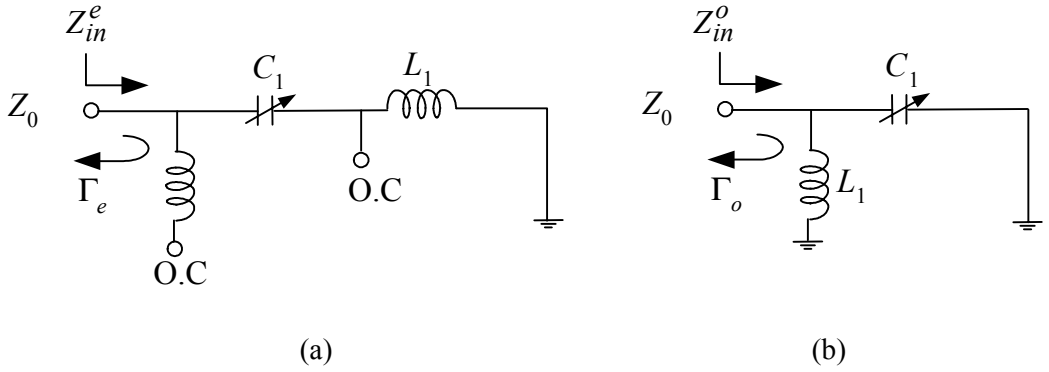

Figure 6.2 Decomposition of the simple all-pass network phase shifter into even- and odd-mode excitations. (a) Even mode. (b) Odd mode.

The reflection coefficient S_{11} and transmission coefficient S_{21} can be expressed using even-odd mode analysis. Figure 6.2 shows the decomposition of the all-pass network phase shifter. Because adding two sets of excitations generates the original excitation of

Figure 6.1, the actual response of the phase shifter can be achieved from the sum of the responses from the even- and odd-mode excitations. With reference to Figure 6.2, the even- and odd-mode reflection coefficients can be expressed as

$$\Gamma_e = \frac{Z_{in}^e - Z_0}{Z_{in}^e + Z_0} = \frac{j(\omega L_1 - (1/\omega C_1)) - Z_0}{j(\omega L_1 - (1/\omega C_1)) + Z_0} \quad , \tag{6.1}$$

$$\begin{aligned} \Gamma_o &= \frac{Z_{in}^o - Z_0}{Z_{in}^o + Z_0} = \frac{(L_1/C_1)/(j(\omega L_1 - 1/\omega C_1)) - Z_0}{(L_1/C_1)/(j(\omega L_1 - 1/\omega C_1)) + Z_0} \\ &= \frac{(1/Z_0)(L_1/C_1) - (j(\omega L_1 - 1/\omega C_1))}{(1/Z_0)(L_1/C_1) + (j(\omega L_1 - 1/\omega C_1))} \end{aligned} . \tag{6.2}$$

By applying the principles of a symmetrical lossless network, S_{11} and S_{21} are

$$S_{11} = \frac{1}{2}(\Gamma_e + \Gamma_o) = \frac{1}{2}\left(\frac{j(\omega L_1 - (1/\omega C_1)) - Z_0}{j(\omega L_1 - (1/\omega C_1)) + Z_0} + \frac{(1/Z_0)(L_1/C_1) - (j(\omega L_1 - 1/\omega C_1))}{(1/Z_0)(L_1/C_1) + (j(\omega L_1 - 1/\omega C_1))} \right), \tag{6.3}$$

$$S_{21} = \frac{1}{2}(\Gamma_e - \Gamma_o) = \frac{1}{2}\left(\frac{j(\omega L_1 - (1/\omega C_1)) - Z_0}{j(\omega L_1 - (1/\omega C_1)) + Z_0} - \frac{(1/Z_0)(L_1/C_1) - (j(\omega L_1 - 1/\omega C_1))}{(1/Z_0)(L_1/C_1) + (j(\omega L_1 - 1/\omega C_1))} \right). \tag{6.4}$$

To obtain a matched network at all frequencies (S_{11} = 0), Z_0 should be equal to $\sqrt{L_1 / C_1}$. This gives the magnitude of S_{21} of unity ($|S_{21}|$ = 1). Furthermore, if both L_1 and C_1 are changed at the same rate, the matching condition is preserved so that the reflection coefficient S_{11} should be zero. To do so, tunable inductors are required [71]. Usually, tunable inductors may be created by equivalent series or parallel LC networks, but this will result in higher loss. Therefore, in this design, only capacitance is allowed to change. The maximum and minimum resonant frequencies can be expressed as

$$\omega_{0min} = \frac{1}{\sqrt{L_1 C_{1max}}}, \tag{6.5}$$

$$\omega_{0max} = \frac{1}{\sqrt{L_1 C_{1min}}}, \tag{6.6}$$

where C_{1max} is the maximum value of the capacitor C_1 at 0 V, and C_{1min} is the minimum value at the highest bias voltage. The maximum and minimum resonant frequencies are optimized to secure a good tradeoff between a phase-shift range and loss from 2.4 GHz to 2.5 GHz.

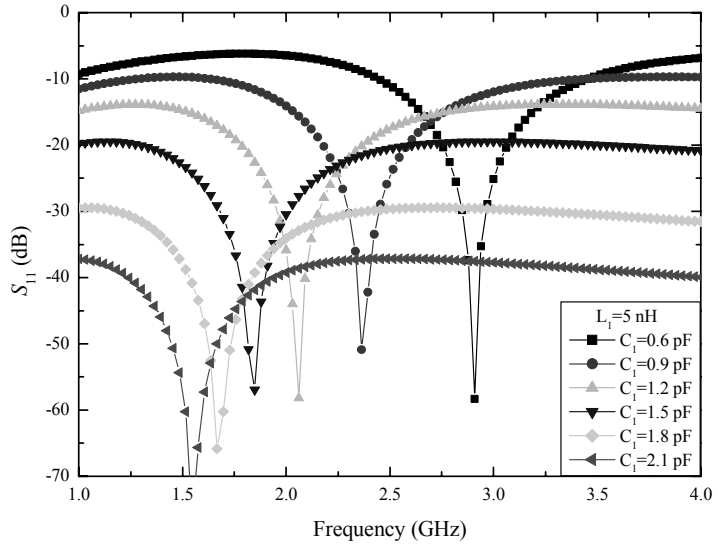

(a)

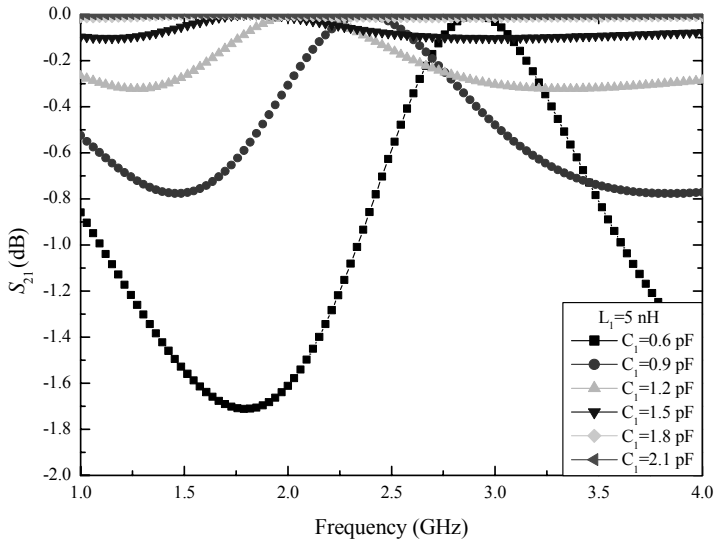

(b)

Figure 6.3 Simulated insertion and return losses of the all-pass network phase shifter.

Figure 6.3 shows the simulated insertion and return losses of the all-pass network phase shifter by changing only capacitances. With the inductance of 5 nH fixed, the capacitance is changed from 0.6 pF to 2.1 pF. Although only capacitance is changed, the return loss is higher than 10 dB for the tunability of 3.5. Also, the maximum insertion loss caused by varying capacitance is only 0.7 dB. Therefore, using only capacitors as tuning elements this phase-shifter design could be an effective approach to gain reasonable performance without the complexity involved with tunable inductors.

6.1.2 Experimental Validation: Single Section and Double Section

A photomicrograph of the fabricated single-section all-pass network phase shifter is shown in Figure 6.4. The overall size of the phase shifter is only 2.6 mm × 2.2 mm. Measured capacitance and Q-factor of the 4 μm-spaced capacitor used here as a function of bias voltage are shown in Figure 6.5. Capacitance and quality factor at 2.4 GHz were extracted using the open and short devices described in Chapter 3, resulting in 3.5 pF at 0 V and 1.25 pF at 140 V. This implies that the tunability of the capacitor, which can be defined as C(0V)/C(140V), is 2.9. Also, the minimum Q-factor of the capacitor is 28 at 0 V and is increasing as bias voltage increases. Such a high Q-factor plus a simple fabrication process is the main advantage over a parallel plate structure. The measured inductance and Q-factor of $2L_1$ are 11.5 nH and 13, respectively, whereas the values of $L_1/2$ are 2.6 nH and 20, respectively, at 2.4 GHz.

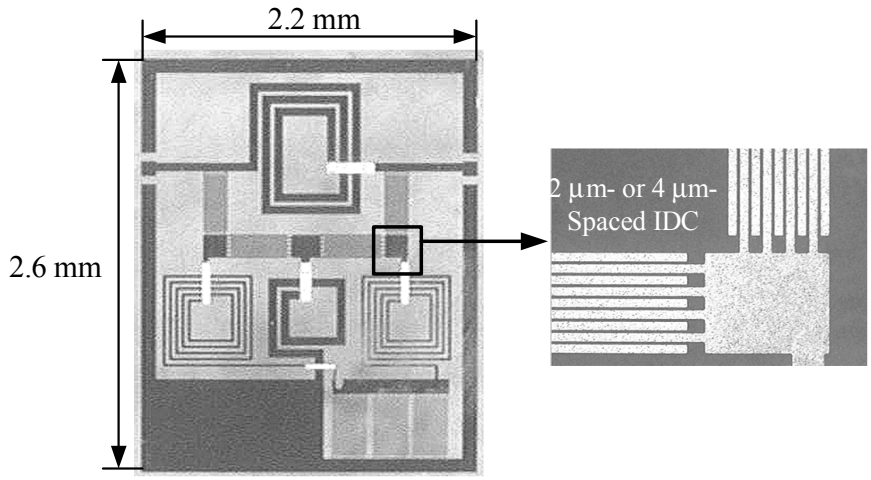

Figure 6.4 Photomicrograph of the single-section all-pass network phase shifter.

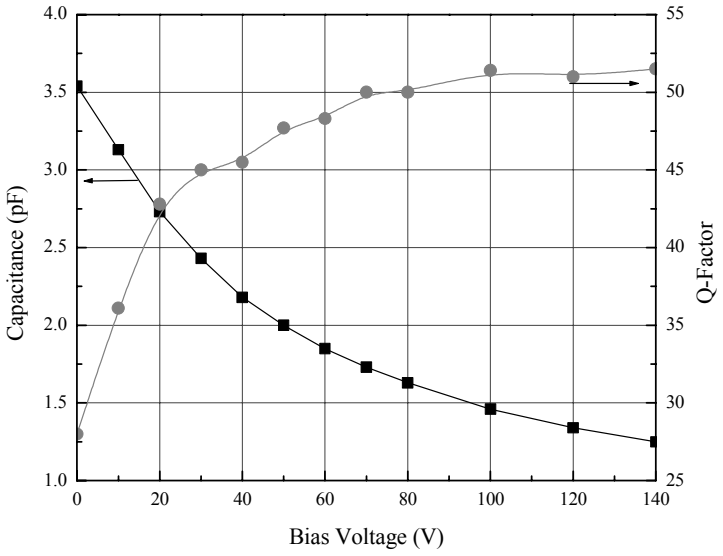

Figure 6.5 Measured capacitance and Q-factor for a capacitor at 2.4 GHz.

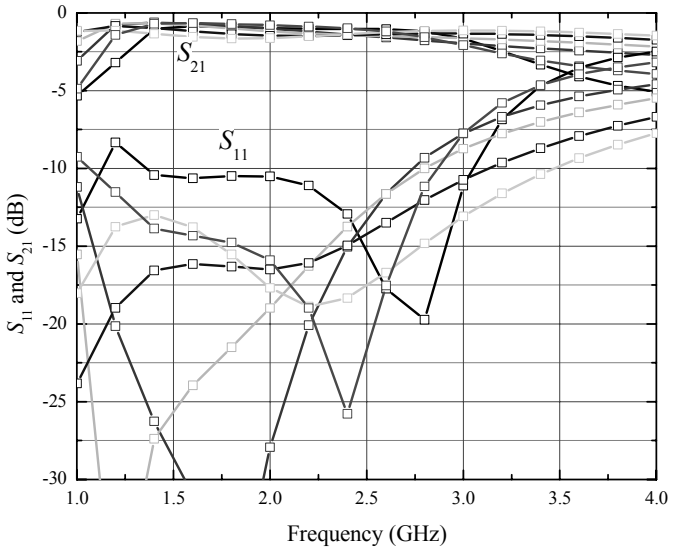

(a)

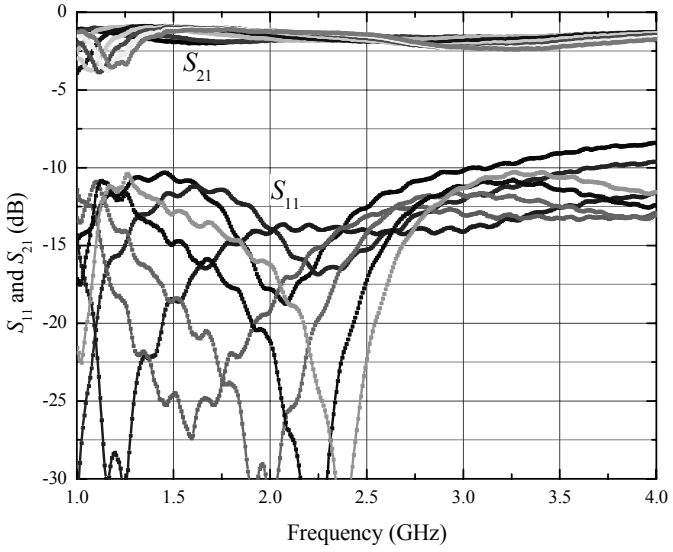

(b)

Figure 6.6 Insertion and return losses. (a) MoM simulation. (b) Measurement.

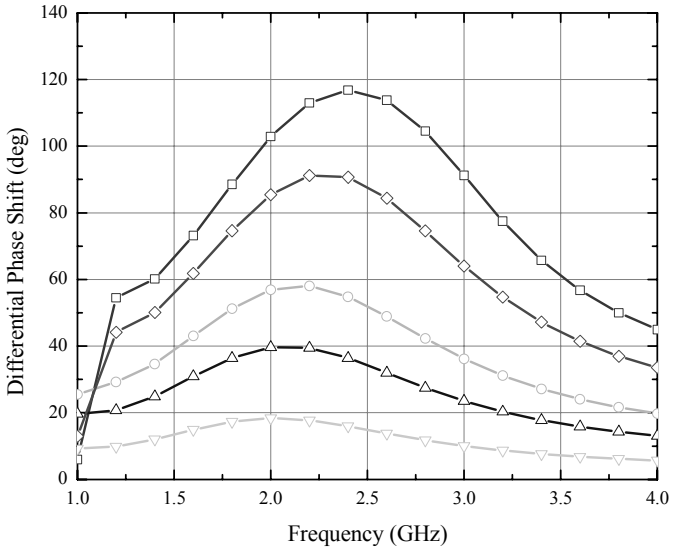

(a)

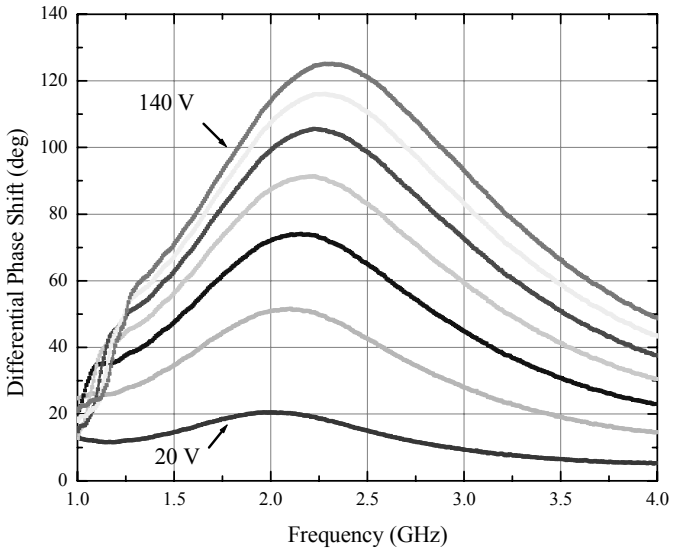

(b)

Figure 6.7 Differential phase shift with respect to the phase at 0 V. (a) MoM simulation. (b) Measurement.

Figure 6.6 shows the simulated and measured losses for the single-section phase shifter using 4 μm-spaced capacitors. The phase shifter provides a maximum insertion loss of 1.8 dB and a return loss of higher than 12.5 dB from 2.4 GHz to 2.5 GHz, as shown in Figure 6.6(b). The insertion-loss variation over all bias states is less than 0.5 dB in the same frequency range. This measured performance of the phase shifter shows pretty good agreement with the MoM simulated result in the frequency range of interest. The differential phase shift with respect to the phase at 0 V is shown in Figure 6.7. The phase shifter provides a phase-shift range of more than 121° with 140 V. Although the differential phase shift is strongly dependent on frequency, the phase variation from 2.4 GHz to 2.5 GHz is below 4° for all bias states. The loss FOM calculated from the measured *S*-parameters is more than 65°/dB from 2.4 GHz to 2.5 GHz, as shown in Figure 6.8. This result is the smallest size and the best performance obtained to date for BST phase shifters in the 2.4 GHz band.

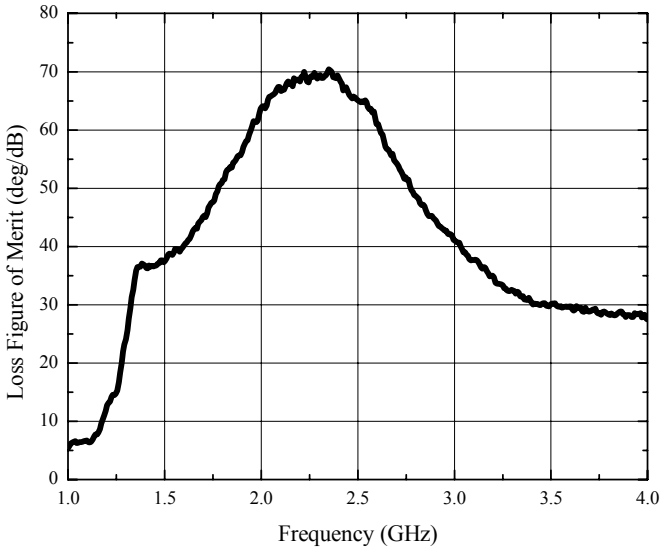

Figure 6.8 Loss FOM of the single-section all-pass network phase shifter.

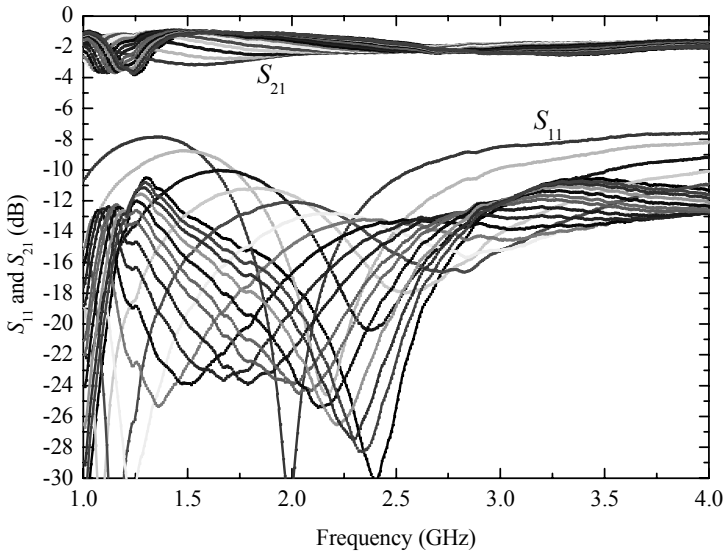

(a)

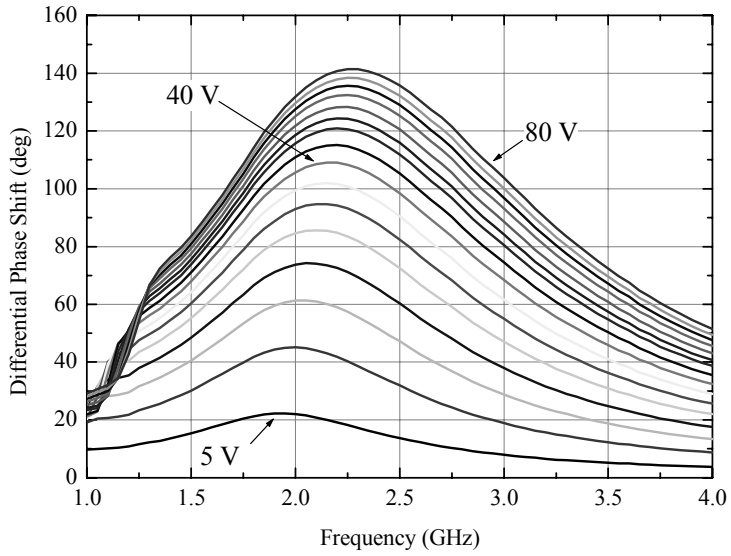

(b)

Figure 6.9 Measured result of the single-section all-pass network phase shifter with 2 μm-spaced IDCs. (a) Insertion loss and return loss. (b) Differential phase shift with respect to the phase at 0 V.

As described in Chapter 4, it is possible to further reduce bias voltage by shrinking the spacing between fingers. To demonstrate this, the single-section all-pass network phase shifter using 2 μm-spaced capacitors was implemented as well. The experimental results of the phase shifter are shown in Figure 6.9 over a bias voltage range of 0 V - 80 V. The maximum insertion loss is 2.37 dB at 2.4 GHz, and the return loss is higher than 11.5 dB for all bias states. The differential phase shift with respect to the phase at 0 V is more than 100° with 40 V. By applying up to 80 V, we can achieve a phase-shift range of more than 140°. The corresponding loss FOM is 59°/dB. The capability to reduce bias voltage to about the same level of a parallel plate capacitor by shrinking the space between fingers (~1 μm or sub-micron dimension) is a very promising result.

However, a significant amount of nonlinear distortion can be created by using smaller spaced capacitors. Consequently, depending on bias voltage, IM3 measurement should be carried out using a two-tone cancellation setup to investigate nonlinearity. This measurement setup is already discussed in Chapter 4. The experimental result for both 2 μm and 4 μm structures is shown in Figure 6.10. In the case of the phase shifter with 2 μm spaced capacitors, IM3 level is -69 dBc at the input power of -5 dBm at 1.9 GHz, and the corresponding the IIP3 is around 25 dBm. On the other hand, the IIP3 of the phase shifter with 4 μm spaced capacitors is 34 dBm at the same input power. Therefore, the IM3 power or IIP3 depends on the bias voltage of the BST IDCs, and thus the IIP3 can be significantly improved at the expense of high bias voltage (large spacing of the capacitor). Note that one approach to overcome this tradeoff between tunability and IIP3 is the reduced IMD capacitor described in Chapter 4.

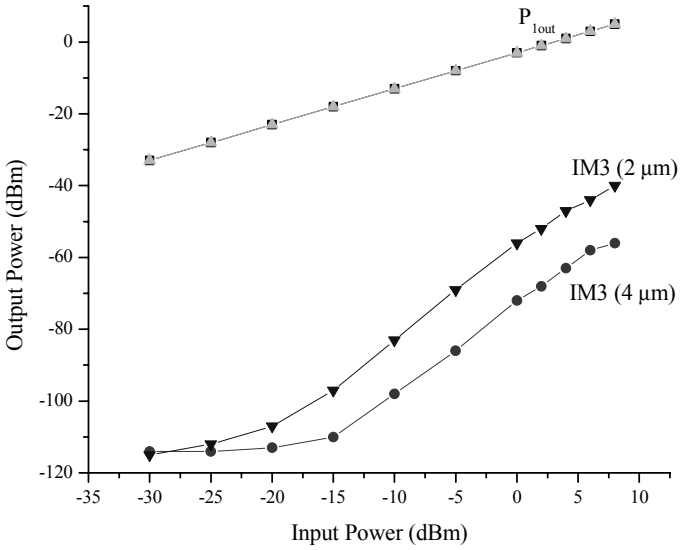

Figure 6.10 Fundamental output powers and third-order IM (IM3) products as a function of input power for two different phase shifters.

By cascading two identical single-section phase shifters, we can achieve a larger phase-shift range with the same bias voltage. A photomicrograph of the double-section phase shifter is shown in Figure 6.11. The total size of this phase shifter is 2.6 mm × 4.2 mm.

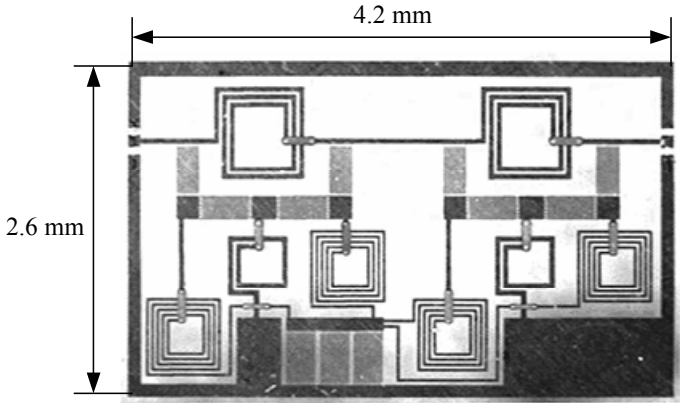

Figure 6.11 Photomicrograph of the double-section all-pass network phase shifter.

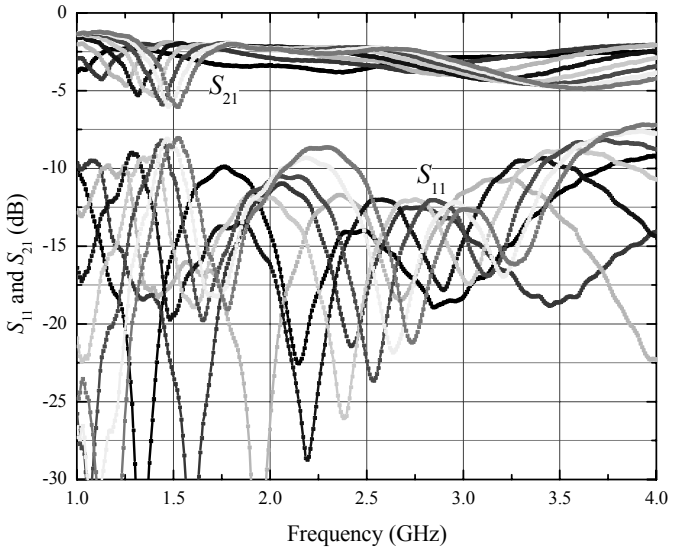

(a)

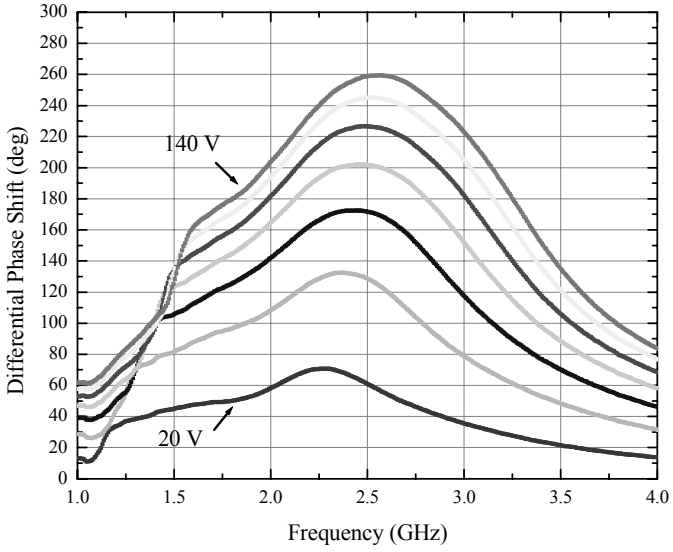

(b)

Figure 6.12 Measured result of the double-section all-pass network phase shifter. (a) Insertion loss and return loss. (b) Differential phase shift with respect to the phase at 0 V.

The measured result of the double-section phase shifter is shown in Figure 6.12. The insertion loss varies from 2.2 dB to 3.75 dB depending on a bias voltage from 2.4 to 2.5 GHz. The return loss is higher than 9.5 dB for all bias states. The measured phase shift is continuous from 0° to 255° at 2.4 GHz, and the phase variation from 2.4 to 2.5 GHz is below 5° for all bias states. With the exception of insertion-loss variation, it is seen that the cascade of two sections scales directly from the single-section phase shifter. Figure 6.13 shows the loss FOM of the phase shifter. The double-section phase shifter provides more than 68°/dB from 2.4 GHz to 2.5 GHz. Out of band, the phase shifter shows around 76°/dB at 2.55 GHz. Therefore, it is concluded that the novel and simple approach of an all-pass network structure that uses BST technology combines high performance and compact size when used in the 2.4 GHz range.

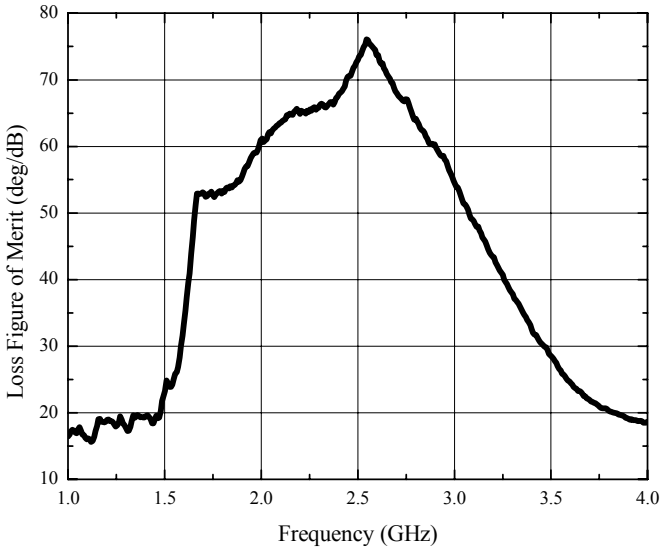

Figure 6.13 Loss FOM of the double-section all-pass network phase shifter.

6.1.3 Temperature Characteristics

As a final note on device performance, the temperature responses of the all-pass network phase shifters were investigated. As discussed in Chapter 4, it was found that the optimum composition of BST thin films with respect to minimum variation over a range of temperature used a Ba/Sr ratio of 1.2 and (Ba+Sr)/Ti ratio of 0.8 with a BST thickness of 250 nm. Therefore, it is necessary to investigate the temperature responses of the single-section phase shifters with this particular BST composition and thickness. In addition, in order to compare with the response of the phase shifter with the optimum composition, the phase shifter with a Ba/Sr ratio of 0.9 and (Ba+Sr)/Ti ratio of 0.8 was tested as well. The temperature responses of both phase shifters were measured from 1 GHz to 4 GHz. Figure 6.14 shows the variation over temperature of the phase shifter with a Ba/Sr ratio of 0.9 and (Ba+Sr)/Ti ratio of 0.8. The variation of the magnitude of S_{21} is less than 0.4 dB between 25°C and 75°C, but the phase-shift variation is more than 35° in the same temperature range. The measured result of the phase shifter with the optimum composition is shown in Figure 6.15. The variation of the magnitude of S_{21} is less than 0.5 dB between 10°C and 75°C, and the corresponding phase-shift variation is 14° at 2.4 GHz. The minimum insertion loss at 2.4 GHz is 2.1 dB at 75°C. Furthermore, if we consider temperature variation from 10°C to 50°C, then the phase-shift variation is only 4° at 2.4 GHz. The loss FOM of the phase shifter with optimum composition is shown in Figure 6.16. The maximum FOM of 65°/dB occurs at 75°C and varies from 65°/dB to 60°/dB in the temperature range of 10°C - 75°C at 2.4 GHz. Therefore, the loss FOM and phase-shift variations of this phase shifter are relatively insensitive compared with the phase shifter with a Ba/Sr ratio of 0.9 and (Ba+Sr)/Ti ratio of 0.8 because of the optimum

composition.

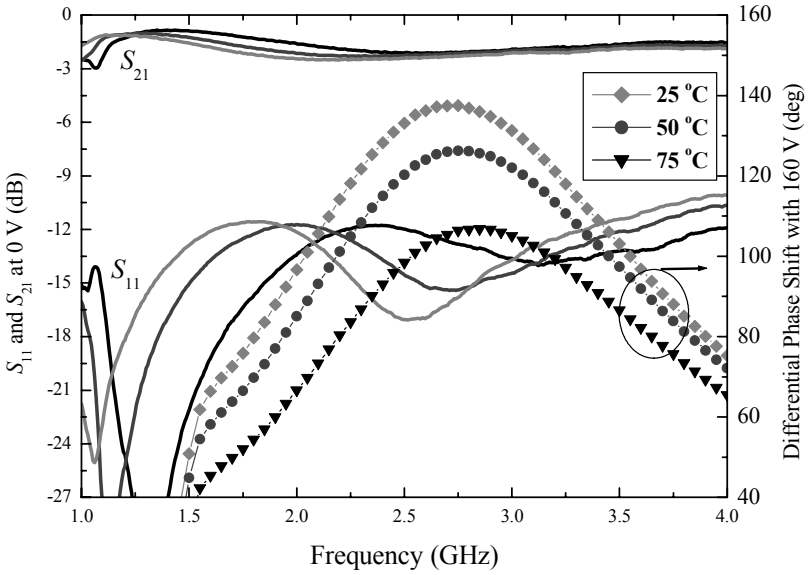

Figure 6.14 Temperature dependence of the all-pass network phase shifter (Ba/Sr = 0.9 and (Ba+Sr)/Ti = 0.8).

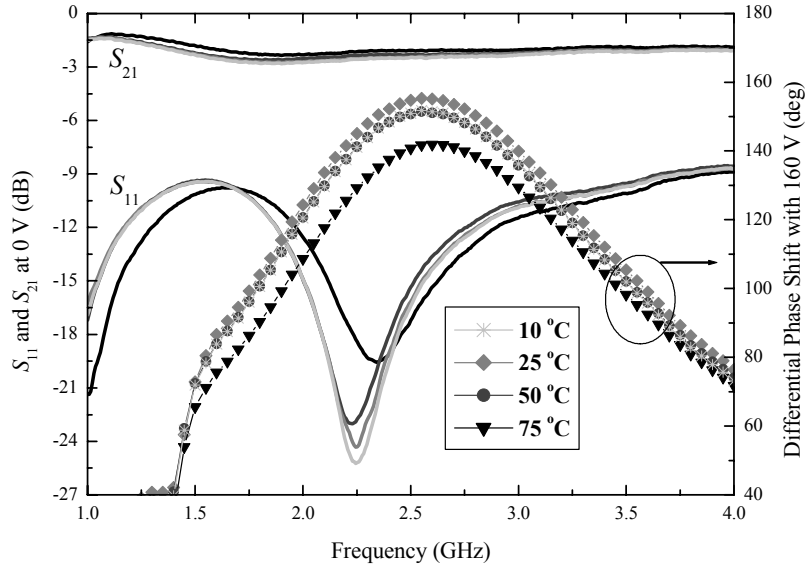

Figure 6.15 Temperature dependence of the all-pass network phase shifter (Ba/Sr = 1.2 and (Ba+Sr)/Ti = 0.8).

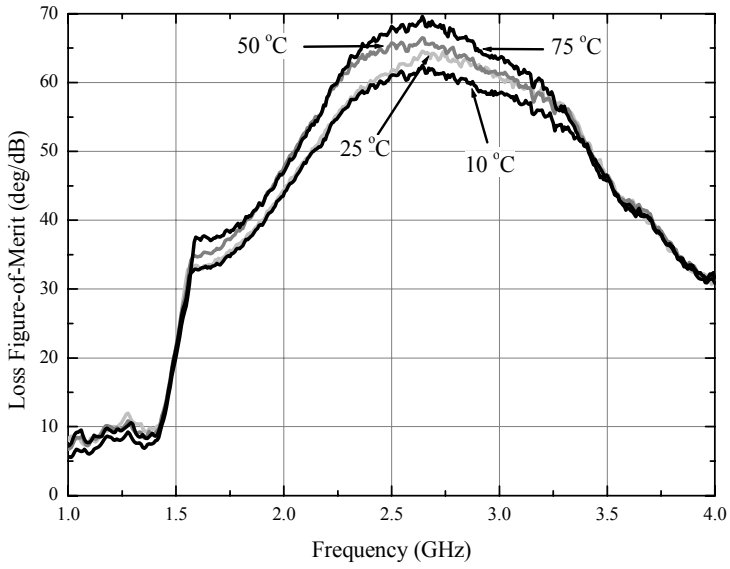

Figure 6.16 Loss FOM of a phase shifter for four different temperature states (Ba/Sr = 1.2 and (Ba+Sr)/Ti = 0.8)

6.2 PHASE SHIFTERS USING TWO QUARTER-WAVE-LENGTH TRANSMISSION LINES

In this section, another all-pass network phase shifter is introduced using π-section lumped-element networks and two variable reactances. The goal of this design aims at a larger phase-shift range while keeping the same size as the single-section all-pass network phase shifter. This design also behaves like a reactive all-pass network so that the only phase variation that will occur will be the result of a bias voltage applied to constant amplitude. The total chip area is kept to less than 6.3 mm^2 by using only lumped elements.

6.2.1 Theoretical Aspect

The phase shifter consists of two variable series resonant circuits with two identical quarter-wave-length transmission lines and a bias network, as shown in Figure 6.17. Two different series resonant circuits are connected between two identical transmission lines, resulting in an all-pass network. The total size of the phase shifter can be further reduced by employing lumped-element quarter-wave-length transmission lines, compared to [48].

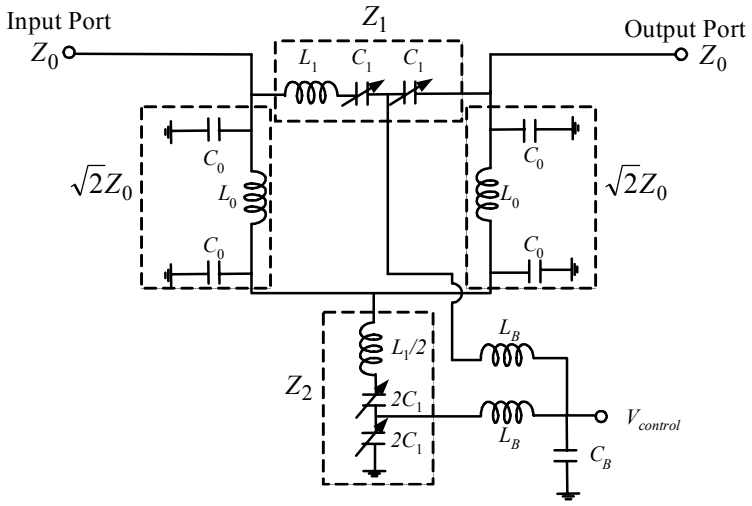

Figure 6.17 Schematic of the all-pass network phase shifter using quarter-wave-length transmission lines.

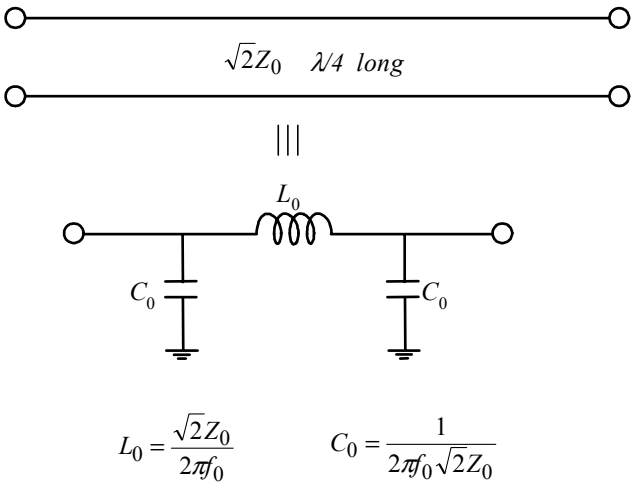

Figure 6.18 The equivalent circuit for a quarter-wave-length transmission line.

Figure 6.18 shows the equivalent circuit for a quarter-wave-length transmission line. The transmission line at frequency f_0 can be replaced by an equivalent π-section lumped-element network, and the values of the inductor and the capacitor are

$$L_0 = \frac{\sqrt{2}Z_0}{2\pi f_0}, \tag{6.7}$$

$$C_0 = \frac{1}{2\pi f_0 \sqrt{2}Z_0}, \tag{6.8}$$

where Z_0 is the characteristic impedance of each port and $\sqrt{2}Z_0$ is the characteristic impedance of the quarter-wave-length transmission lines.

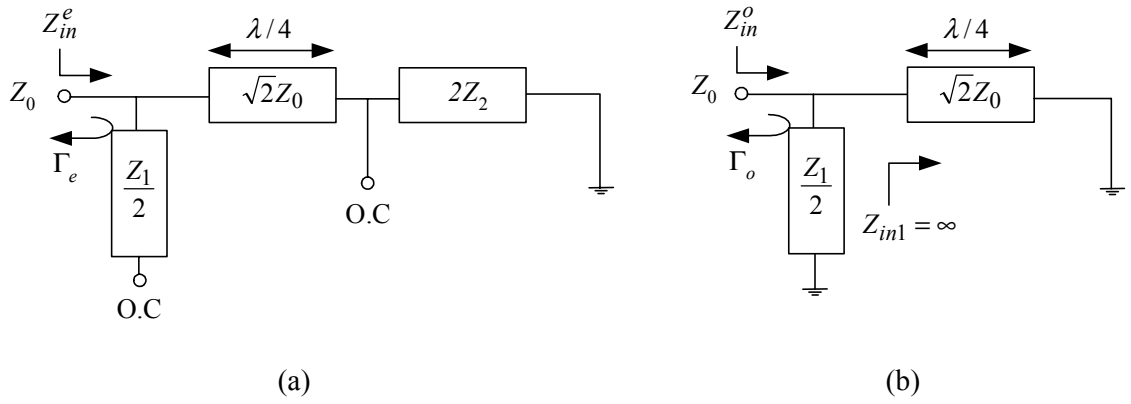

(a) (b)

Figure 6.19 Decomposition of the phase shifter into even- and odd-mode excitations. (a) Even mode. (b) Odd mode.

The reflection coefficient S_{11} and S_{22} of the phase shifter can be expressed by the sum of the even-mode reflection coefficient Γ_e and the odd-mode reflection coefficient Γ_o using even-odd mode analysis [48][49]. The phase shifter in Figure 6.17 can be decomposed into a set of two networks as shown in Figure 6.19. In order to calculate Γ_e and Γ_o, we must have

$$Z_{in}^{e} = \sqrt{2}Z_0 \frac{2Z_2 + j\sqrt{2}Z_0 \tan(\pi/2)}{\sqrt{2}Z_0 + j2Z_2 \tan(\pi/2)} = \frac{Z_0^2}{Z_2}, \tag{6.9}$$

$$Z_{in}^{o} = \frac{Z_1}{2}. \tag{6.10}$$

Then, the even- and odd-mode reflection coefficients become

$$\Gamma_e = \frac{Z_{in}^{e} - Z_0}{Z_{in}^{e} + Z_0} = \frac{Z_0^2 / Z_2 - Z_0}{Z_0^2 / Z_2 + Z_0} = \frac{Z_0 - Z_2}{Z_0 + Z_2}, \tag{6.11}$$

$$\Gamma_o = \frac{Z_{in}^{o} - Z_0}{Z_{in}^{o} + Z_0} = \frac{Z_1/2 - Z_0}{Z_1/2 + Z_0} = \frac{Z_1 - 2Z_0}{Z_1 + 2Z_0}. \tag{6.12}$$

Finally, S_{11} and S_{22} can be written as

$$S_{11} = S_{22} = \frac{1}{2}(\Gamma_e + \Gamma_o) = \frac{Z_0(Z_1 - 2Z_2)}{(Z_0 + Z_2)(2Z_0 + Z_1)}. \tag{6.13}$$

Therefore, we can preserve the matching condition by setting the values of two variable impedances with the following relationship

$$Z_2 = \frac{Z_1}{2}. \tag{6.14}$$

In this case, the transmission coefficient S_{21} and S_{12} can simply be expressed as

$$S_{21} = S_{12} = \frac{1}{2}(\Gamma_e - \Gamma_o) = \frac{2Z_0 - Z_1}{2Z_0 + Z_1}. \tag{6.15}$$

If we consider a lossless network and variable reactances jX_1 and jX_2 as variable impedances Z_1 and Z_2, respectively, then the phase of the phase shifter can be expressed as

$$\tan\phi_T = \frac{\sin\phi_T}{\cos\phi_T} = \frac{4Z_0X_1}{X_1^2 - 4Z_0^2}, \tag{6.16}$$

$$\angle\phi_T = \tan^{-1}\left(\frac{4Z_0X_1}{X_1^2 - 4Z_0^2}\right) = \pi - 2\tan^{-1}\left(\frac{X_1}{2Z_0}\right), \tag{6.17}$$

resulting in the phase variation of

$$\Delta\phi = 2\left[\tan^{-1}\left(\frac{X_{1max}}{2Z_0}\right) - \tan^{-1}\left(\frac{X_{1min}}{2Z_0}\right)\right], \tag{6.18}$$

$$X_{1max} = \left(\omega L_1 - \frac{1}{\omega C_{1max}}\right), \tag{6.19}$$

$$X_{1min} = \left(\omega L_1 - \frac{1}{\omega C_{1min}}\right), \tag{6.20}$$

where X_{1max} and X_{1min} are the maximum and minimum reactance, respectively. The maximum phase shift will occur when the maximum reactance (X_{1max}) is set equal to the minimum reactance with opposite sign ($-X_{1min}$). The corresponding inductance L_1 and the maximum phase shift for a lossless network can be expressed as

$$L_1 = \frac{1}{\omega^2 C_{1min}}\left(1 + \frac{1}{r}\right), \tag{6.21}$$

$$\Delta\phi_{max} = 4\tan^{-1}\left[\frac{1}{2\omega Z_0 C_{1min}}\left(1 - \frac{1}{r}\right)\right], \tag{6.22}$$

where r is the ratio of the maximum and minimum capacitance of C_1. In this design, two identical capacitors are series connected on each branch in order to apply bias voltage to only capacitors.

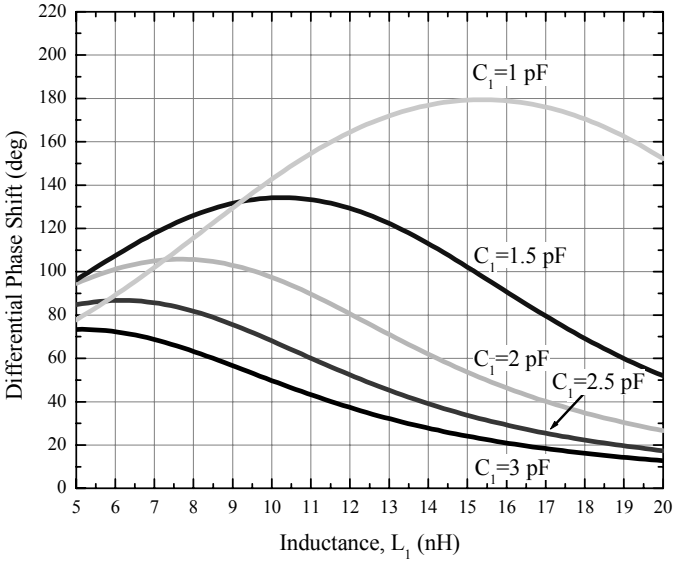

(a)

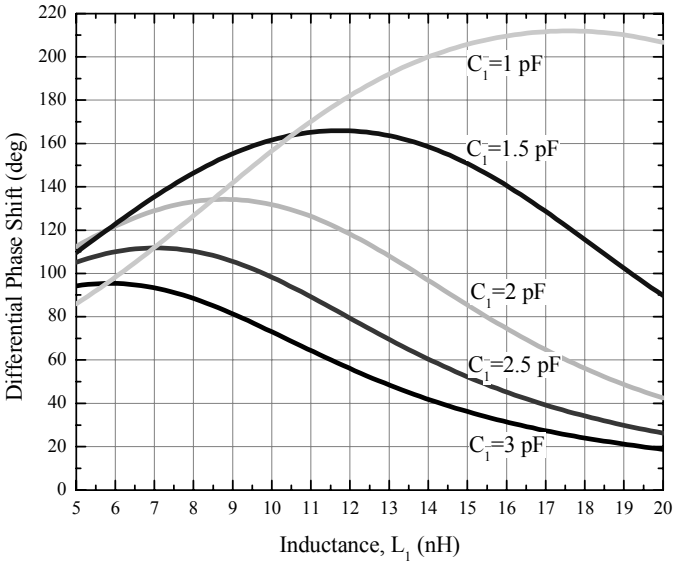

(b)

Figure 6.20 Differential phase shift as a function of inductance for different values of capacitor C_1. (a) Tunability, $r = 2.5$. (b) Tunability, $r = 3$.

Figure 6.20 shows the differential phase shift versus the inductance of L_1 for the different values of C_1 at 2.4 GHz. In this case, the tunability r of 2.5 and 3.0 is chosen because these values can be easily achieved using BST IDCs. The maximum phase shift using the given tunability such as r = 2.5 or 3.0 is increasing with the higher optimal inductance of L_1 and the lower capacitance of C_1. For example, the maximum phase shift of 180° is achievable with C_1 = 1 pF and L_1 = 15 nH at 2.4 GHz using r = 2.5, whereas the maximum phase shift is only 70° with C_1 = 3 pF and L_1 = 5 nH. However, the higher inductance and lower capacitance can increase device loss because of higher resistive parasitics. Therefore, there is a tradeoff between the maximum phase shift and the insertion loss of the device with the given tunability.

6.2.2 Experimental Validation

The photomicrograph in Figure 6.21 shows the fabricated all-pass network phase shifter. The overall size of the phase shifter is less than 2.6 mm × 2.4 mm, which is almost same size as the single-section all-pass network phase shifter.

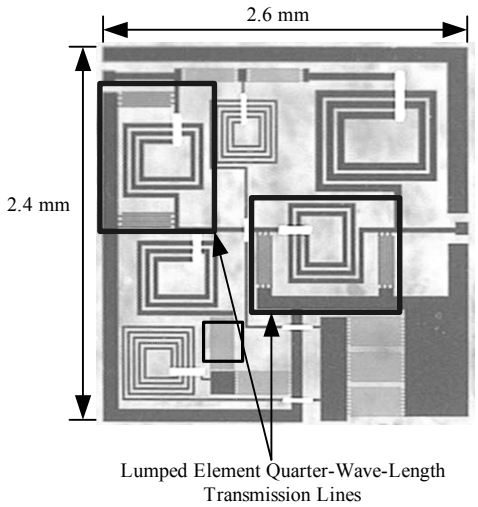

Figure 6.21 Photomicrograph of the all-pass network phase shifter using quarter-wave-length transmission lines.

Figure 6.22 illustrates measured result of the phase shifter with a Ba/Sr ratio of 1.33, (Ba+Sr)/Ti ratio of 1.0, and BST thickness of 350 nm. The average insertion loss of the phase shifter is 3.2 dB and the worst-case insertion loss is 4.4 dB from 2.4 GHz to 2.5 GHz. The return loss is higher than 10 dB in the same frequency range for all bias states. By applying a bias voltage of 180 V, we can achieve a phase shift of more than 147°. Also, the phase variation from 2.4 GHz to 2.5 GHz is only ± 2°.

The measured result of the phase shifter with a Ba/Sr ratio of 1.2, (Ba+Sr)/Ti ratio of 0.8, and BST thickness of 250 nm is shown in Figure 6.23. In this case, the BST thin film was treated by heat in a conventional furnace at 550°C for 3 hours in an N_2 atmosphere to increase capacitance and tunability [65]. The return loss of the phase shifter is higher than 15 dB at 2.4 GHz for all bias states. A phase-shift range of 183° is obtained with a maximum insertion loss of 5.5 dB at 2.4 GHz. Out of band, the phase shifter provides a phase-shift range of 177° with a return loss of higher than 18 dB and a maximum insertion loss of 4.4 dB. Therefore, the loss FOM of the phase shifter is ~40°/dB at 2.1 GHz and ~33°/dB at 2.4 GHz. Compared with the simple all-pass network phase shifter, the total chip size of this phase shifter is almost the same but a higher phase-shift range can be obtained. However, this phase shifter needs more elements than a simple all-pass network phase shifter, so this design has a quite low yield in terms of fabrication. The phase-shift range can be increased up to 300° by cascading two phase shifters.

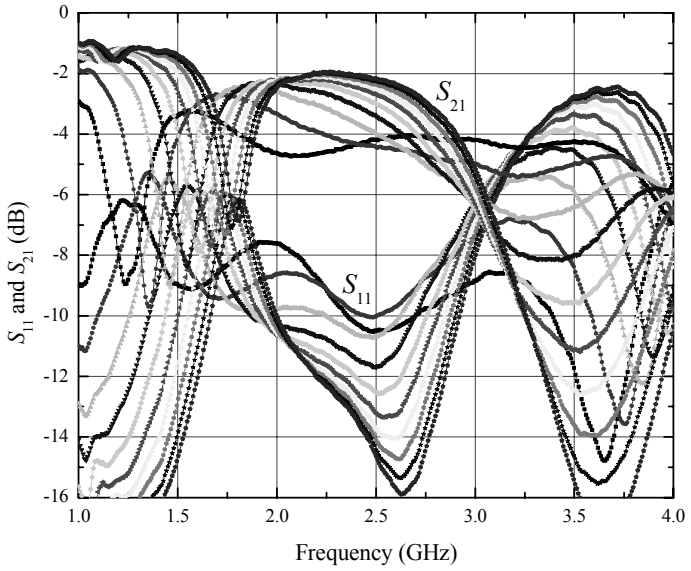

(a)

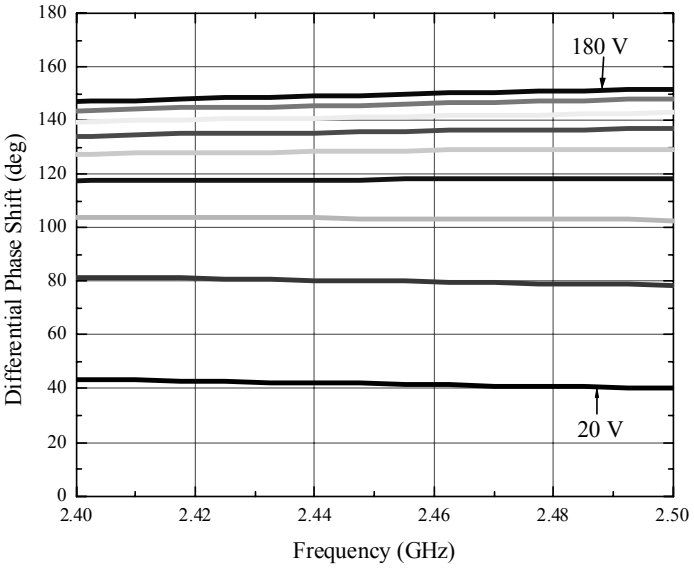

(b)

Figure 6.22 Measured result of the phase shifter for bias voltages from 0 V to 180 V. (a) Insertion and return loss. (b) Differential phase shift with respect to the phase at 0 V.

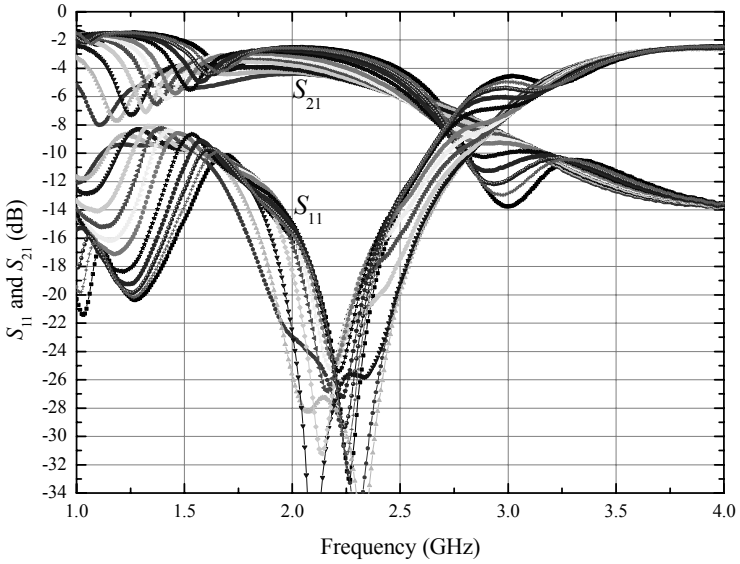

(a)

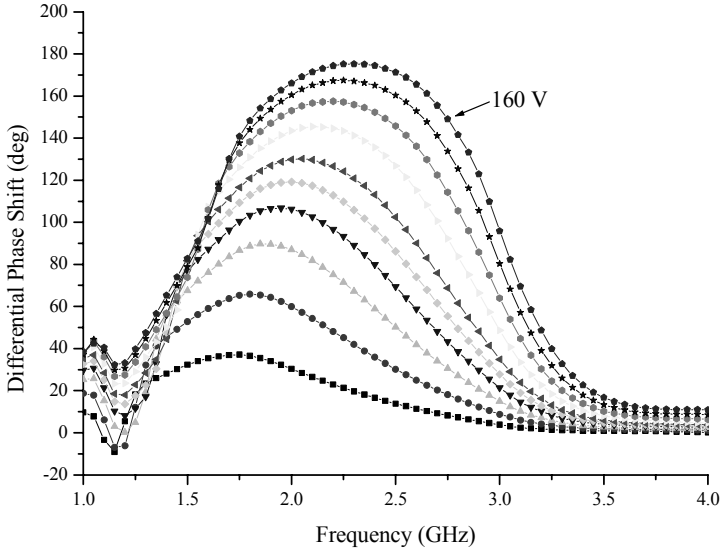

(b)

Figure 6.23 Measured result of the phase shifter for bias voltages from 0 V to 160 V. (a) Insertion and return loss. (b) Differential phase shift with respect to the phase at 0 V.

6.2.3 Temperature Characteristics

The temperature response of the phase shifter was investigated as well. At room temperature, a phase-shift range of more than 177° is achieved with a maximum insertion loss of 4.4 dB at 2.1 GHz. The return loss at the same frequency is higher than 18 dB for all bias states. By increasing the temperature, the phase-shift range decreases from 177° to 146°. Note that the phase-shift variation of the phase shifter is larger than that of the simple all-pass network phase shifter because of the varying value of the lumped-element transmission lines. However, the variation of the loss FOM is less than 4°/dB from 25°C to 75°C by decreasing the insertion loss.

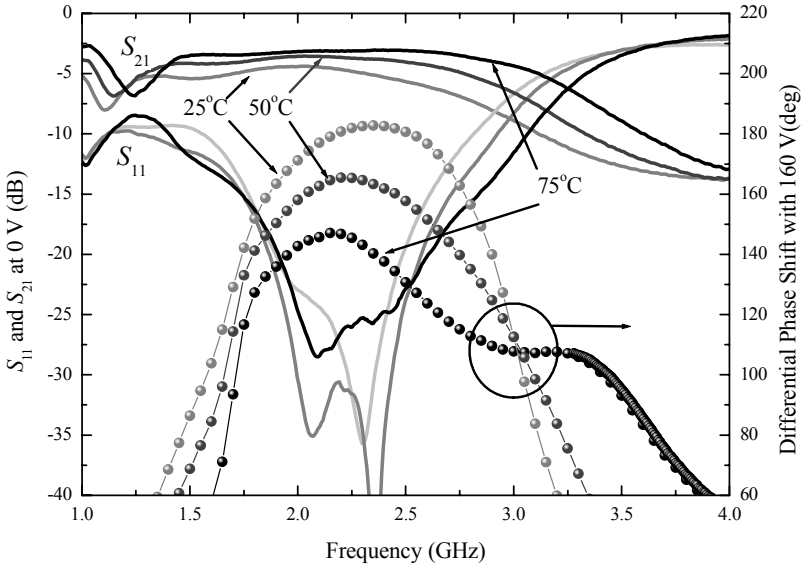

Figure 6.24 Temperature dependence of an all-pass network phase shifter using quarter-wavelength transmission lines.

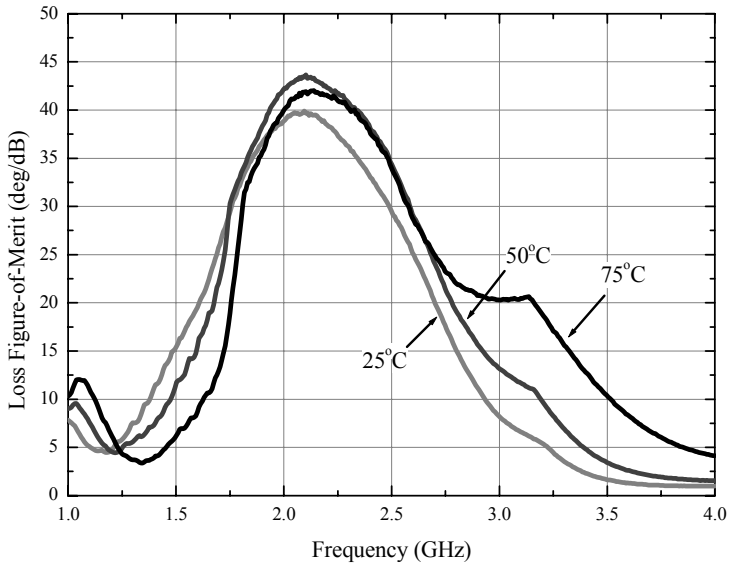

Figure 6.25 Loss FOM of the phase shifter at three different temperature states.

6.3 CONCLUSIONS

In this chapter, the design of all-pass network phase shifters was discussed. Two different types of all-pass network structures were implemented using a lumped-element approach so that the overall size of both configurations is less than 2.6 mm × 2.4 mm. Theoretical analyses that incorporated the optimum phase-shift range and loss mechanism were performed to predict the actual response of both phase shifters. The performance of a simple all-pass network phase shifter was found to have the best loss FOM and the smallest size obtained to date for BST phase shifters in the 2.4 GHz band. This promising result compares with or surpasses similar designs implemented using GaAs MMICs. In addition, it was determined that this phase shifter was minimally affected by changes in temperature. The phase shifter using π-section lumped-element quarter-wave-length

transmission lines was fabricated to show that this design was capable of providing a phase-shift range of 180° while retaining its compact size. Additionally, with incorporation of smaller spaced capacitors, it would offer the benefit of reducing bias voltage at the expense of nonlinearity. For instance, a phase-shift range of more than 100° could be obtained using 2 μm-spaced IDCs with an applied bias voltage of 40 V. The corresponding IIP3 is around 28 dBm, whereas the IIP3 of the phase shifter with 4 μm-spaced IDCs is 36 dBm.

In future investigations, phase shifters operating in other frequency range such as 5 GHz for IEEE 802.11a or millimeter wave for military applications will have to be fabricated. The performance of the phase shifter can be further improved by implementing low loss inductors that appear possible by a thicker metallization layer or MEMS approach. In the next chapter, compact BFN based on the phase shifters, which are described in Chapter 5 and Chapter 6, will be explored for WLAN systems.

CHAPTER VII

BST BEAMFORMING NETWORKS (BFNS) FOR WLAN SYSTEMS USING CLIENT-BASED SMART ANTENNAS

The final topic to be investigated is a beamforming network (BFN) employing BST phase shifters for WLAN systems using client-based smart antennas. A WLAN based on the IEEE 802.11b standard, which transmits at 2.4 GHz and sends data up to 11 Mbps using direct sequence spread spectrum (DSSS) modulation, has become dramatically popular over the last few years. Formerly used only in high mobility applications, such as factories, warehouses, and hospitals, WLAN cards are now being purchased by consumers simply for convenience. However, the IEEE 802.11b standard operates in an unlicensed band, and thus, within these bands, other wireless devices such as cordless phones or unintentional radiators such as microwave ovens create significant amounts of interference at the mobile unit receiver. One promising method to reduce interference is to use smart antenna systems that can increase throughput and network capacity by rejecting interference.

Smart antennas can be classified into two categories: adaptive antennas and switch beam technologies [72]. In the latter technology, a number of fixed beams produced by a fixed BFN such as a Butler matrix are used by a switch to select the best beam to receive a particular signal. This system requires relatively simple implementation but may not provide the degree of performance improvement offered by adaptive antenna systems. On the other hand, despite their complexity, better performance can be achieved by adaptive

antenna systems able to change their antenna patterns dramatically. Such variable antenna patterns may adjust to noise, interference, and multipath by using phase differences generated by phase shifters operating among an array of antennas. Therefore, a WLAN employing adaptive antenna systems has been proposed as a way to improve capacity by applying spatial filtering to separate carrier signals from interference based on their angle of arrival.

In cellular systems, the smart antenna system is usually restricted to the base station because the angle of arrival is small and predictable, whereas WLAN systems enjoy the advantage of smart antenna systems because the propagation channel of WLAN systems is not as varying as rapidly in cellular systems. The ability to make a small-size, low-cost, and high-performance BFN into reality becomes the constraint for WLAN mobile clients. The trend toward such a BFN involves a strong demand for low-cost and compact-size variable phase shifters with a large phase-shift range and low insertion loss. Consequently, such a BFN is one of the most important applications of BST phase shifters.

In this final chapter, to validate the feasibility of BST technology, the compact BFNs of a WLAN client smart antenna system are discussed. In this adaptive antenna system we are going to use the null point in the radiation pattern in order to reduce the interference signal. Hardware descriptions and throughput improvement of WLAN systems are described.

7.1 DESCRIPTION AND SIMULATION OF THE SYSTEM

The two-element smart antenna system allows a non-isotropic pattern in azimuth, which makes possible the separation between the carrier and interference signal. The schematic of the system used for simulation is shown in Figure 7.1. Details of simulation conditions

and results were presented in [73]. A summary is as follows. The carrier signal is a QPSK modulated signal and the interference source is considered to emit a white Gaussian noise uniformly within the band of interest. To make the simulation more realistic, some effects of the propagation environment are introduced: Path-loss (both Line-of-Sight (LoS) and NonLine-of-Sight (NLoS)) and Multipath-fading caused by scattered signals arriving at different times from difference angles. We assume that we are in an indoor environment, and that any delay spread will be equalized by the receiver. Thus, the model will only estimate the ratio of signal power to interference power.

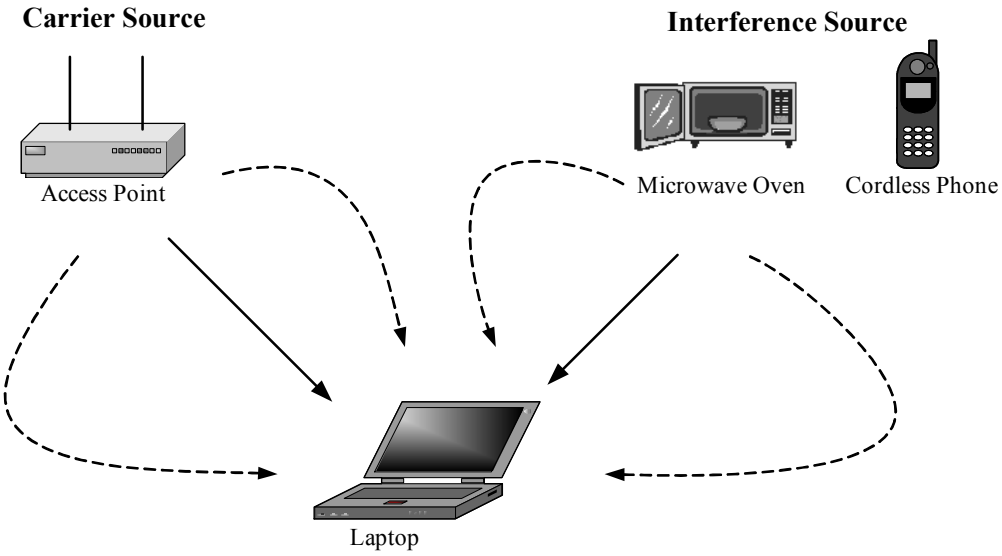

Figure 7.1 Scheme of the system used for the simulation.

With reference to [73], if we considered five scattered paths in addition to LoS for both the transmitter and the interference source and the LoS angle of arrivals were separated by 40°, then a 6 dB improvement was seen over a wide range of SNR. As the number of scatterers increases to 20, the improvement is diminished to 3 dB. Averaging over many angles of arrival, the C/I improvement in sparse scattering environments (5 to 10) showed

improvements ranging from 3 to 7 dB. However, when the number of scatterers was increased to 20 or 50, in most case the improvement diminished to 3 dB or less. Figure 7.2 shows the simple block diagram of a WLAN system connected to two-element BFN. To apply a high static bias voltage to both phase shifters, a phase-shifter driver, which was realized by LT3420 DC-DC converter from Linear Technologies, Inc., was used along with tracking software for beam scanning. The output voltage for each element was controlled by the MCP42100 digital potentiometer from Microchip Technology, Inc.

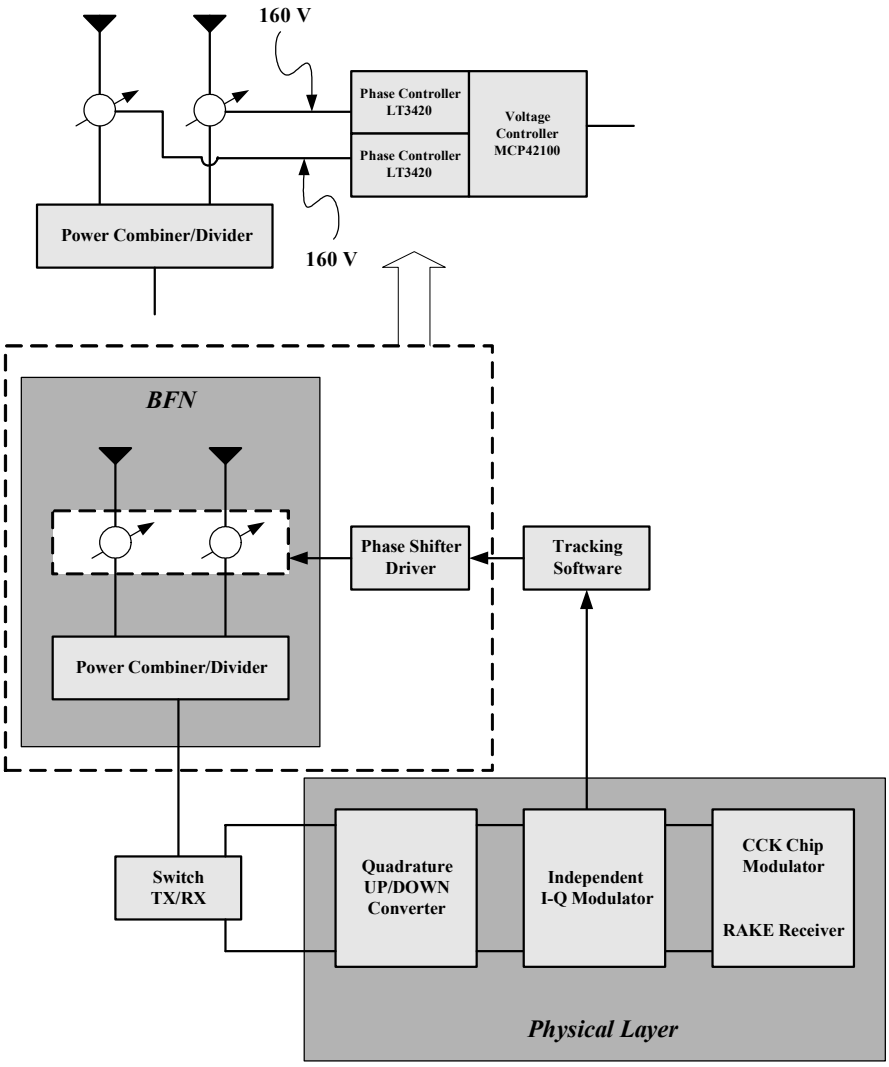

Figure 7.2 Simplified block diagram of the WLAN system connected to a two-element BFN.

7.2 Hardware Description and Measurement of Two-Element BFNs

The first attempt to realize a two-element BFN is a hybrid approach [74]. Each BST phase shifter was packaged on leadless chip carrier (LCC) packages with 20 pins from Kyocera Inc., and connected to a commercial power divider from Anaren Inc., as shown in Figure 7.3. To interconnect the phase shifter and package, standard silver bond wires were used. It was necessary to add external matching networks on both input and output ports using additional off-chip inductors and capacitors on a test board in order to compensate for the effect of parasitic inductance generated from bond wires. Additionally, the LT3420 DC-DC converter described in the previous section was used to apply a high static bias voltage to operate the phase shifters. The external antenna signal from an Orinoco 802.11b WLAN NIC card was fed into the BFN PCB assembly through a coaxial cable, and external inverted-F antennas were connected through SMA cables to radiate the signal.

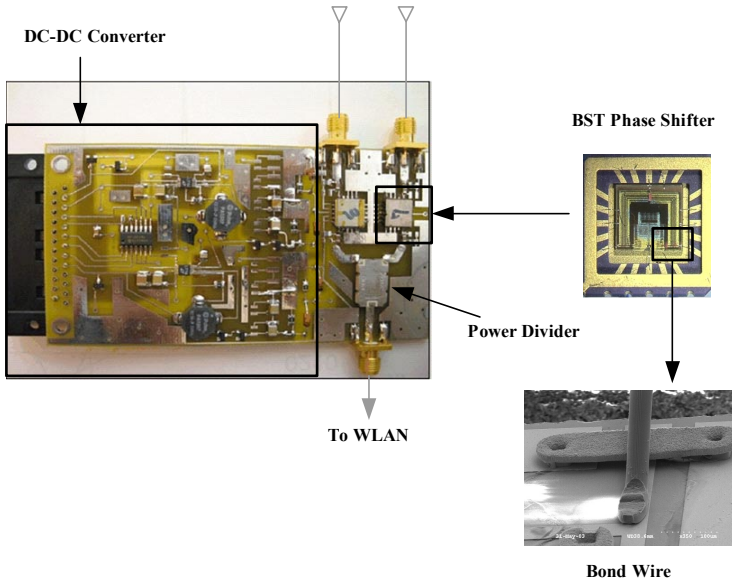

Figure 7.3. Photograph of the BFN, packaged phase shifter, and bond wire.

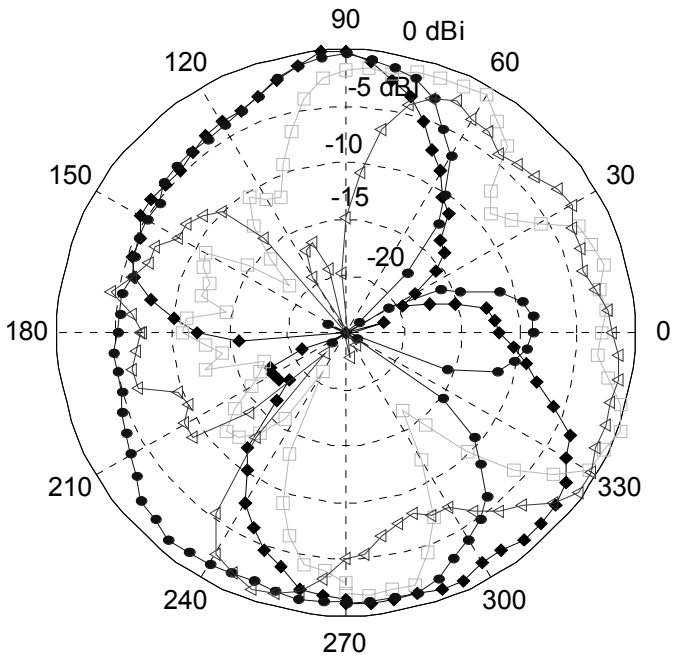

Figure 7.4 Measured beam pattern with phase difference of 0° (diamond), -90° (circle), 90° (square), and 60° (triangle).

To predict a direction of a null point in the radiation pattern, antenna beam pattern measurement should be carried out with the calibration of phase offset in the BFN. Figure 7.4 illustrates the measured beam pattern with four different phase differences. In spite of inaccuracy in an outdoor antenna range setup, it is enough to know the direction of the null point in the radiation pattern because only the receiving mode would be considered in this experiment.

Another attempt to implement the BFN incorporates an integrated BFN on a BST coated substrate. The successfully fabricated BFN is shown in Figure 7.5. The BFN is composed of two identical all-pass network phase shifters connected to a Wilkinson power divider. All devices were fabricated directly onto the BST coated substrate, and thus the overall size of the BFN is only 6 mm × 5.6 mm. Unfortunately, however, the

integrated BFN didn't work properly at this time because an unexpected coupling and/or matching problem among each port occurred so that each port reflected excessive power after loading a 50 ohm load. Nevertheless, we can predict the overall performance of this integrated BFN by incorporating the measured data of the power divider and the phase shifter.

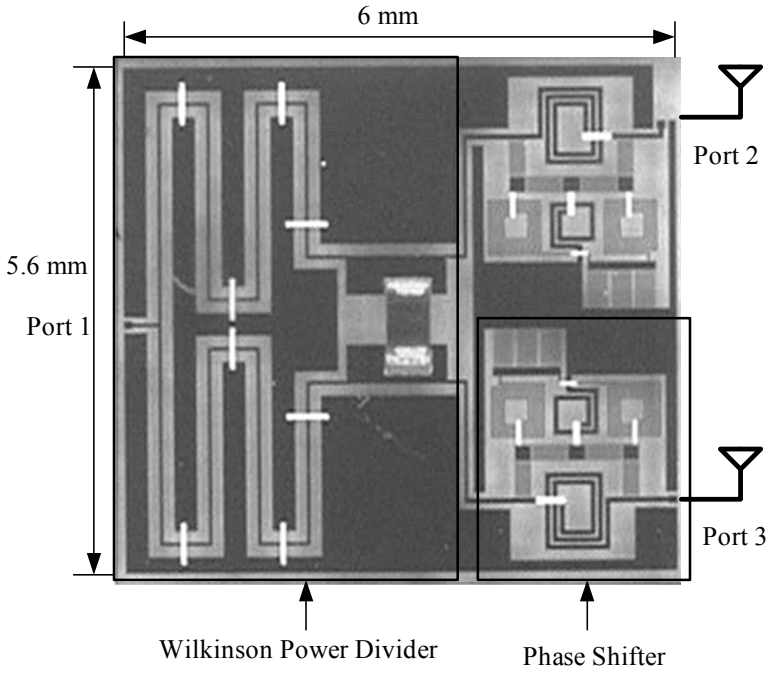

Figure 7.5 Photomicrograph of the integrated two-element BFN.

An equal-split Wilkinson power divider consists of two branches and a lumped resistor. The resistor is inserted between two output ports to provide isolation. The resistance of the lumped resistor is 100 Ω. A photomicrograph and measured result of the fabricated Wilkinson power divider are shown in Figure 7.6. The power divider provided an insertion loss of 3.8 dB (actual loss is 0.8 dB) with phase difference of only 1° between each output port. The return loss is higher than 25 dB and the isolation between each output port is more than 36 dB from 2.4 GHz to 2.5 GHz. Therefore, the power divider

based on the BST thin film offers good performance with a compact size. Figure 7.7 shows the expected integrated BFN performance from measured data of the power divider and the phase shifter discussed in the previous chapter. The maximum loss of the BFN is about 6.3 dB, and the return losses at port 1 and port 2 are higher than 17 dB and 10 dB, respectively, in the range of 2.4 GHz - 2.5 GHz. The phase difference between each port is more than 140°, and thus the total achievable phase difference of this BFN is more than 280°.

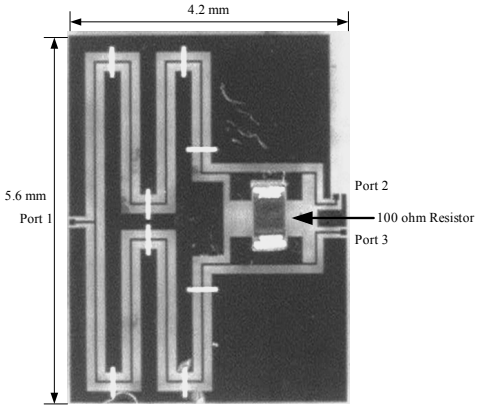

(a)

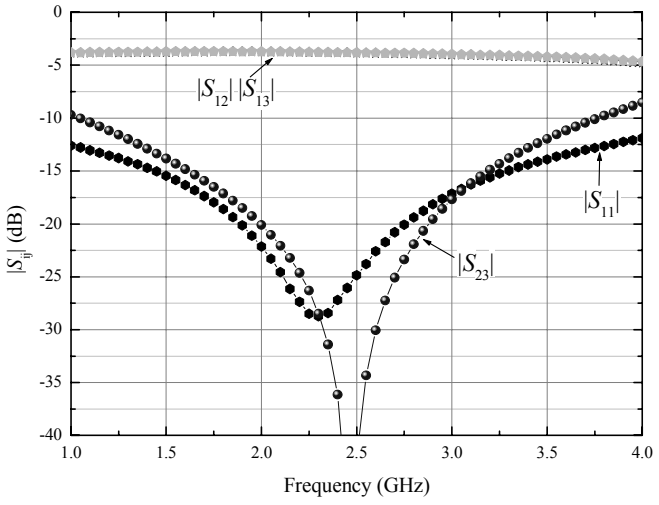

(b)

Figure 7.6 Wilkinson power divider based on a BST coated sapphire substrate. (a) Photomicrograph. (b) Measured result.

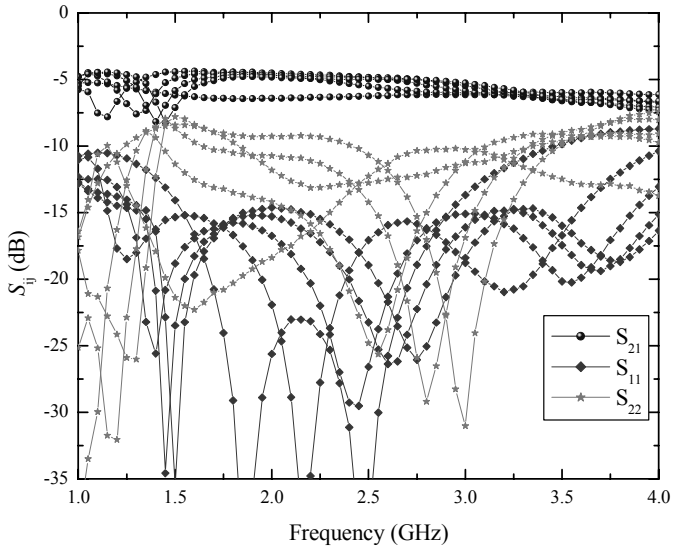

(a)

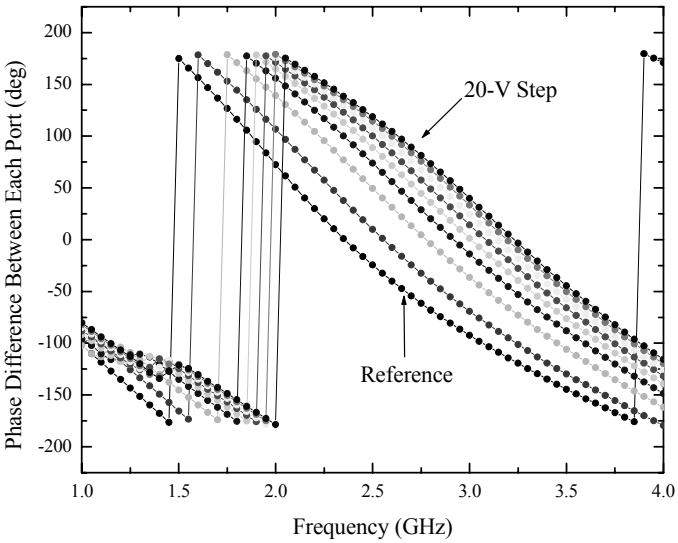

(b)

Figure 7.7 BFN performance from measured data of the power divider and phase shifters.

7.3 EXPERIMENTAL VALIDATION OF THROUGHPUT IMPROVEMENT

IEEE 802.11b provides 11Mbps, 5 Mbps, 2 Mbps and 1 Mbps data rates. All these connections are determined by the number of channels in frequency bands and the SNR in a station and an access point (AP). By adopting smart antenna systems, spatial filtering using noise cancellation can be achieved. As a consequence, rejecting an interference signal can provide a better SNR so that it can provide a higher data rate. Figure 7.8 shows how much of an interference signal can be rejected in an indoor environment by scanning a null point of the radiation pattern. In this experiment the beam was steered in azimuth over the entire 180° coverage range. A conventional WLAN AP located more than 10 meters away from a PC was the signal source, and an interference source (2.42 GHz CW signal with dipole radiator) was placed in the proximity of the antenna. The experiments took place in an enclosed indoor laboratory measuring approximately 10 m x 15 m. No special care was taken to minimize multipath scattering within the lab.

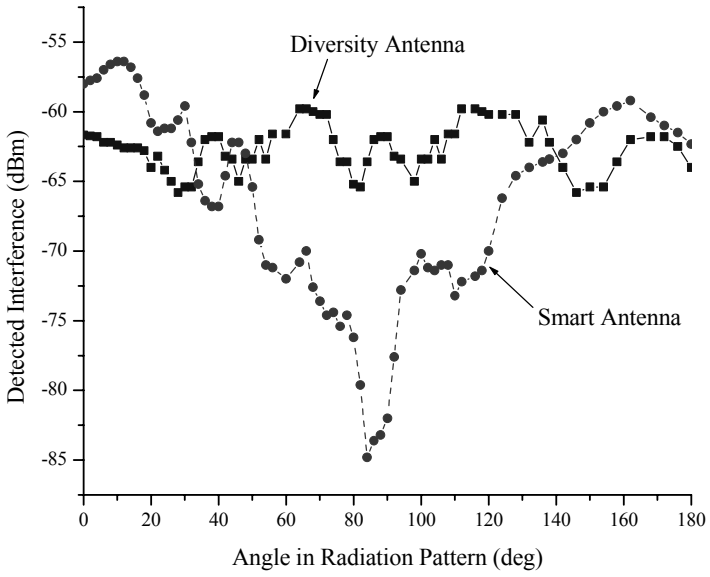

Figure 7.8 Rejection of interference signal versus angle of beam.

According to [75], the data rate can be affected by the SNR in the network. However, with a higher SNR, such as 25 dB or larger, the data rate is more affected by the number of channels than by SNR. So, significant improvement in throughput performance may be expected below 25 dB SNR under limited interference conditions. The experiment to observe throughput improvement was set up in sparsely scattering and densely scattering environments in an infrastructure mode. To provide a consistent data rate, instead of internet service, an FTP server was connected to the AP, and the mobile station with the smart antenna was the only user in the channel. To simulate a dense scattering indoor environment, about 20 scatterers were randomly deployed between the AP and the station with the smart antenna. In the sparse scattering outdoor environment, fewer than 5 scatterers were used. Both cases considered the presence of LoS from a carrier signal and an interference signal. As can be seen in Figure 7.9 and Figure 7.10, throughput with a smart antenna system is better than with a diversity antenna both in indoor and outdoor environments when LoS from carrier and interference sources exists. However, the improvement is more significant in the outdoor environment. Comparison between Figure 7.9 and Figure 7.10 was also predicted by the simulation results in [73] for different scenarios of the number of scatterers. We also considered the case of NLoS for the carrier signal and LoS for the interference, resulting in a poor connection between the WLAN and the AP, as shown in Figure 7.11.

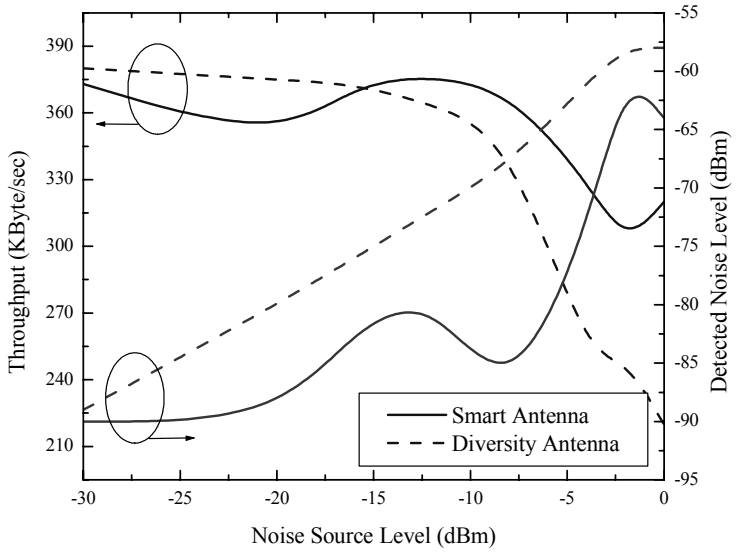

Figure 7.9 Measured throughput and detected noise level in an indoor environment. (Carrier: LoS, Interference: LoS, and 54 dB SNR at the AP).

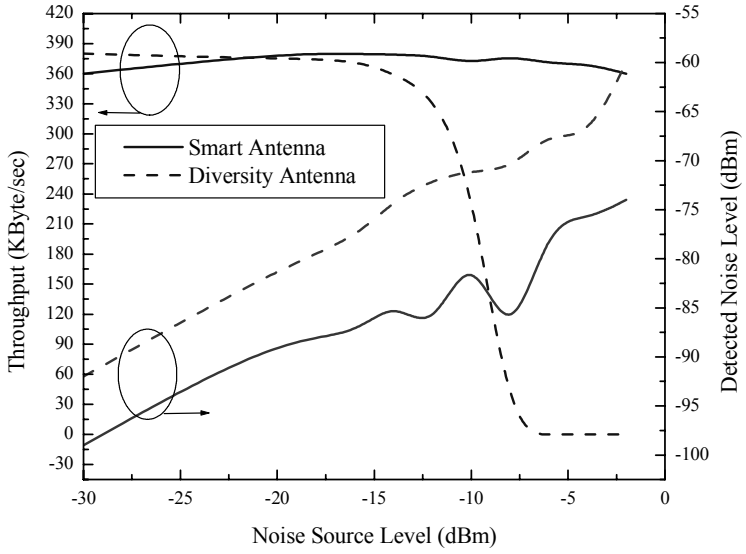

Figure 7.10 Measured throughput and detected noise level in an open outdoor environment. (Carrier: LoS, Interference: LoS, and 38 dB SNR at the AP).

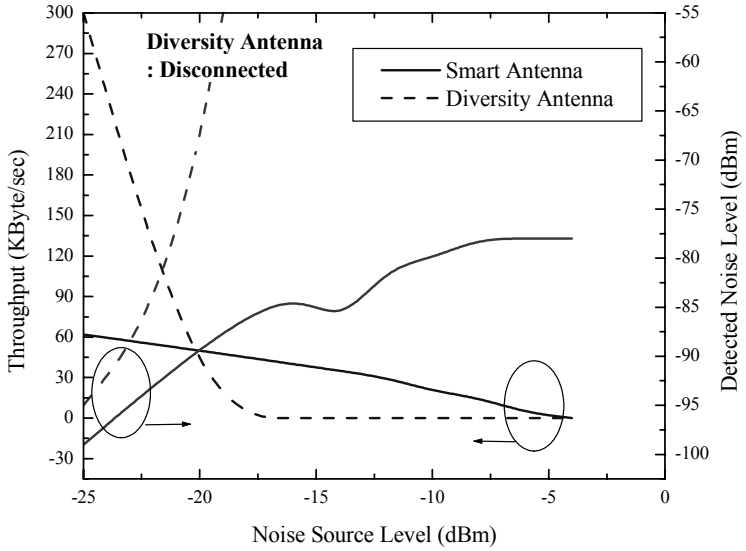

Figure 7.11 Measured throughput and detected noise level in an open outdoor environment. (Carrier: NLoS, Interference: LoS, and 22 dB SNR at the AP).

7.4 CONCLUSIONS

In this chapter, two-element beamforming networks for an 802.11b WLAN client-based smart antenna system based on BST phase shifters were demonstrated. Hardware descriptions of the BFN were discussed along with the design of a very compact integrated BFN. Measured beam patterns and the corresponding throughput improvements were verified with comparison of a diversity antenna system. In the sparse scattering environment, this system could improve significantly in the presence of LoS of both carrier and interference signals, compared to the diversity antenna system built into the commercial wireless network cards. Furthermore, this system enabled the station to keep connecting to the network when the conventional diversity antenna system lost the connection because of the very weak carrier power. Therefore, this smart antenna system

showed very promising results for BST phase shifters.

In future investigation, expected performance of the integrated BFN will be obtained by solving the unknown effects for 802.11b WLAN application. Furthermore, to reduce the overall size of the BFN, a BFN integrated with charge pump circuits to generate voltage larger than the supply voltage will be developed.

CHAPTER VIII

CONCLUSIONS & FUTURE WORK

The aim of this dissertation is the development of compact analog phase shifters based on BST coated sapphire substrates for WLAN applications. Comprehensive material characterizations including linear responses, temperature characteristics, and nonlinear responses were investigated before attempting to implement phase shifters. Several design topologies for BST phase shifters were proposed and successfully fabricated, resulting in the smallest size and best performance obtained to date for *S*-band BST phase shifters. The original contributions of this dissertation include: the first development of CPW-based couplers on high-quality BST thin films; the first development of monolithic BST reflection-type and all-pass network phase shifters; the first demonstration of beamforming networks for WLAN systems using client-based smart antennas with BST phase shifters.

This dissertation began with the metallization process performed by the author at the Georgia Institute of Technology on BST coated sapphire substrates prepared by MCT using its CCVD process. Two different types of photoresists and a standard lift-off process were used to complete top electrodes, depending on the minimum feature size of the pattern. Air bridges were also successfully fabricated to interconnect signal lines or ground planes.

Coplanar waveguides and interdigital capacitors have been used to determine the electrical parameters of the BST thin films at *S*-band. BST permittivity and dielectric loss

associated with capacitance and Q-factor of interdigital capacitors have been extracted with the help of conformal mapping based model and/or commercial EM simulator. Inductors on the BST thin films were also fabricated, resulting in a relatively high Q-factor of ~20 at 2.4 GHz with a small occupied area.

Once the material characteristics were verified at *S*-band, phase shifters were then designed. The initial version of BST phase shifter was a reflection-type structure, which consists of a 3-dB coupler and two identical reflective terminations controlled by an applied bias voltage on BST interdigital capacitors. The phase shifters employing either the CPW branch-line coupler or the CPW Lange coupler were demonstrated along with investigation of two different types of reflective terminations. Although the operating frequency was not optimized at 2.4 GHz, it has promise for providing a large phase-shift range while using a small occupied area of 4 mm × 4 mm.

The next version of BST phase shifter was an all-pass network structure, which used compact lumped-element approach. Two different topologies were considered and analyzed to incorporate with the optimum phase-shift range and loss mechanism. The measured result of the simple all-pass network phase shifter was found to be the best loss FOM and the smallest size obtained to date in the 2.4 GHz band. Additionally, with incorporation of smaller spaced capacitors, it would offer the benefit of reducing bias voltage down to 40 V at the expense of nonlinearity. Temperature responses of the phase shifter to correlate with the best BST composition with respect to variation over temperature were discussed as well. In addition, the phase shifter using π-section lumped-element quarter-wave-length transmission lines was implemented. This phase shifter was capable of providing a phase-shift range of 180° while retaining its compact size.

Once high-performance phase shifters were effectively functioning in the 2.4 GHz band, beamforming networks for WLAN systems using client-based smart antennas then were developed to increase throughput and network capacity by rejecting interference. Hardware descriptions of beamforming networks were described and throughput improvement of WLAN systems was successfully demonstrated.

Several future undertakings related to this research are as follows. One of the most obvious extensions of this research is to further reduce bias voltage. It would be appropriate approach either to employ a parallel plate capacitor at the expense of complexity of fabrication or to shrink the spacing between adjacent fingers in an interdigital capacitor. Furthermore, to overcome the large nonlinearity caused by a decreased bias voltage, the BST phase shifter with the reduced IMD capacitor described in Chapter 4 would be one of the best candidates for future research.

Another topic to be considered with respect to high bias voltage would be a phase shifter integrated with charge pump circuits to generate a voltage larger than the supply voltage. While keeping the established process and design of the phase shifter, additional charge pump circuits could further reduce bias voltage without degradation of linearity. Compact integrated beamforming networks that use phase shifters with integrated charge pump circuits will be another interesting topic for WLAN applications.

Appendix

BST PHASE-SHIFTER FABRICATION

This appendix contains the detailed process sequences used in fabrication of the BST phase shifter.

1. BST sample clean

- Clean a BST sample with trichloroethylene (TCE), acetone, and methanol.
- Rinse with de-ionized (DI) water.
- Dry with N_2 gun.
- Attach the BST sample to a large glass substrate.

2. Top electrode metallization

2.1. NR3000P

- Spin coat a layer of 3.5 μm-thick NR3000P at 2800 rpm for 30 seconds.
- Soft bake the sample in an oven at 95°C for 10 minutes, and cool down naturally.
- Expose UV light for 10 seconds (9 mW) on an OAI mask aligner (wavelength = 365 nm).
- Post bake the sample in an oven at 100°C for 10 minutes, and cool down naturally.
- Develop in RD6 developer for 10 seconds.
- Rinse with DI water and dry with N_2 gun.
- Check the pattern under microscope.

- Load the sample into CVC Electron Beam Evaporator (E-beam evaporator).
- Evaporate Cr/Cu/Au or Ti/Cu/Au after pumping down to 1.3×10^{-6} Torr.
- Cr or Ti (thickness of 300 Å, evaporation rate of 3 Å/sec).
- Cu (thickness of 2 μm, evaporation rate of 5 Å/sec).
- Au (thickness of 0.5 μm, evaporation rate of 5 Å/sec).
- Put the sample in acetone for more than an hour.
- Use ultrasonic to help the lift off, if necessary.
- Rinse with DI water and dry with N_2 gun.
- Check the pattern under microscope.

2.2. SU-8 photoresist

- Spin coat a layer of 17 nm of Omnicoat at 3000 rpm for 30 seconds.
- Soft bake the sample on a hotplate at 200°C for 1 minute, and cool down naturally.
- Spin coat a layer of 4 μm-thick SU-8 at 1500 rpm for 30 seconds
- Soft bake the sample on a hotplate at 65°C for 1 minute and 95°C for 3 minutes, and cool down naturally.
- Expose UV light for 10 seconds (9 mW) on an OAI mask aligner (wavelength = 365 nm).
- Post bake the sample on a hotplate at 65°C for 1 minute and 95°C for 1 minute, and cool down naturally.
- Develop in MicroChem's SU-8 developer (PGMEA) or Thinner P for 20 seconds.

- Rinse with isopropanol and dry with N_2 gun.
- Remove the Omnicoat with MCC 101 developer and Microposit MF 319.
- Use MCC 101 developer for 1 minute and rinse with DI water for 2 minutes.
- Use Microposit MF 319 for 30 seconds and rinse with DI water for 2 minutes.
- Check the pattern under microscope.
- Load the sample into CVC Electron Beam Evaporator (E-beam evaporator).
- Evaporate Cr/Cu/Au or Ti/Cu/Au after pumping down to 1.3×10^{-6} Torr.
- Cr or Ti (thickness of 300 Å, evaporation rate of 3 Å/sec).
- Cu (thickness of 2 μm, evaporation rate of 5 Å/sec).
- Au (thickness of 0.5 μm, evaporation rate of 5 Å/sec).
- Put the sample in MicroChem's Remover PG on a hotplate at 80°C for 10 minutes.
- Use ultrasonic to help the lift off, if necessary.
- Rinse with isopropanol and dry with N_2 gun.
- Remove the Omnicoat with MCC 101 developer and Microposit MF 319.
- Use MCC 101 developer for 1 minute and rinse with DI water for 2 minutes.
- Use Microposit MF 319 for 30 seconds and rinse with DI water for 2 minutes.
- Check the pattern under microscope.

3. Air bridge fabrication

- Spin coat a layer of 10 μm-thick AZ9260 at 1800 rpm for 30 seconds.
- Soft bake the sample in an oven at 95°C for 10 minutes, and cool down naturally.
- Expose UV light for 2 minutes (120 mW) on a Karl Suss MA6 mask aligner

(CH2: wavelength = 405 nm).

- Post bake the sample in an oven at 100°C for 5 minutes, and cool down naturally.
- Develop in AZ400K:DI (1:5 by volume) solution for 2 minutes.
- Rinse with DI water and dry with N_2 gun.
- Check the pattern under microscope.
- Load the samples into CVC DC sputterer.
- Deposit a seed layer of 500 Å of Ti/Cu.
- Spin coat a layer of 10 μm thick AZ9260 at 1800 rpm for 30 seconds.
- Soft bake the sample in an oven at 95°C for 10 minutes, and cool down naturally.
- Expose UV light for 2 minutes (120 mW) on a Karl Suss MA6 mask aligner (CH2: wavelength = 405 nm).
- Post bake the sample in an oven at 100°C for 5 minutes, and cool down naturally.
- Develop in AZ400K:DI (1:5 by volume) solution for 2 minutes.
- Rinse with DI water and dry with N_2 gun.
- Check the pattern under microscope.
- Electroplate the sample in a Cu electroplating bath by biasing the sample with 40 mA/Cm^2 (anode to Cu sourse and cathode to the sample).
- Remove top photoresist (AZ9260) with acetone.
- Remove Cu seed layer in a solution of 1:1:10 (H_2SO_4:H_2O_2:DI).
- Remove Ti seed layer in a solution of 1:10 (HF:DI).
- Remove bottom photoresist (AZ9260) with acetone.

- Rinse with DI water and dry with N_2 gun.
- Check the pattern under microscope.
- Perform RF measurements.

References

[1] K. Uchino, *Ferroelectric devices*, Marcel Dekker, Inc., 2000.

[2] T. M. Shaw, Z. Suo, M. Huang, E. Liniger, R. B. Laibowitz, and J. D. Baniecki, "The effect of stress on the dielectric properties of barium strontium titanate thin films," *Applied Physics Lett*., vol. 75, no. 14, pp. 2129-2131, October 1999.

[3] D. Kim, S. Je, J. S. Kenney, and P. Marry, "Design of ferroelectric phase shifters for minimum performance variation over temperature," accepted in *2004 IEEE MTT-S Int. Microwave Symp.*

[4] O. Auciello, J. F. Scott, and R. Ramesh, "The physics of ferroelectric memories," *Physics Today*, vol. 51, no. 7, pp. 22-27, July 1998.

[5] S. J. Fiedziuszko, I. C. Hunter, T. Itoh, Y. Kobayashi, T. Nishikawa, S. N. Stitzer, and K. Wakino, "Dielectric materials, devices, and circuits," *IEEE Trans. Microwave Theory & Tech*., vol. 50, no. 3, pp. 706-720, March 2002.

[6] F. R. Morgenthaler, "Velocity modulation of electromagnetic waves," *IEEE Trans. Microwave Theory & Tech.*, vol. MTT-6, pp. 167-172, April 1958.

[7] P. D. Coleman and R. C. Becker, "Present state of the millimeter wave generation and technique art-1958," *IEEE Trans. Microwave Theory & Tech.*, vol. MTT-7, pp. 42-61. January 1959.

[8] M. DiDomenico, Jr. and R. H. Pantell, "An X-band ferroelectric phase shifter," *IEEE Trans. Microwave Theory & Tech.*, vol. MTT-10, pp. 179-185, May 1962.

[9] M. Cohn and A. F. Eikenberg, "Ferroelectric phase shifters for VHF and UHF," *IEEE Trans. Microwave Theory & Tech.*, vol. MTT-10, pp. 536-548, November 1962.

[10] M. Cohn and A. F. Eikenberg, "A high-power ferroelectric limiter," *IEEE Trans. Microwave Theory & Tech.*, vol. MTT-13, pp. 47-54, January 1965.

[11] J. W. Amoss, M.R. Donaldson, L. J. Lavedan, A. L. Stanford, and J. E. Pippin, "A ferroelectric microwave switch," *IEEE Trans. Microwave Theory & Tech.*, vol. MTT-13, pp. 789-793, November 1965.

[12] J. B. Horton and M. R. Donaldson, "A one-GHz ferroelectric limiter," *IEEE Trans. Microwave Theory & Tech.*, vol. MTT-15, pp. 517-623, September 1967.

[13] R. Das, "Ferroelectric phase shifters," *1967 IEEE MTT-S Int. Microwave Symp. Dig.*, vol. 67, pp. 185-187, 1967.

[14] J. A. Beall, R. H. Ono, D. Galt, and J. C. Price, "Tunable high temperature super conductor microstrip resonators," *1993 IEEE MTT-S Int. Microwave Symp. Dig.*, vol. 3, pp. 1421-1423, 1993.

[15] C. M. Jackson, T. Pham, Z. Zhang, A. Lee, C. Pettiete-Hall, "Model for a novel CPW phase shifter," *1995 IEEE MTT-S Int. Microwave Symp. Dig.*, vol. 3, pp. 1439-1442, 1995.

[16] F. De Flaviis, N. G. Alexopoulos, and O. M. Stafsudd, "Planar microwave integrated phase-shifter design with high purity ferroelectric material," *IEEE Trans. Microwave Theory & Tech.*, vol. 45, no. 6, pp. 963-969, June 1997.

[17] G. Subramanyam, F. V. Keuls, F. A. Miranda, "A K-band tunable microstrip bandpass filter using a thin-film conductor/ferroelectric/dielectric multilayer configuration," *IEEE Microwave Guided Wave Lett.*, vol. 8, no. 2, pp.78-80, February 1998.

[18] A. Kozyrev, A. Ivanov, V. Keis, M. Khazov, V. Osadchy, T. Samoilova, O. Soldatenkov, A. Pavlov, G. Koepf, C. Mueller, D. Galt, and T. Rivkin, "Ferroelectric films: nonlinear properties and applications in microwave devices," *1998 IEEE MTT-S Int. Microwave Symp. Dig.*, vol. 2, pp. 985-988, June 1998.

[19] A. Kozyrev, V. Osadchy, A. Pavlov, and L. Sengupta, "Application of ferroelectrics in phase shifter design," *2000 IEEE MTT-S Int. Microwave Symp. Dig.*, vol. 3, pp. 1355-1358, June 2000.

[20] E.G. Erker, A. S. Nagra, Y. Liu, P. Periaswamy, T. R. Taylor, J. Speck, and R. A. York, "Monolithic Ka-band phase shifter using voltage tunable BaSrTiO3 parallel plate capacitors," *IEEE Microwave Guided Wave Lett.*, vol. 10, no. 1, pp. 10-12, January 2000.

[21] Y. Liu, A. S. Nagra, E. G. Erker, P. Periaswamy, T. R. Taylor, J. Speck, and R. A. York, "$BaSrTiO_3$ interdigitated capacitors for distributed phase shifter applications," *IEEE Microwave Guided Wave Lett.*, vol. 10, no. 11, pp. 448-450, November 2000.

[22] B. Acikel, Y. Liu, A. S. Nagra, T. R. Taylor, P. J. Hansen, J. S. Speck and R. A. York, "Phase shifters using (Ba,Sr)TiO_3 thin films on sapphire and glass substrates," *2001 IEEE MTT-S Int. Microwave Symp. Dig.*, vol. 3, pp. 1191-1194, June 2001.

[23] V. Sherman, K. Astafiev, N. Setter, A. Tagantsev, O. Vendik, I. Vendik, S. Hoffmann, U. Böttger, and R. Waser, "Digital reflection-type phase shifter based on a ferroelectric planar capacitor," " *IEEE Microwave and Wireless Components Lett.*, vol. 11, no. 10, pp. 407-409, October 2001.

[24] A. Tombak, J. P. Maria, F. Ayguavives, Z. Jin, G. T. Stauf, A. I. Kingon, and A. Mortazawi, "Tunable barium strontium titanate thin film capacitors for RF and microwave applications," *IEEE Microwave and Wireless Components Lett.*, vol. 12, no. 1, pp. 3-5, January 2002.

[25] A. S. Nagra and R. A. York, "Distributed analog phase shifters with low insertion loss," *IEEE Trans. Microwave Theory & Tech.*, vol. 47, no. 9, pp. 1705-1711, September 1999.

[26] B. Acikel, T. R. Taylor, P. J. Hansen, J. S. Speck, and R. A. York, "A new high performance phase shifter using $Ba_xSr_{1-x}TiO_3$ thin films," *IEEE Microwave and Wireless Components Lett.*, vol. 12, no. 7, pp. 237-239, July 2002.

[27] R. N. Hardin, E. J. Downey, and J. Munushian, "Electronically-variable phase shifters utilizing variable capacitance diodes," *Proc. IRE*, vol. 48, pp. 944-945, May 1960.

[28] F. Ellinger, R. Vogt, and W. Bächtold, "Compact reflective-type phase-shifter MMIC for C-band using a lumped element coupler," *IEEE Trans. Microwave Theory & Tech.*, vol. 49, no. 5, pp. 913-917, May 2001.

[29] K. Miyaguchi, M. Hieda, K. Nakahara, H. Kurusu, M. Nii, M Kasahara, T. Takagi, and S. Urasaki, "An ultra-broad-band reflection-type phase-shifter MMIC with series and parallel LC circuits," *IEEE Trans. Microwave Theory & Tech.*, vol. 49, no. 12, pp. 2446-2452, December 2001.

[30] D. Kim, Y. Choi, M. G. Allen, J. S. Kenney, and D. Kiesling, "A wide bandwidth monolithic BST reflection-type phase shifter using a coplanar waveguide Lange coupler," *2002 IEEE MTT-S Int. Microwave Symp. Dig.,* vol. 3, pp. 1471-1474, June 2002.

[31] D. Kim, Y. Choi, M. G. Allen, J. S. Kenney, and D. Kiesling, "A wide-band reflection-type phase shifter at S-band using BST coated substrate," *IEEE Trans. Microwave Theory & Tech.*, vol. 50, no. 12, pp. 2903-2909, December 2002.

[32] J. L. Serraiocco, P. J. Hansen, T. R. Taylor, J. S. Speck, and R. A. York, "Compact ferroelectric reflection phase shifters at X-band," *2003 IEEE MTT-S Int. Microwave Symp. Dig.,* vol. 3, pp. 1993-1996, June 2003.

[33] B. T. Henoch and P. Tamm, "A 360° reflection-type diode phase modulator," *IEEE Trans. Microwave Theory & Tech.*, vol. 19, pp. 103-1056, January 1971.

[34] D. Kim, Y. Choi, M. Ahn, M. G. Allen, and J. S. Kenney, "Monolithic 180° and 360° analog phase shifters based on barium-strontium-titanate coated substrate," *IEICE Trans. Electronics,* vol. E86-C, no. 8, pp. 1607-1612, August 2003.

[35] D. Kim, Y. Choi, M. Ahn, M. G. Allen, J. S. Kenney, and P. Marry, "2.4 GHz continuously variable ferroelectric phase shifters using all-pass networks," *IEEE Microwave and Wireless Components Lett.* vol. 13, no. 10, pp. 434-437, October 2003.

[36] Y. Liu, A. Borgioli, A. S. Nagra, and R. A. York, "K-band 3-bit low-loss distributed MEMS phase shifter," *IEEE Microwave Guided Wave Lett.*, vol. 10, no. 10, pp. 415-417, October 2000.

[37] G. M. Rebeiz, G. –L. Tan, J. S. Hayden, "RF MEMS phase shifters: Design and applications," *IEEE Microwave magazine*, vol. 3, pp. 72-81, June 2002.

[38] A. Borgioli, Y. Liu, A. S. Nagra, and R. A. York, "Low-loss distributed MEMS phase shifter," *IEEE Microwave Guided Wave Lett.*, vol. 10, no. 1, pp. 7-9, January 2000.

[39] B. Lakshminarayanan and T. Weller, "Distributed MEMS phase shifters on silicon using tapered impedance unit cells," *2002 IEEE MTT-S Int. Microwave Symp. Dig.*, vol. 2, pp. 1237-1240, June 2002.

[40] B. Pillans, S. Eshelman, A. Malczewski, J. Ehmke, and C. Goldsmith, "Ka-band RF MEMS phase shifter," *IEEE Microwave Guided Wave Lett.*, vol. 9, no. 12, pp. 520-522, December 1999.

[41] N. S. Barker and G. M. Rebeiz, "Optimization of distributed MEMS transmission-line phase shifters-U-band and W-band designs," *IEEE Trans. Microwave Theory & Tech.*, vol. 48, no. 11, pp. 1957-1966, November 2000.

[42] A. Malczewski, S. Eshelman, B. Pillans, J. Ehmke, and C. L. Goldsmith, "X-band RF MEMS phase shifters for phased array applications," *IEEE Microwave Guided Wave Lett.*, vol. 9, no. 12, pp. 517-519, December 1999.

[43] M. Kim, J. B. Hacker, R. E. Mihailovich, and J. F. DeNatale, "A DC-to-40 GHz four-bit RF MEMS true-time delay network," *IEEE Microwave and Wireless Components Lett.*, vol. 11, no. 2, pp. 56-58, February 2001.

[44] H. –T. Kim, J. –H. Park, Y. –K. Park, and Y. Kwon, "V-band low-loss and low-voltage distributed MEMS digital phase shifter using metal-air-metal capacitors," *2002 IEEE MTT-S Int. Microwave Symp. Dig.,* vol. 1, pp. 341-344, June 2002.

[45] J. S. Hayden and G. M. Rebeiz, "A low-loss Ka-band distributed MEMS 2-bit phase shifter using metal-air-metal capacitors," *2002 IEEE MTT-S Int. Microwave Symp. Dig.,* vol. 1, pp. 337-340, June 2002.

[46] C. F. Campbell and S. A. Brown, "A compact 5-bit phase-shifter MMIC for K-band satellite communication systems," *IEEE Trans. Microwave Theory & Tech*., vol. 48, no. 12, pp. 2652-2656, December 2000.

[47] D. M. Krafcsik, S. A. Imhoff, D. E. Dawson, and A. L. Conti, "A dual-varactor analog phase shifter operating at 6 to 18 GHz," *IEEE Trans. Microwave Theory & Tech.*, vol. 36, no. 12, pp. 1938-1941, December 1988.

[48] H. Hayashi, T. Nakagawa, K. Araki, "A miniaturized MMIC analog phase shifter using two quarter-wave-length transmission lines," *IEEE Trans. Microwave Theory & Tech.*, vol. 50, no. 1, pp. 150-154, January 2002.

[49] D. Kim, S. Je, J. S. Kenney, and P. Marry, "A compact ferroelectric phase shifter using lumped-element quarter-wave transmission lines," *2003 Radio and Wireless Conf. Dig.*, pp. 309-312, August 2003.

[50] C. Chen, W. E. Courtney, L. J. Mahoney, M. J. Manfra, A. Chu, and H. A. Atwater, "A low-loss Ku-band monolithic analog phase shifter," *IEEE Trans. Microwave Theory & Tech.*, vol. MTT-35, no. 3, pp. 315-320, March 1987.

[51] F. Ellinger, R. Vogt, and W. Bächtold, "Ultracompact reflective-type phase shifter MMIC at C-band with 360° phase-control range for smart antenna combining," *IEEE Trans. Solid-State Circuits*, vol. 37, no. 4, pp. 481-486, April 2002.

[52] Y. –S. Dai and T. –S. Chen, "A novel ultra-wideband 90 degrees GaAs MMIC phase shifter with either analogue or digital control," *2000 Asian-Pacific Microwave Conf. Dig.,* pp. 1081-1084, December 2000.

[53] S. Ya, C. Jiyi, C. Tangsheng, C. Xiaojian, and L. Jinting, "A compact L-band four-bit MMIC phase shifter," *1998 International Conf. On Microwave and Millimeter Wave Tech. Proc.,* pp. 242-244, August 1998.

[54] F. Ellinger, H. Jackel, and W. Bachtold, "Varactor-loaded transmission-line phase shifter at C-band lumped elements," *IEEE Trans. Microwave Theory & Tech*., vol. 51, no. 4, pp. 1135-1140, April 2003.

[55] S. Nam, A. W. Payne, and I. D. Robertson, "RF and microwave phase shifter using complementary bias techniques," *Electron. Lett*., vol. 37, no. 18, pp. 1124-1125, August 2001.

[56] MicroCoating Technologies, Inc. Chamblee, GA, http://www.microcoating.com.

[57] Futurrex, Inc. Franklin, NJ, http://www.futurrex.com.

[58] MicroChem Copr. Newton, MA, http://www.microchem.com.

[59] C. P. Wen, "Coplanar waveguide: a surface strip transmission line suitable for nonreciprocal gyromagnetic device applications," *IEEE Trans. Microwave Theory & Tech*., vol. 17, no. 12, pp. 1087-1090, December 1969.

[60] Microwave Office, Applied Wave Research, Inc., El Segundo, CA.

[61] K. Ikuta, Y. Umeda, and Y. Ishii, "Measurement of high-frequency dielectric characteristics in the mm-wave band for dielectric thin films on semiconductor substrates," *Jpn. J. Appl. Phys.*, vol 34, pp. L1211-L1213, September 1995.

[62] D. Kim, S. Je, J. S. Kenney, and P. Marry, "Tunable $Ba_xSr_{1-x}TiO_3$ interdigital capacitors for microwave applications," *2003 Asian-Pacific Microwave Conf. Dig.,* vol. 3, November 2003.

[63] Y. Yoon, D. Kim, M. G. Allen, A. T. Hunt, and J. S. Kenney, "A reduced intermodulation tunable ferroelectric capacitor-architecture and demonstration", *IEEE Trans. Microwave Theory & Tech.*, vol. 51, no. 12, pp. 2568-2576, December 2003.

[64] S. S. Gevorgian, T. Martinsson, P. L. J. Linner, and E. L. Kollberg, "CAD models for multilayered substrate interdigital capacitors," *IEEE Trans. Microwave Theory & Tech*., vol. 44, no. 6, pp. 896-904, June 1996.

[65] S. Je, D. Kim, J. S. Kenney, and T. Polley, "Effect of annealing and sintering on the structural and electrical properties of $Ba_{0.6}Sr_{0.4}TiO_3$ thin films grown on sapphire by combustion chemical vapor deposition (CCVD)," *2003 Asian-Pacific Microwave Conf. Dig.,* vol. 3, November 2003.

[66] C. B. Parker, J. –P. Maria, and A. I. Kingon, "Temperature and thickness dependent permittivity of (Ba,Sr)TiO_3 thin films," *Applied Physics Lett*., vol.81, no. 2, pp. 340-342, July 2002.

[67] S. S. Gevorgian and E. L. Kollberg, "Do we really need ferroelectrics in paraelectric phase only in electrically controlled microwave devices?" *IEEE Trans. Microwave Theory & Tech*., vol. 49, no. 11, pp. 2117-2124, November 2001.

[68] N. Pothecary, *Feedforward linear power amplifiers*, Norwood, MA: Artech House, 1999.

[69] J. Lange, "Interdigitated stripline quadrature hybrid," *IEEE Trans. Microwave Theory & Tech.*, vol. MTT-17, pp. 1150-1151, December 1969.

[70] D. M. Pozar, *Microwave engineering*, John Wiley & Sons, Inc., 1998.

[71] N. E. Hodges and M. H. Yam, "A precise analog phase shifter for SHF SATCOM phased arrays," *GaAs IC Symp. Dig*., pp. 29-32, 1992.

[72] J. C. Liberti, Jr. and T. S. Rappaport, *Smart antennas for wireless communications: IS-95 and third generation CDMA applications*, NJ: Prentis Hall, Inc. 1999.

[73] E. Desautel, D. Kim, J. S. Kenney, and D. Kiesling, "Interference mitigation in WLAN networks using client-based smart antennas," *2002 Radio and Wireless Conf. Dig.*, pp. 63-66, August 2002.

[74] M. Ahn, G. Quillard, D. Kim, and J. S. Kenney, "Design and implementation of a ferroelectric smart antenna system for 802.11b WLANs," *2003 Radio and Wireless Conf. Dig.,* pp. 309-312, August 2003.

[75] IEEE Std.802.11b Supplement to Part Ⅱ: Wireless LAN medium access control (MAC) and physical layer (PHY) specifications: higher-speed physical layer extension in the 2.4 GHz Band, IEEE Std. 802.11b-1999, 1999.

Vita

Dongsu Kim was born in Taegu, Korea in 1972. He received his B.S. degree and M.S. degree in electronics engineering from the Kyungpook National University, Taegu, Korea, in 1997 and 1999, respectively. He also received the M.S. degree in electrical and computer engineering from the Georgia Institute of Technology, Atlanta, GA, in 2001. Since 2000, he has been working toward his doctoral degree in electrical and computer engineering at the Georgia Institute of Technology under supervision of Dr. J. Stevenson Kenney.

While at the Georgia Institute of Technology, he worked as a research assistant in the Communication Systems Technology (CST) Laboratory from March 2000 to April 2004. His research focuses on the design and fabrication of RF passive component, ferroelectric devices, and beamforming networks for smart antenna systems.